Templated Aqueous Syntheses of Inorganics within Carboxyl-Containing Block Copolymer Domains

by

Yot Boontongkong

Bachelor of Science, Materials Science and Engineering
Northwestern University, Evanston, Illinois, 1995
Master of Science, Materials Science and Engineering
Massachusetts Institute of Technology, Cambridge, Massachusetts, 1997

Submitted to the Department of Materials Science and Engineering
in Partial Fulfillment of the Requirements for the Degree of

DOCTOR OF PHILOSOPHY IN POLYMERS

at the
MASSACHUSETTS INSTITUTE OF TECHNOLOGY
February 2002

Signature of Author .....
Department of Materials Science and Engineering
Program in Polymer Science and Technology
January 11, 2002

Certified by .....
Robert E. Cohen
St. Laurent Professor of Chemical Engineering
Thesis Supervisor

Certified by .....
Michael F. Rubner
TDK Professor of Polymer Materials Science and Engineering
Thesis Reader

Accepted by .....
Harry L. Tuller
Professor of Ceramics and Electronic Materials
Chairman, Departmental Committee on Graduate Students

Templated Aqueous Syntheses of Inorganics within Carboxyl-containing Block Copolymer Domains

by

Yot Boontongkong

Submitted to the Department of Materials Science and Engineering on January 11, 2002,
in partial fulfillment of the requirements for the degree of
Doctor of Philosophy in Polymers

ABSTRACT

Template-directed, aqueous-based syntheses of nanoscale inorganic materials in carboxyl-functionalized block copolymer domains (nanoreactors) were demonstrated. First, the successful application of electroless metal deposition within the sub-surface lamellar domains of an amphiphilic block copolymer is presented. Several electroless metals were selectively deposited inside the interconnected network of the water-permeable block domains containing pre-loaded palladium, which served as the spatially localized deposition catalyst. The technique proved to be a facile means to rapidly deposit large amounts of metals within the hydrophilic block domains, despite limitations on the transport of plating reagents into the bulk templates. The simple process yielded novel nanocomposites consisting of alternating layers of metal with those of the hydrocarbon matrix. The extent of metal deposition within the bulk block copolymer templates was controlled by adjusting the deposition rate and deposition time.

Second, unique self-assembled thin film templates comprising in-plane arrays of nanosized surface cavities were investigated. The micellar thin films, formed by direct casting of kinetically stable styrene(PS)-acrylic acid(PAA) block copolymer reverse micelles from toluene onto solid substrates, consisted of lateral hexagonal arrays of spherical PAA domains in PS matrices. It was shown that hydration and swelling of PAA upon treatment in a monovalent base (NaOH) aqueous solution led to a cavitation process that exposed the PAA cores to the free surface. The use of these cavitated PAA domains as open nanoreactors for the synthesis of corresponding nanocluster arrays following aqueous sequestration of metal ions into carboxyl-containing domains was demonstrated. Metal loading of the PAA domains could alternatively be achieved in the absence of cavitation by omitting the base treatment step, where the loaded PAA domains remained embedded within the original PS matrix. Additional stability was imparted to the nanoclusters synthesized within these closed nanoreactors relative to their cavitated counterparts. The option to employ either the open or the closed micellar templates represents a useful versatility of this system.

Thesis Supervisor: Robert E. Cohen
Title: St. Laurent Professor of Chemical Engineering

Acknowledgments

First, I thank my advisor, Professor Robert Cohen, for his generous academic and mental support over the past 6 years. During this time there have been several uneasy periods when my work was not progressing well. Fortunately, I was able to rely on Prof. Cohen's guidance and encouragement as a motivation to continue. I especially appreciate the opportunities that he allowed for me to step back and sort out my thoughts when I needed them. His optimism and reassuring support have enabled me to finally put these last few words together to complete my thesis work.

I thank Professor Michael Rubner for offering his valuable inputs to my work, especially for introducing to me the electroless plating technique. It helped jump-start my project during a slow period, and led to the work that constitutes Chapter 2 of this document. I'd also like to thank Professor Samuel Allen for his kind and helpful comments on my work and writing.

I have been fortunate to share the lab with a pleasant group of people. I thank the Cohen group members, both former and current, who provided help with my work as well as a cordial lab atmosphere. In particular, I'd like to acknowledge Tom Wang and Yonathan Thio for making our lab a simpler, more productive workplace. Tom seemed to be able to assist and provide answers for all my 'how-to' questions – from experimental to computer-related. Yonathan contributed to many aspects of my work, and regularly offered to help out, even when I was grumpy. I also thank him for proofreading practically this entire thesis!

I thank Jason Gratt and Alice Man for their help when I was getting started on this project; Jeff Abes and Leslie Loo for acquiring TEM, NMR, and AFM data while I was training to become a self-user; and Russ Clay, Ravi Kane, and Younghwan Kwon for their helpful discussions. I'd like to thank Liz Webb, Arline Benford, and Danielle Delgado who provided administrative support and welcoming smiles. Thanks also to Libby Shaw for her kind assistance with the AFM.

I thank Ya and Tengo, my local compatriots, for their friendship and for the tennis we played. Thanks to my friends Rob and Brad for spending time with me when I wanted to get away from work. I am grateful to my mentor, Serra, who patiently encouraged me to find happiness in myself. Finally, I thank my parents, sister, and grandmother for all their love and support, especially on my decision to study abroad.

I never really imagined life after a Ph.D., partly because up until this moment I've always been a student, and partly because the prospect of the degree often appeared distant. Now that it's almost a reality, I hope the knowledge and memories accumulated during my time at MIT will help translate the path ahead into a fulfilling journey.

Table of Contents

4. Thesis Summary

Appendices

List of Figures

List of Schemes

List of Tables

List of Acronyms and Symbols

2D: Two-dimensional
Ac: [CH_3COO] = acetate
AFM: Atomic force microscopy
-b-: -block-
CMSE: Center for Materials Science and Engineering, MIT
DMAB: Dimethylamine borane
GPC: Gel permeation chromatography
LARS: Load-and-reduction sequence (**Scheme 1.1B**)
Me: [CH_3] = methyl
MTD: Methyltetracyclododecene
NMR: Nuclear magnetic resonance
NORCOOH: 2-norbornene-5,6-dicarboxylic acid
NORCOOTMS: 2-norbornene-5,6-dicarboxylic acid-bis trimethylsilyl ester
PAA: poly(acrylic acid)
PS: polystyrene
ROMP: Ring-opening metathesis polymerization
SEM: Scanning electron microscopy
STEM: Scanning transmission electron microscopy
TEM: Transmission electron microscopy
THF: Tetrahydrofuran
λ: Light wavelength

Chapter 1
Introduction

1.1 General background

1.1.1 Block copolymers

A block copolymer molecule is made up of two or more chemically distinct sequences (blocks) of repeat units (monomers) covalently bonded to one another. For example, a linear macromolecule comprising two monomer sequences is referred to as a diblock copolymer. As a common behavior, thermodynamic driving forces favor segregation or demixing of the dissimilar blocks, with the exception of miscible constituent block species that have adequately small enthalpic segmental interactions (represented by the Flory-Huggins parameter, χ).[1] Since true macroscopic phase separation is prevented by the block linkage, block copolymers exhibit local, molecular-scale ordering in the melt state. This self-assembly process is commonly called 'microphase separation' despite the fact that the characteristic length scales of the resulting periodic structures are generally within the nanometer regime.

Theoretical and experimental investigations have established several equilibrium diblock copolymer bulk morphologies;[2-4] the most commonly observed are body-centered cubic spheres, hexagonal-packed cylinders, and lamellae (illustrated in **Figure 1.1**.) Alternating lamellar domains of segregated blocks form at approximately equal volume fractions of the constituent blocks. Transitions towards cylindrical and spherical domains of the minor block embedded in the continuous matrix of the major block occur upon a gradual reduction in the volume fraction of the minor block. Several intermediate bicontinuous morphologies also exist between the cylindrical and lamellar structures, such as double-diamond[5] and gyroid[6,7] (not shown). Aside from the relative block volume fractions, the ordering of block copolymers is also influenced by

the absolute molecular weight of the macromolecules, temperature, and the degree of block compatibility (i.e., block chemical compositions).

The interactions between small-molecule solvents and block copolymers represent another variable for manipulating block copolymer self-assembly. For example, it has been shown that casting a single block copolymer from solutions of different solvents leads to a variety of metastable morphologies.[8] Though not thermodynamically favorable, such kinetically stable morphologies are observed upon (rapid) solvent evaporation due to limited polymer chain mobility below the glass transition temperature. Of particular relevance to this work is the aggregation of block copolymer micelles which occur as a result of differential solvation of the component blocks in selective solvents.[9,10] The use of kinetically locked, solvent-free block copolymer micelles as in situ templates for nanoclusters is the subject of the work presented in Chapter 3 of this document.

1.1.2 Templating inorganics in block copolymer domains

Nanoclusters are aggregates of atoms or molecules with characteristic size scale on the order of nanometers, which is intermediate between those of the bulk and the atom. They have been of interest to scientists and engineers because they exhibit properties that are also intermediate between those of the bulk and the atom, and are strongly dependent on the cluster size.[11] Unique and potentially useful catalytic, magnetic, optical, and semiconducting properties[11-14] arise from the quantum size effects due to incompletely developed electronic band structure from discrete atomic electronic configurations,[11,15,16] as well as from the magnified surface-area-to-volume ratio due to diminutive sizes.[17] For example, the band gaps of semiconducting nanoclusters enlarge with decreasing cluster size due to the quantum size effects, resulting in blue-shifting of the absorption edges.[13,18,19]

The use of polymers as supporting media for nanoclusters combines the unique functional properties of the clusters with the processibility and mechanical properties of polymeric materials, as well as other potentially desirable qualities such as optical transparency and permeability. Polymer matrices also serve to stabilize the individual clusters against interparticle agglomeration: nanoclusters of uniform size are necessary for well-defined collective properties. Examples of incorporating nanocluster into homopolymer matrices are condensation of metal vapor into liquid monomer prior to polymerization,[20,21] simultaneous metal evaporation and plasma polymerization,[22] and infusion of organometallic precursors dissolved in supercritical CO_2 into solid polymers followed by reduction.[23]

Block copolymers have also been used as in situ templates for nanoclusters, providing additional control over the location and spatial distribution of nanoparticles within the polymer matrices.[24-26] Previous works in the Cohen research group[27,28] have taken advantage of the diblock copolymer morphologies, utilizing the segregated block domains as 'nanoreactors'. Such domains naturally provide spatial confinement for chemical species that can be selectively dispersed within one of the block domains but is excluded by the other. These nanoscale compartments are beneficial as small reactors inside of which a variety of interesting chemical reactions can be conducted - in particular, the in situ synthesis of metal-based nanoclusters within the microphase-separated domains.

To template inorganic nanoclusters in block copolymers, metal precursors must first be distributed within the microphase-separated block domains (nanoreactors). Two different approaches have been employed by our research group. One route is to attach the metal species as a pendant group to organometallic monomers to be polymerized into an organometallic block. This method gives

uniform dispersion of the metal precursor within the metal-containing block domains upon microphase separation, and uniform clusters of PbS,[29] ZnS,[18] ZnF_2,[30] Ag,[31,32] and Pd,[33] for example, were synthesized via this scheme. However, the drawback of this metal dispersion route is the fact that lengthy synthetic procedures are usually required to obtain organometallic monomers for each particular metal species.

The other, more general, approach is to selectively 'load' metallic species from external reservoirs into preformed microphase-separated block copolymer domains that contain reactive metal-binding moieties. Yue et al.[34] developed a loading methodology that makes use of carboxylic acid block functionalities as the metal-sequestering groups. Shown in **Scheme 1.1A**, this simple loading technique operates by substituting the carboxylic protons (H^+) with cations of the desired metal species during the sequestration reaction. Via such ion-exchange process, the metal ions are effectively solubilized into the carboxylic domains as the counter-cations for the carboxylate anions. Metal loading can be achieved either with aqueous metal salt solution or with vapor permeation of metal-alkyl compounds (e.g., $ZnEt_2$ and $CdMe_2$), depending on the block copolymer morphology to be loaded. This universal scheme has enabled the incorporation of a variety of transition and rare-earth metal ions into the microdomains of a single starting diblock copolymer.[35,36]

Following the loading step, formation of zero-valent metallic nanoclusters occurs by exposing the loaded block copolymer sample to a reducing agent; e.g., H_2 gas. As shown in **Scheme 1.1A**, the reduction process converts the solubilized metal cations to zero-valent atoms. Localized precipitation of these metallic atoms leads to the formation of nanoclusters within the carboxylic microdomains. Notice that upon completion of the 'loading cycle' via H_2 reduction, the protic

carboxylic acid groups become regenerated. This reactivation gives the loading scheme the versatility of performing multiple loading cycles in order to increase the size and the amount of metal nanoclusters in the microdomains. In a similar fashion, nanoclusters of various metal-based derivatives can be synthesized via the use of other cluster-forming reagents.[30,34,19,37] For example, the introduction of $H_2S_{(g)}$ to the loaded metal ion precursors yields metal sulfide clusters, e.g., semiconducting ZnS and PbS. Synthesizing nanoclusters of mixed[34] or doped[37] chemical species is also possible with this technique.

Selective metal sequestration can be achieved by permeation of vapors of metal-alkyl compounds such as diethylzinc and dimethylcadmium into the polymer matrix.[34] As an example of vapor-phase loading, clusters of PbS were synthesized by Kane et al.[19] Permeation of tetraethyllead vapor into the preformed spherical carboxyl-containing microdomains allowed the coordination of the tetravalent lead with the carboxylate groups. Subsequent heat treatment to reduce lead to its divalent form and exposure to H_2S created the PbS nanoclusters, as well as regenerated the active carboxylic acid groups. Such vapor-phase loading method may be applied to essentially any preformed block copolymer morphologies since vapors of metallic alkyl compounds readily permeate organic polymers. Still, a constraint associated with this loading method is the limited availability of metal-alkyl compounds.

Alternatively, loading nanocluster precursors into carboxyl-containing microdomains can be achieved via uptake of metal ions from salt solutions. This loading method is suitable when the acid domains are interconnected throughout the bulk matrix, enabling metal ions to diffuse into the hydrophilic microdomains from external aqueous reservoirs. Sequestration occurs upon coordination of metal species by carboxylate anions, leading to a uniform dispersion of the metal ions within the carboxylic block domains. Yue et al.[34] and Clay et al.[35] demonstrated the

permeation and sequestration of various aqueous metal salts into the interconnected, water-absorbing carboxylic-functionalized NORCOOH microdomains of MTD-NORCOOH block copolymers (structure in **Scheme 1.3**) using this aqueous loading technique. Subsequent reduction of the metal ions with $H_{2(g)}$ and $NaBH_{4(aq)}$ resulted in a wide variety of metallic nanocluster species (e.g., Ag, Au, Cu, Ni, Pb, Pd, Pt)[38] within the NORCOOH domains as well as reactivated carboxylic acid groups.

A noteworthy modification to the universal loading scheme via aqueous salt solution was introduced by Clay et al.[39] Prior to metal loading, the block copolymer polymer is pre-treated in a $NaOH_{aq}$ solution to convert the protonated carboxylic acid groups in NORCOOH domains to sodium carboxylate. **Scheme 1.1B** illustrates the 2-step ion-exchange loading method of this so-called 'load-and-reduction sequence' (LARS). With the LARS technique, they observed that both the rate and the equilibrium amount of metal ion uptake into the NORCOOH domain significantly increased compared to without NaOH treatment (**Scheme 1.1A**). The observed enhancement in metal loading is attributed to fact that Na^+ counter-cations more readily dissociate from COO^- (carboxylate) anions in aqueous solution than do the acid protons (H^+). As a result, the uptake of transition metal into the microdomains is facilitated since the heavier metal ions can readily replace the Na^+ ions as the counter-cations for the carboxylate anions. This increased loading capability was demonstrated by a significant 26wt% cumulative loading of silver in the Ag-diblock copolymer nanocomposite after four LARS cycles.

Inorganic nanoclusters formed with this aqueous-based load-and-reduction methodology are typically small (several nanometers in size) and spherical, are relatively uniform in size, and are homogeneously distributed within the confine of the originally metal-loaded, carboxyl-containing block copolymer microdomains. We note that though vapor-phase loading was occasionally

employed, the majority of this thesis work relied on the aqueous schemes similar to the aforementioned techniques - with certain modifications outlined in Chapter 2 - as the main methods for the in situ synthesis of nanoscale inorganics in the microdomains of different block copolymer templates.

1.2 Preliminary results

Presented in this section are results from the early stages of this thesis project aimed at reproducing previous works by the Cohen group, which served as the basis for the subsequent original contribution presented in the following chapters of this document. These include the synthesis and characterization of $MTD_{400}NORCOOH_{50}$ block copolymer, as well as carrying out the load-and-reduction (LARS) procedures for in situ nanocluster synthesis using this ROMP diblock copolymer as the template. The same polymer was employed for the electroless metal deposition experiments described in Chapter 2. Chapter 3 discusses the application of the aqueous-based nanocluster synthesis techniques outlined in the previous section towards another set of block copolymer templates, namely the deposited micelles of a commercial styrene-acrylic acid block copolymer.

1.2.1 Synthesis of poly(MTD_{400}-block-$NORCOOH_{50}$)

Introduction

Ring-opening metathesis polymerization (ROMP) involves the metathesis (ligand switching) reaction of a metal-alkylidene with a cyclic olefin via the formation of a metallacycloalkane intermediate[40,41] as illustrated in **Scheme 1.2**. Ring-opening of the cyclic olefin monomer upon cleavage of its double bond constitutes the chain-growth propagation of the polymerization. Developments of ROMP initiators that selectively polymerize strained cyclic alkene monomers via such metathesis mechanism have been achieved primarily by the Schrock[42,43] and the

Grubbs[44,45] research groups. These specialized organometallic initiators have enabled the living polymerization of well-defined block copolymers with narrow molecular weight dispersity. The ROMP initiators' tolerance for a variety of monomer functionalities[46] allows for the synthesis of block copolymers that were not possible to make via anionic polymerization; for example, the polymerization of organometallic monomers.[47,48]

The ROMP technique has afforded the Cohen group the ability to synthesize a variety of functional block copolymers with the control over the molecular architecture (hence, the morphology) to meet experimental demands. Functionalized derivatives of norbornene make up the family of strained cyclic monomers most extensively employed by the research group.[18,29-33,49,50] A potential disadvantage of ROMP polymers is the presence of double bonds along the polymer backbone that could limit certain double bond-active chemistry and render the polymer susceptible to oxidative degradation. This shortcoming, however, is preventable by saturation of the double bonds via hydrogenation.[51]

Materials and equipment

NORCOOH capping and subsequent ROMP polymerization were performed in a nitrogen-atmosphere drybox (MBraun LabMaster 130) as the ROMP initiator used is moisture- and oxygen-sensitive. MTD (methyltetracyclododecene) monomer (**Figure 1.2**) (donated by BF Goodrich) and chlorotrimethylsilane had been degassed by a previous user and stored in the drybox prior to our use. All solvents and reagents used were anhydrous and/or deoxygenated (except for the NORCOOH starting monomer). The Mo-based Schrock initiator (2,6-diisopropylphenylimido neophylidenemolybdenum(VI) bis(t-butoxide) (**Figure 1.2**) was purchased from Strem. Gel permeation chromatography of the block copolymer was performed using a series of Waters Ultrastyrogel™ columns (10^5, 10^4, 10^3 Å) connected to a Waters

Differential Refractometer R401 (Cohen Lab). The GPC carrier solvent was toluene running at 1 mL/min flow rate.

Synthetic procedures

To make $MTD_{400}NORCOOH_{50}$ block copolymers we followed the procedures described in detail by Saunders[49] and Clay.[38] The following is a brief summary of the synthetic route, including minor adjustments made to the original routine. First, NORCOOH (2-norbornene-5,6-dicarboxylic acid) monomer (**Figure 1.2**) was synthesized via the Diels-Alder reaction of fumaric acid and cyclopentadiene (obtained from thermal cracking of dicyclopentadiene) in methanol. Here, the author used 1.2 molar equivalence (20% excess) of cyclopentadience per mole of fumaric acid, rather than 2 equivalence as suggested.[49,38]

NORCOOH was next converted to NORCOOTMS (2-norbornene-5,6-dicarboxylic acid-bis trimethylsilyl ester) (**Figure 1.2**). This acid capping procedure was necessary since the Schrock ROMP initiator would otherwise be deactivated by the NORCOOH acid protons. The first capping attempt followed the procedure described by Clay:[38] reacting NORCOOH with 1.1-equivalent (10% excess) pyridine and 1.1-equivalent chlorotrimethylsilane in diethyl ether, followed by recrystallization of the product from pentane and diethyl ether. However, the resulting NORCOOTMS monomer failed to polymerize, likely due to residual unreacted NORCOOH.

For the second capping attempt, 25% excess of both pyridine and chlorotrimethylsilane were used to ensure complete conversion of NORCOOH to NORCOOTMS. All anhydrous solvents were stored over sodium overnight and filtered before use. Also, all filter aids - alumina, celite, and

silica gel - were reactivated prior to use (reactivation was done by heating at 180°C under vacuum for 15 hours.) These procedures were done to minimize the possibility of water contamination. This second batch of NORCOOTMS was successfully polymerized by the initiator, and was used for all subsequent ROMP syntheses.

The sequential polymerization of $MTD_{400}NORCOOTMS_{50}$ diblock copolymer was performed according to Clay,[38] using the Mo initiator. Shown schematically in **Scheme 1.3**, the polymerization of 400 equivalence of MTD units was first allowed to proceed for 35 minutes in sodium-dried toluene. Next, 50 equivalence of NORCOOTMS monomers was added to the living solution and allowed to polymerize for 30 minutes. Polymerization was then termination by adding benzaldehyde (solution color changed from golden-yellow to orange upon benzaldehyde quenching.)

An aliquot of the quenched MTD-NORCOOTMS block copolymer in the original toluene solution was characterized using a gel permeation chromatograph operating with toluene carrier solvent. The measurement was obtained immediately after the aliquot was taken out of the drybox in order to minimize polymer precipitation as a result of exposing NORCOOTMS to ambient moisture. The measured polystyrene-equivalent M_n of the block copolymer was 85 kg/mole, with a 1.05 polydispersity. (Calculated molecular weights for $MTD_{400}NORCOOTMS_{50}$ and $MTD_{400}NORCOOH_{50}$ are 86 kg/mole and 79 kg/mole, respectively.)

Acidification of the NORCOOTMS block (conversion back to NORCOOH) was done by adding deionized water to the toluene solution and stirring overnight, yielding a milky, viscous mixture. Poly($MTD_{400}NORCOOH_{50}$) was precipitated drop-wise from this mixture into pentane. The

recovered solid polymer was washed in pentane and dried under vacuum prior to film casting. Infrared spectroscopy (IR) was also used to characterize films of the block copolymer. Evident carbonyl (C=O) and hydroxyl (O-H) absorption peaks were observed in the block copolymer samples, but were not present in the MTD homopolymer sample (used as a standard); thus, incorporation of NORCOOH into the block copolymer was verified.

1.2.2 Selective metal loading and nanocluster synthesis in bulk poly(MTD_{400}-block-$NORCOOH_{50}$) templates

Materials and Equipment

The following chemicals were used as received: sodium hydroxide (98.9%) and lithium chloride obtained from Mallinckrodt; lead (II) acetate trihydrate from Aldrich; copper (II) acetate monohydrate (98+%), sodium tetrachloropalladate(II) trihydrate (99%), and palladium (II) chloride from Strem. Lithium tetrachloropalladate solution was made by mixing 2:1 molar amounts of lithium chloride and palladium (II) chloride in water. All aqueous salt solutions were made with deionized water. The following salt concentrations were used for the loading experiments: 0.04M NaOH, 0.02M $CuAc_2$, 0.02M $Li_2(PdCl_4)$, 0.4mM $PbAc_2$, 0.01M $Na_2(PdCl_4)$, where Ac = CH_3COO.

Ultra-thin (50-nm) samples for morphological examination were prepared with a Sorvall Ultra Microtome MT5000. Microtomed sections were collected onto 300-mesh gold grids. Cross-sectional morphological investigation was performed on a Jeol 200CX transmission electron microscope operating at 200 kV (CMSE). X-ray diffraction was performed using a Rigaku X-ray diffractometer operating with copper Kα X-ray of wavelength 1.54 angstrom (Cohen Lab). The X-ray point source is generated by a rotating anode at 50kV and 60mA; the beam is filtered

through a Ni foil. UV-visible spectra were obtained with a Cary 5E UV-vis-NIR spectrophotometer illuminated by a tungsten halide lamp (CMSE).

Film casting and metal loading results

The bulk film was statically cast from 1 wt% solution of the $MTD_{400}NORCOOH_{50}$ block copolymer in THF (approximately 100 mg of polymer in 12 mL of THF). Solubilization of the polymer in THF was expedited by warming the solution briefly on a hot plate; the polymer quickly went into solution upon stirring. This was done at the lowest heat setting to prevent the solvent from boiling. (To do this, use only fresh, new THF: aged THF may develop explosive peroxides over time. Still, a safer alternative would be to stir the mixture rigorously at room temperature over several hours, which should eventually solubilize the polymer as well.) The solution was allowed to cool back to room temperature and filtered through a 0.5 μm PTFE syringe filter. Casting was done in a Pyrex glass petri dish with a 5-cm diameter to produce approximately 50-μm-thick film.

In the first film casting attempt, the solvent was allowed to evaporate relatively quickly over approximately 12 hours by placing a cover glass loosely over the dish. Once dried, the surface of the resulting film appeared undulated (not flat) most likely as a result of the relatively fast casting speed. The film was released from glass dish by putting a few drops of deionized water under a raised film's edge and allowing the water to seep in between the film and the glass substrate. The film was then stored under vacuum for 24 hours to remove residual THF and water.

Clay[38] was able to obtain morphology with interconnected NORCOOH domains in MTD matrix via similar static casting procedure. To examine whether the morphology of our block copolymer

was also an interconnected one, we subjected the bulk film to an aqueous loading of $CuAc_{2(aq)}$ as illustrated in **Scheme 1.1B**. (It has been shown that isolated spherical NORCOOH domains in MTD_{800}-block-$NORCOOH_{30}$ are not loadable via the aqueous method since aqueous reagents could not permeate through the MTD matrix.)[36] Metal loading involves first submerging films in a 0.04M $NaOH_{aq}$ solution for 16-24 hrs, followed by a 3-hr rinse in water. The samples were then treated in designated metal salt solution, followed by another 3-hr rinse.

The film developed a blue color similar to the solution color as a result of treatment in the cupric solution (21 hrs). We note that the colors that occur within metal-loaded films usually serve as preliminary indicators of successful uptake of metal ions from aqueous solutions into the samples (except for the cases where metal ions or complexes are colorless; e.g., loading of silver acetate.) Successful copper loading within the film was verified by TEM observation. Shown in **Figure 1.3A**, the morphology is made up of NORCOOH microdomains (exhibiting dark contrasts due to loaded Cu^{2+}) forming an interconnected, worm-like network throughout the MTD matrix, and is believed to be a kinetically locked morphology. (Hexagonally packed NORCOOH cylinders in MTD matrix exhibited by MTD_{400}-block-$NORCOOH_{50}$ have been observed.)[38]

Reduction of sequestered Cu^{2+} ions to form metallic Cu clusters was performed under a hydrogen atmosphere (2 atm at 125°C for 24 hours). The Cu-loaded film's color turned from blue to dark red (nearly opaque) upon reduction, indicating the existence of metallic Cu particles. Successful reduction was also indicated by the absorption peak near 600 nm in the UV-visible absorption spectrum of the sample (**Figure 1.4**) which is attributed to the surface plasmon absorption of Cu nanoclusters.[52,15] The bulk sample's morphology was also verified via TEM. Shown in

Figure1.3B, the web-like NORCOOH microdomains are now decorated with spherical nanoclusters of Cu metal generally a few nanometers in size.

We attempted another casting trial of the block copolymer at a slower THF evaporation rate in order to obtain film with a smoother, more even surface. This was achieved by placing the petri dish containing the polymer solution inside a jar and tightening the cap nearly fully, leaving only a small opening for solvent evaporation. The setup was rested on a stable bench top to minimize vibration during casting. This casting process took about 3 days to complete, and the resulting film exhibits a flatter, more uniform surface relative to the previous casting. TEM shows that the relatively slower casting process leads to a better-defined microphase-separated poly(MTD_{400}-b-$NORCOOH_{50}$) morphology. **Figure 1.5** shows TEM image of a microtomed section from the bulk sample loaded with lead ions (via treatment in 0.4mM $PbAc_{2(aq)}$ solution for 43hrs). The longer-range ordering of the microdomains becomes more evident as a result of slower casting speed. The block copolymer exhibits an approximate periodic domain spacing of ~ 40nm.

The NORCOOH blocks apparently segregate to form thin lamellar layers. The sheet-like structures of the NORCOOH microdomains are clearly portrayed by the rotation of the edge-on lamellae to reveal views through the thin dimensions of the lamellar layers. The disparity in the relative block lengths is represented by the obvious difference in the thickness of the alternating NORCOOH and MTD lamellar layers. In addition, the fact that much of the bulk film is made up of individual grains, each comprising oriented NORCOOH domains in MTD matrix, is shown in **Figure 1.6** (sample treated in $Na_2(PdCl_4)_{aq}$ for 120 hrs.) Connectivity among NORCOOH lamellae is often manifested as the observed ordering defects which generally occur at the boundaries between individual lamellar grains, merging local NORCOOH domains with one another.

Figure 1.7 is a TEM micrograph of a Pd-loaded sample (treated in $Li_2(PdCl_4)_{aq}$ for 92 hrs) that has been subjected to reduction via treatment in a 1wt% $NaBH_{4(aq)}$ solution for 20 hrs. Again, the resulting Pd^0 nanoclusters are uniformly dispersed within the original Pd-loaded NORCOOH domains. Successful reduction of Pd^{2+} ions to Pd^0 was indicated by a change in the color of the bulk film from brown to opaque-black. The reduction was also confirmed by X-ray diffraction: **Figure 1.8** shows an observed enhanced diffraction from the (111) atomic plane of metallic Pd (peak located at $2\Theta = 40.1°$) as a result of the reduction process. As described in the next chapter, the ability to load and reduce palladium within the NORCOOH microdomains is a basis for selective electroless deposition as zero-valent palladium serves as a catalyst for electroless plating.

1.2.3 Summary

The $MTD_{400}NORCOOH_{50}$ block copolymer was successfully synthesized via ring-opening metathesis polymerization technique. It was shown that the microphase separation of the block copolymer upon static casting from THF is dependent on the rate of solvent evaporation: slower casting yields better-defined ordered morphology. The resulting kinetically locked bulk morphology comprises interconnected NORCOOH microdomains of thin lamellae, alternating with thicker layers of the MTD matrix. The block copolymer film was used to reproduce the aqueous-based metal loading and nanocluster synthesis technique previously reported by Clay.[38] Using this same block copolymer as the template for selective electroless plating of metals within the NORCOOH microdomains is the subject of the following chapter.

1.3 References

(1) Flory, P. J. *Principles of Polymer Chemistry*; Cornell University Press: Ithaca, New York, 1953.

(2) Helfand, E.; Wasserman, Z. R. Microdomain structure and the interface in block copolymers. In *Developments in Block Copolymers*; Goodman, I., Ed.; Applied Science Publishers: London, 1982; Vol. 1; pp 99-125.

(3) Bates, F. S.; Fredrickson, G. H. *Annual Review of Physical Chemistry* **1990**, *41*, 525-557.

(4) Hamley, I. W. *The Physics of Block Copolymers*; Oxford University Press: New York, 1998.

(5) Thomas, E. L.; Alward, D. B.; Kinning, D. J.; Martin, D. C.; Handlin, D. L.; Fetters, L. J. *Macromolecules* **1986**, *19*, 2197-2202.

(6) Hajduk, D. A.; Harper, P. E.; Gruner, S. M.; Honeker, C. C.; Kim, G.; Thomas, E. L.; Fetters, L. J. *Macromolecules* **1994**, *27*, 4063-4075.

(7) Khandpur, A. K.; Forster, S.; Bates, F. S.; Hamley, I. W.; Ryan, A. J.; Bras, W.; Almdal, K.; Mortensen, K. *Macromolecules* **1995**, *28*, 8796-8806.

(8) Cowie, J. M. G. Carbon-chain block copolymers and their relationship with solvents. In *Developments in Block Copolymers*; Goodman, I., Ed.; Applied Science Publishers: London, 1982; Vol. 1; pp 1-37.

(9) Price, C. Colloidal properties of block copolymers. In *Developments in Block Copolymers*; Goodman, I., Ed.; Applied Science Publishers: London, 1982; Vol. 1; pp 39-80.

(10) Tuzar, Z.; Kratochvil, P. Micelles of block and graft copolymers in solutions. In *Surface and Colloid Science*; Matijevic, E., Ed.; Plenum Press: New York, 1993; Vol. 15; pp 1-83.

(11) Henglein, A. *Chemical Reviews* **1989**, *89*, 1861-1873.

(12) Davis, S. C.; Klabunde, K. J. *Chemical Reviews* **1982**, *82*, 153-208.

(13) Bahnemann, D. W. *Israel Journal of Chemistry* **1993**, *33*, 115-136.

(14) LesliePelecky, D. L.; Rieke, R. D. *Chemistry of Materials* **1996**, *8*, 1770-1783.

(15) Halperin, W. P. *Reviews of Modern Physics* **1986**, *58*, 533-606.

(16) Stucky, G. D.; Macdougall, J. E. *Science* **1990**, *247*, 669-678.

(17) Bond, G. C. *Surface Science* **1985**, *156*, 966-981.

(18) Sankaran, V.; Yue, J.; Cohen, R. E.; Schrock, R. R.; Silbey, R. J. *Chemistry of Materials* **1993**, *5*, 1133-1142.

(19) Kane, R. S.; Cohen, R. E.; Silbey, R. *Chemistry of Materials* **1996**, *8*, 1919-1924.

(20) Klabunde, K. J.; Habdas, J.; Cardenas-Trivino, G. *Chemistry of Materials* **1989**, *1*, 481.

(21) Elshall, M. S.; Slack, W. *Macromolecules* **1995**, *28*, 8456-8458.

(22) Heilmann, A.; Hamann, C. *Progress in Colloid and Polymer Science* **1991**, *85*, 102.

(23) Watkins, J. J.; McCarthy, T. J. *Chemistry of Materials* **1995**, *7*, 1991.

(24) Antonietti, M.; Wenz, E.; Bronstein, L.; Seregina, M. *Advanced Materials* **1995**, *7*, 1000.

(25) Spatz, J. P.; Roescher, A.; Moller, M. *Advanced Materials* **1996**, *8*, 337-340.

(26) Moffitt, M.; McMahon, L.; Pessel, V.; Eisenberg, A. *Chemistry of Materials* **1995**, *7*, 1185-1192.

(27) Cohen, R. E. Metal nanoclusters (within block copolymer domains). In *Polymeric Materials Encyclopedia*; Salamone, J. C., Ed.; CRC Press: Boca Raton, FL, 1996; Vol. 6; pp 4143-4149.
(28) Ciebien, J. F.; Clay, R. T.; Sohn, B. H.; Cohen, R. E. *New Journal of Chemistry* **1998**, *22*, 685.
(29) Sankaran, V.; Cummins, C. C.; Schrock, R. R.; Cohen, R. E.; Silbey, R. J. *Journal of the American Chemical Society* **1990**, *112*, 6858-6859.
(30) Yue, J.; Sankaran, V.; Cohen, R. E.; Schrock, R. R. *Journal of the American Chemical Society* **1993**, *115*, 4409-4410.
(31) Sohn, B. H.; Cohen, R. E. *Acta Polymerica* **1996**, *47*, 340-343.
(32) Sohn, B. H.; Cohen, R. E. *Journal of Applied Polymer Science* **1997**, *65*, 723-729.
(33) Ciebien, J. F.; Cohen, R. E.; Duran, A. *Supramolecular Science* **1998**, *5*, 31-39.
(34) Yue, J.; Cohen, R. E. *Supramolecular Science* **1994**, *1*, 117-122.
(35) Clay, R. T.; Cohen, R. E. *Supramolecular Science* **1995**, *2*, 183-191.
(36) Clay, R. T.; Cohen, R. E. *Supramolecular Science* **1997**, *4*, 113-119.
(37) Kane, R. S.; Cohen, R. E.; Silbey, R. *Chemistry of Materials* **1999**, *11*, 90-93.
(38) Clay, R. T. Ph.D. Thesis, MIT, 1997.
(39) Clay, R. T.; Cohen, R. E. *Supramolecular Science* **1998**, *5*, 41-48.
(40) Herisson, J. L.; Chauvin, Y. *Die Makromolekulare Chemie* **1970**, *141*, 161-176.
(41) Ivin, K. J. *Olefin metathesis*; Academic Press: New York, 1983.
(42) Schrock, R. R.; Depue, R. T.; Feldman, J.; Yap, K. B.; Yang, D. C.; Davis, W. M.; Park, L.; Dimare, M.; Schofield, M.; Anhaus, J.; Walborsky, E.; Evitt, E.; Kruger, C.; Betz, P. *Organometallics* **1990**, *9*, 2262-2275.
(43) Schrock, R. R.; Murdzek, J. S.; Bazan, G. C.; Robbins, J.; Dimare, M.; Oregan, M. *Journal of the American Chemical Society* **1990**, *112*, 3875-3886.
(44) Nguyen, S. T.; Grubbs, R. H.; Ziller, J. W. *Journal of the American Chemical Society* **1993**, *115*, 9858-9859.
(45) Kanaoka, S.; Grubbs, R. H. *Macromolecules* **1995**, *28*, 4707-4713.
(46) Bazan, G. C.; Schrock, R. R.; Cho, H. N.; Gibson, V. C. *Macromolecules* **1991**, *24*, 4495-4502.
(47) Cummins, C. C.; Beachy, M. D.; Schrock, R. R.; Vale, M. G.; Sankaran, V.; Cohen, R. E. *Chemistry of Materials* **1991**, *3*, 1153-1163.
(48) Chan, Y. N. C.; Craig, G. S. W.; Schrock, R. R.; Cohen, R. E. *Chemistry of Materials* **1992**, *4*, 885.
(49) Saunders, R. S. Ph.D. Thesis, MIT, 1992.
(50) Gratt, J.; Cohen, R. E. *Macromolecules* **1997**, *30*, 3137-3140.
(51) Sohn, B. H.; Gratt, J. A.; Lee, I. K.; Cohen, R. E. *Journal of Applied Polymer Science* **1995**, *58*, 1041-1046.
(52) Bamford, C. R. *Colour Generation and Control in Glass*; Elsevier Scientific: New York, 1977.

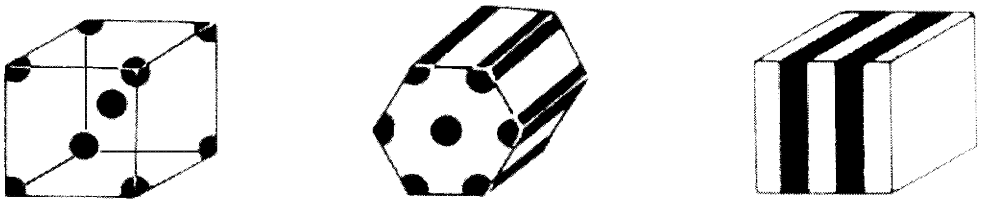

Figure 1.1: Common diblock copolymer microphase-separated morphologies
(adapted from Cowie, 1982)

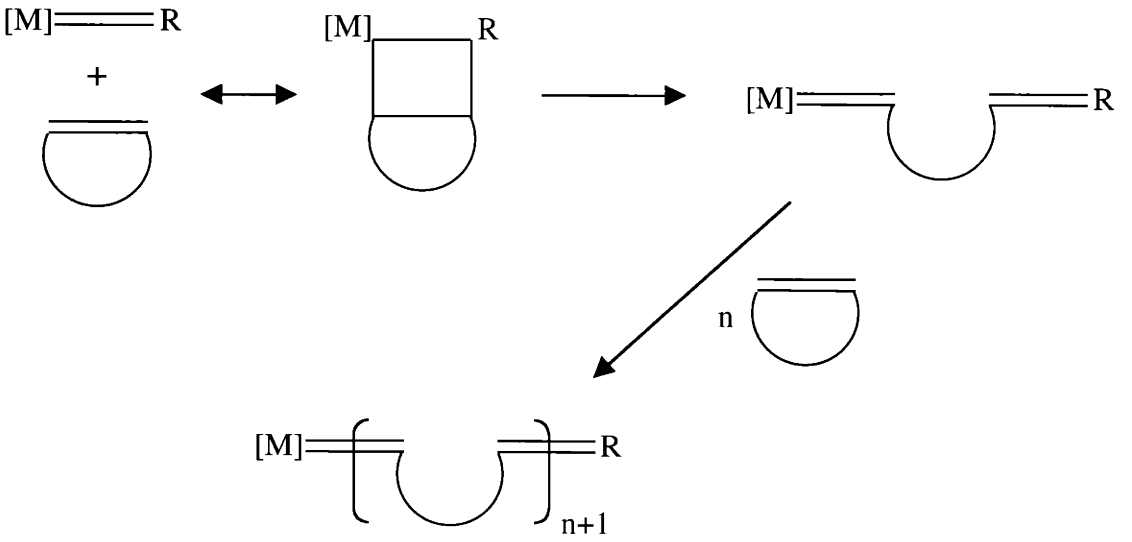

Scheme 1.2: Ring-opening metathesis polymerization (ROMP) of cyclic olefin

Scheme 1.1: (A) Generalized Loading Scheme (Yue et al., 1994)
(B) Aqueous Load-and-Reduction Sequence ('LARS') (Clay et al., 1998)

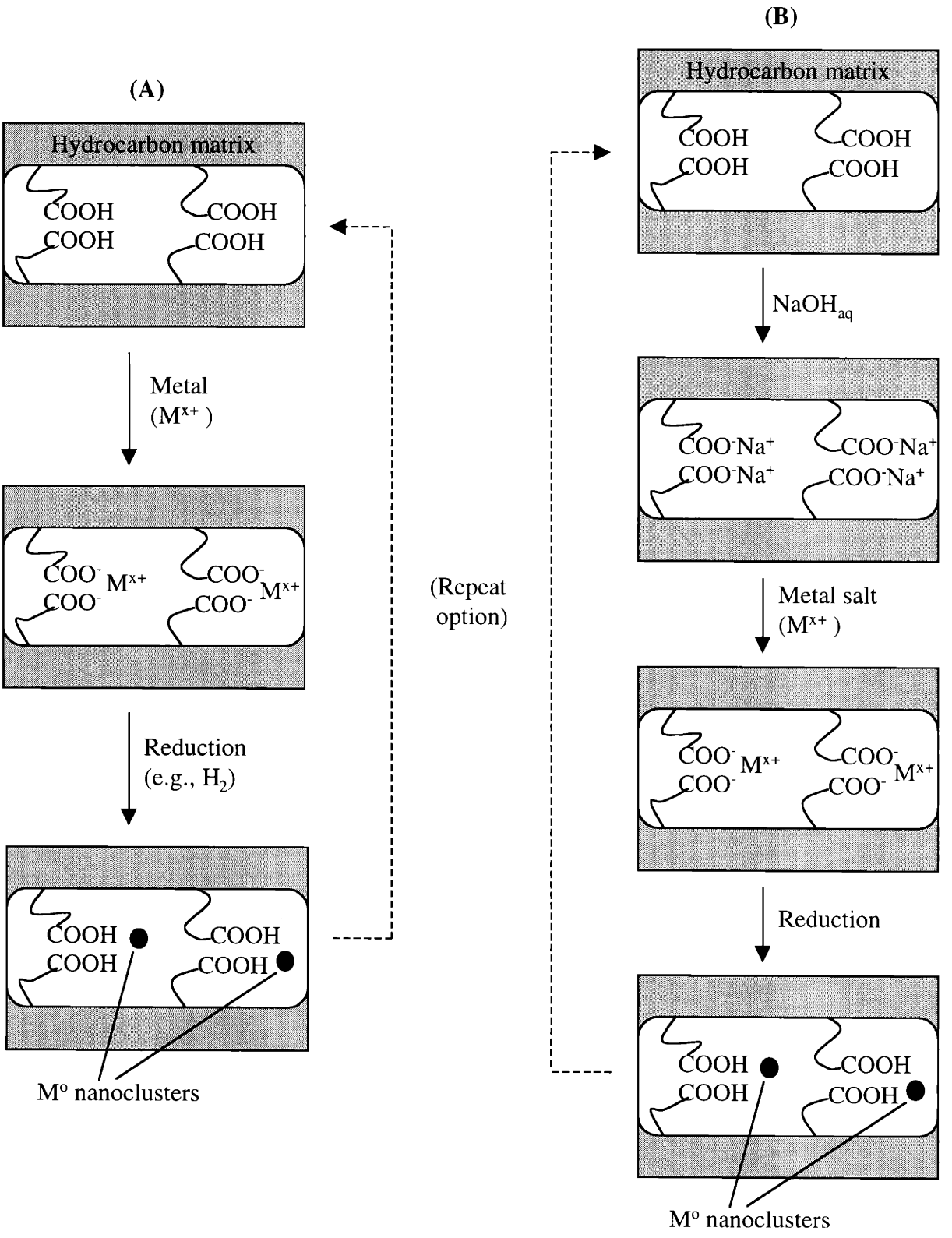

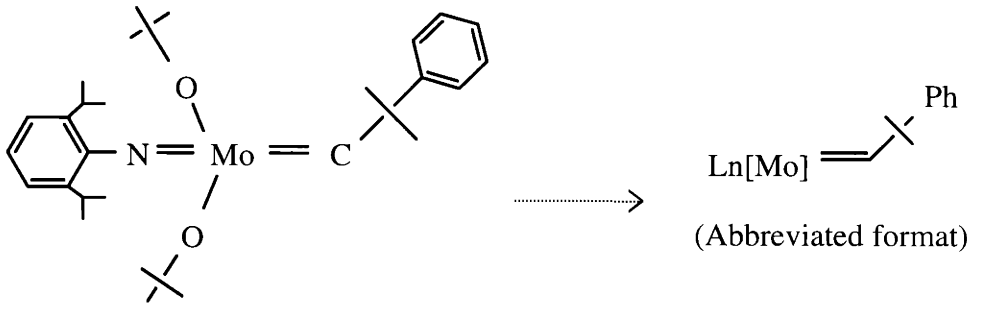

Mo-based ROMP (Schrock) initiator

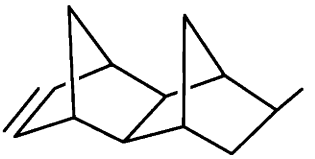

Methyltetracyclododecene (MTD)

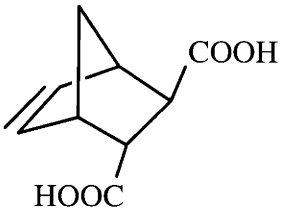

2-Norbornene-5,6-dicarboxylic acid
(NORCOOH)

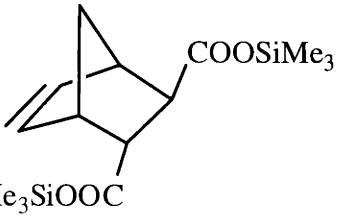

2-Norbornene-5,6-dicarboxylic acid-bis trimethylsilyl esther
(NORCOOTMS)

Figure 1.2: Mo-based ROMP initiator and relevant ROMP monomers

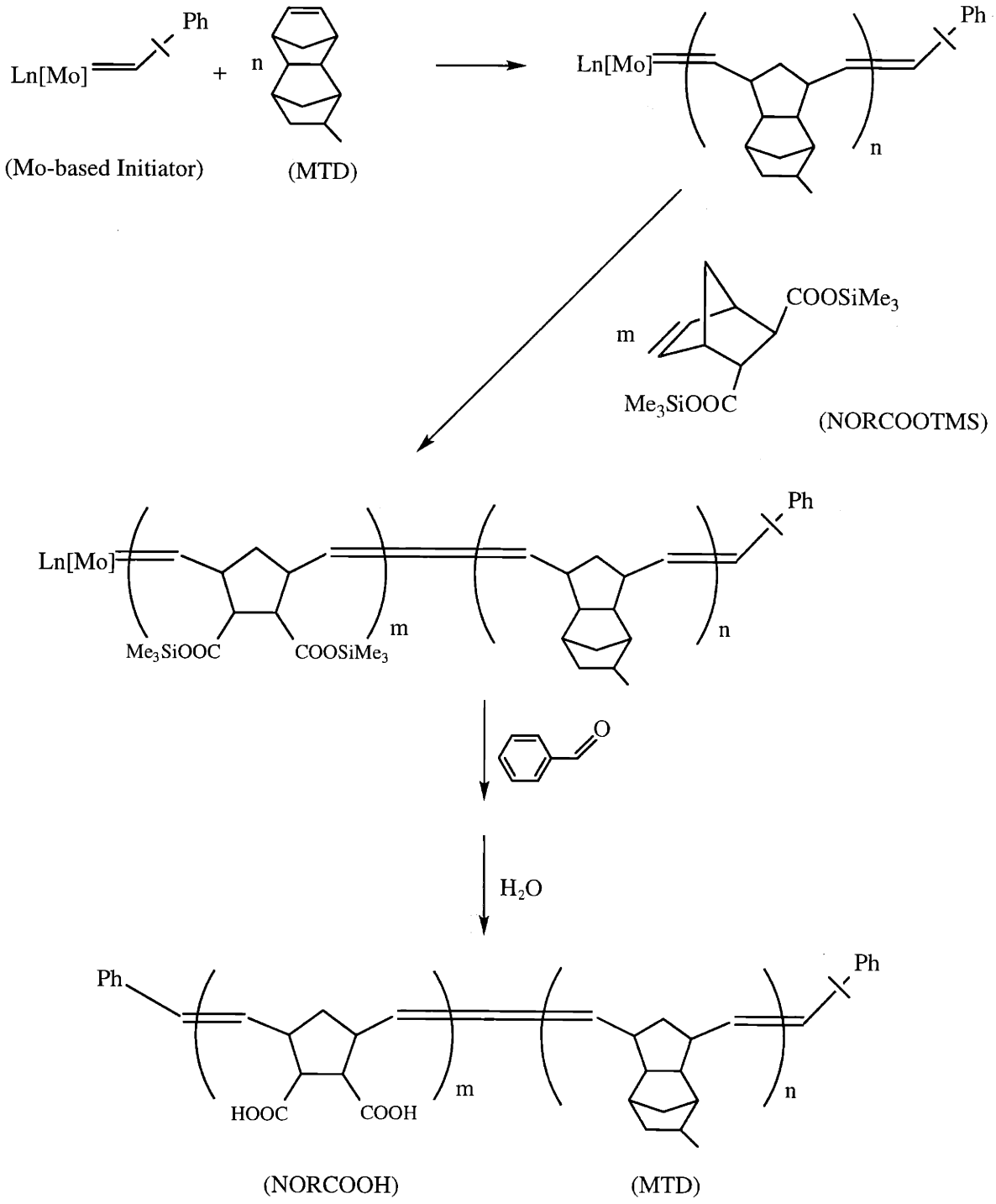

Scheme 1.3: Ring-opening metathesis polymerization of MTD-block-NORCOOH

(A)

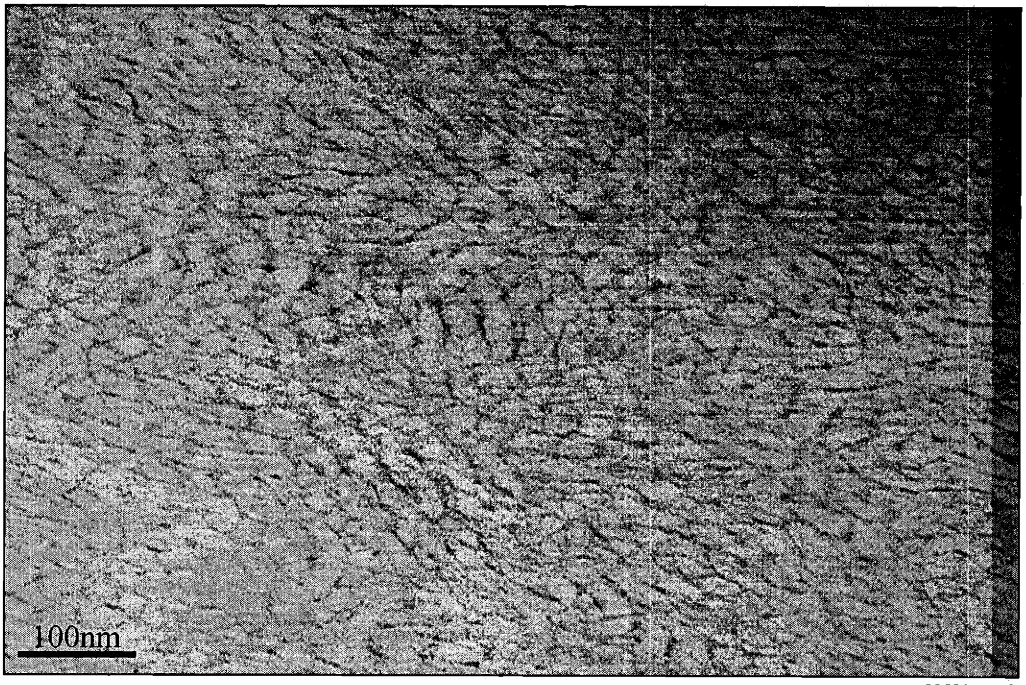

83591copy3

(B)

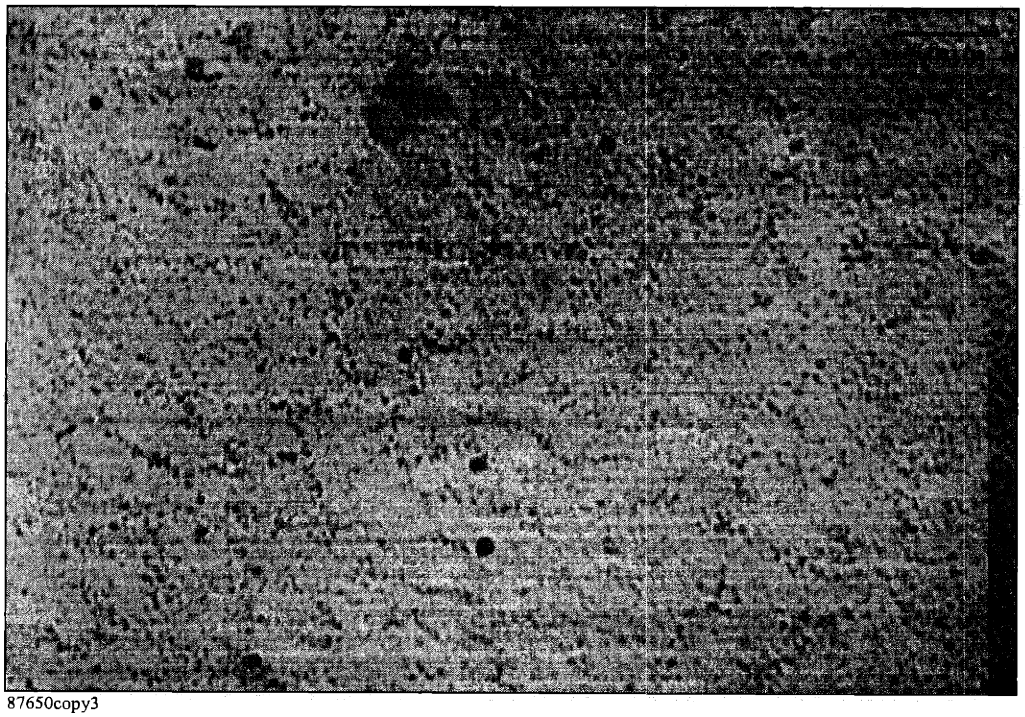

87650copy3

Figure 1.3: Poly(MTD_{400}-b-$NORCOOH_{50}$)
(A) loaded with $CuAc_{2(aq)}$
(B) reduced with $H_{2(g)}$

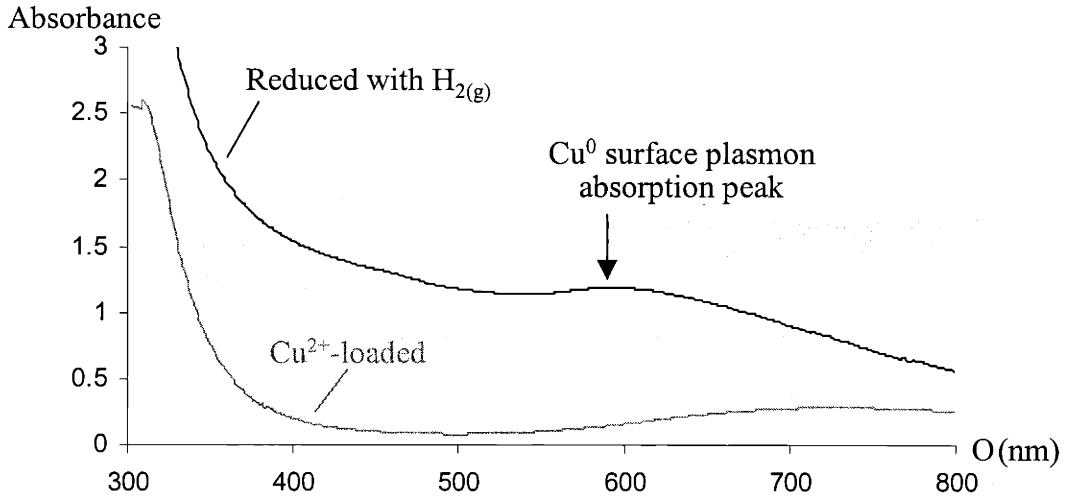

Figure 1.4: UV-visible absorption spectra of $CuAc_{2(aq)}$-loaded sample before and after reduction to Cu^0

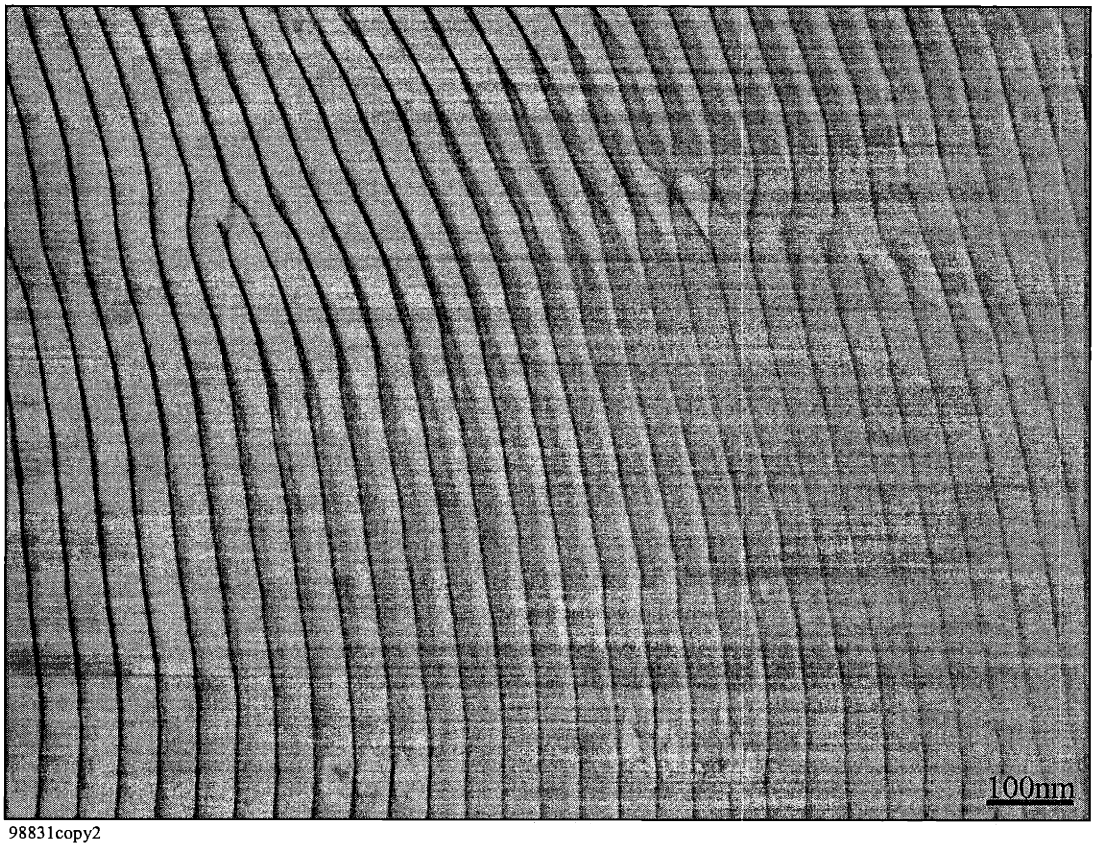

Figure 1.5: Poly(MTD_{400}-b-$NORCOOH_{50}$) loaded with $PbAc_{2(aq)}$

Figure 1.6: Poly(MTD_{400}-b-$NORCOOH_{50}$) loaded with $Na_2(PdCl_4)_{(aq)}$

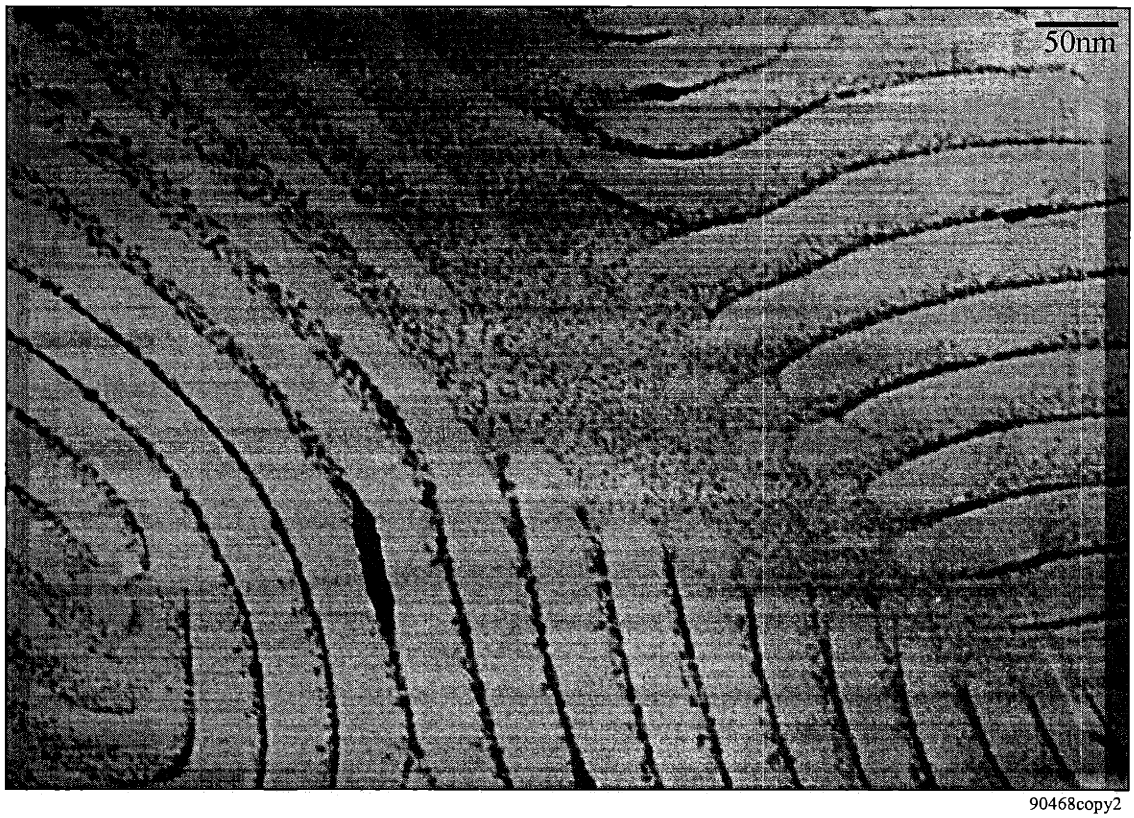

Figure 1.7: Poly(MTD_{400}-b-$NORCOOH_{50}$) loaded with $Li_2(PdCl_4)_{aq}$ and reduced in $NaBH_{4(aq)}$

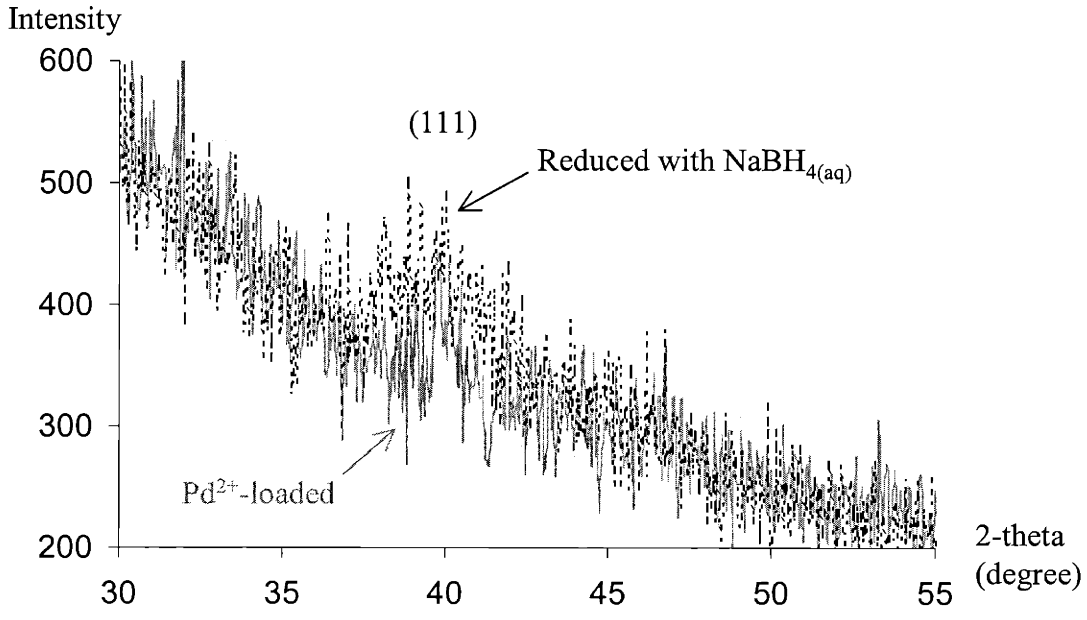

Figure 1.8: X-ray diffraction spectra of sample loaded with $Li_2(PdCl_4)_{aq}$ before and after reduction to Pd^0

Chapter 2

Selective Electroless Metal Deposition within Block Copolymer Domains

2.1. Introduction

As illustrated by Clay et al.[1,2] (see also Chapter 1), the load-and-reduction sequence (LARS) represents a simple method for depositing in-situ metallic nanoclusters in water-permeable block copolymer microdomains. Clay demonstrated that the amount of metal incorporated into the NORCOOH microdomains can be increased by repeating the LARS cycle multiple times, as illustrated conceptually in **Scheme 1.1B**. However, in practice such sequential process turned out to be time-consuming and inefficient since the LARS method relies on the stoichiometry-limited amount of reagents that can be sequestered into the nanoreactors upon each loading cycle. In addition, studies of repeated LARS trials revealed that the amount of metal (e.g., silver ions from silver acetate solution to create Ag clusters) sequestered into the polymer microdomains decreases with each additional loading cycle.[1] Even after several-repeated LARS cycles, the resulting distribution of the in-situ Ag clusters within the NORCOOH microdomains still is generally sparse. These limitations of the LARS method provided us with the motivation to investigate a potentially more efficient method for increasing the amount and density of deposited metal in the block copolymer microdomains, namely electroless metal deposition.

Since the report of its discovery in 1946, electroless metal deposition has developed into a commercially important method for surface coating and finishing.[3-6] As a means to create uniform metal coatings over various surfaces regardless of shapes and sizes, electroless plating has found applications in various industrial products, e.g., automotive parts, tools, printed circuit boards. Among many advantages offered by electroless plating is the fact that the surface to be plated needs not be electrically conductive. As a result, this versatile technique has been widely

employed to plate metals over surfaces of non-conductors (polymers, ceramics, etc.) onto which metalization could not be achieved via conventional electrochemical deposition processes.

Electroless deposition involves chemical reduction of metal cations from an aqueous solution. The non-electrolytic process is generally initiated onto a surface that has previously been activated by a noble metal catalyst, e.g., palladium. Once initiated, the deposition is sustained as the surface of the previously plated metal itself serves as catalyst for further reduction of metal ions from solution; hence, an auto-catalytic process. Such process continues as long as the electroless bath condition is kept operational via proper replenishment and maintenance.

Basic components in an electroless bath include a source of metal ions, a reducing agent (e.g., formaldehyde, hypophosphite, dimethylamine borane, etc), a complexing agent (tartrate, EDTA, etc.) to stabilize the metal ions in solution, and a buffering agent. The following is an example of an electroless copper redox mechanism which comprises the oxidation of formaldehyde and the reduction of the cupric ion complex, resulting in the deposition of zero-valence metallic copper onto the catalytic surface.[3,6,7]

$$Cu^{2+} + 2HCHO + 4OH^- \rightarrow Cu^0 + 2HCOO^- + H_2 + 2H_2O$$

A variety of metals can be deposited via electroless deposition, copper and nickel being the most common. Other electroless metals include cobalt, gold, palladium, silver, tin, etc. There are usually a number of bath formulae for a given electroless metal. The bath chemistry and conditions (e.g., temperature) can be adjusted to achieve the desired deposition rate, bath stability, as well as physical and chemical properties of the plated metals. For example, electroless nickel baths with hypophosphite as the reductant yield Ni-P alloys as the plating products, of which properties vary with the amount of phosphorus incorporated.[3]

In addition to its conventional applications in surface metalization of large industrial components, electroless plating has also been shown recently an effective mean to create uniform metal coatings over small, template-directed surface areas.[8-10] For example, Whitesides et al.[11,12] demonstrated the confinement of an electroless copper growth within sub-micron patterns created by stamping palladium colloids onto surfaces via microcontact printing.

Prior to our report of this work,[13] block copolymer morphologies had already been employed as templates for the directed metalization of nanoscale surface structures via electroless plating in recent years. In particular, Zehner et al.[14] selectively decorated the surface morphology of lamellar diblock copolymer films with palladium colloids. The Pd-decorated lamellae in turn served as template for electroless deposition, which resulted in a surface pattern of 20-nm copper structures. In another example, Hashimoto et al.[15] created void nanochannels inside the styrene matrix of a bicontinuous styrene-isoprene block copolymer via selective degradation of the pre-existing isoprene microdomains. The surfaces of the 30-nm void network were then coated with nickel via electroless deposition.

While we also employ microphase-separated block copolymers as templates for the selective electroless deposition, a distinction of our work from the aforementioned reports is our attempt to apply electroless plating beyond the surface regime. Based on previous works by our research group, we postulated that palladium selectively pre-loaded into the NORCOOH microdomains could serve as localized catalyst to initiate selective electroless plating in our block copolymers. Therefore, our goal was to induce electroless plating to occur within the sub-surface microdomains of our bulk block copolymer, without the need for prior physical modifications to the polymer microstructure.

In the following sections, we demonstrate that the electroless deposition process represents an effective and efficient alternative to the 'serial' LARS method. The continuous nature of electroless plating leads to relatively rapid growth of dense metallic structures inside the block copolymer microdomains. The method relies on the diffusion of electroless plating reagents from the external reservoir through the water-permeable NORCOOH lamellar network embedded in the MTD hydrocarbon block matrix. These same lamellar microdomains also serve as templates for selective metal deposition, with certain limitations on reagent transport as described below. In the case of our lamellar morphology, we demonstrate the successful formation of metallic layers inside the three-dimensional sub-surface morphology of our block copolymer.

2.2 Experimental

Materials

Poly($MTD_{400}NORCOOH_{50}$) diblock copolymer was synthesized as previously reported.[16] A 50-μm-thick film was statically cast from a 1 weight-percent THF solution in a glass petri dish over approximately 3 days. The resulting light-brown, transparent film was dried under vacuum before use (see also section 1.2). Sodium tetrachloropalladate(II) trihydrate (99%), copper(II)sulfate pentahydrate (98+%), and dimethylcadmium (99+%) were purchased from Strem. Triethanolamine (97%), dimethylamine borane (DMAB) (98+%), and 1,5,8,12-tetraazadodecane (96.5+%) were purchased from Fisher Scientific. Sodium potassium tartrate tetrahydrate (99%) and formaldehyde (37wt % aqueous solution) were obtained from Aldrich. Sodium hydroxide (98.9%) and sodium sulfate (anhydrous, 99.5%) were obtained from Mallinckrodt. Nickel (II) sulfate hexahydrate was purchased from Sigma Chemicals. Cobalt (II) sulfate heptahydrate (100%), sodium succinate hexahydrate, sodium citrate dihydrate (99%), and lactic acid (85-90%)

were obtained from Alfa Aesar. All reagents were used as received. All aqueous solutions were prepared with de-ionized water.

Palladium Loading and Electroless Copper Deposition (see **Scheme 2.1**)

Pre-treatment of bulk block copolymer films in 0.04M $NaOH_{aq}$ solution to convert the carboxyl groups (NORCOOH) to sodium carboxylate form (NORCOO-Na+) was done by immersing block copolymer films in a solution for 16-24 hours, followed by rinsing in de-ionized water for 2 hours. Dispersion of palladium into the NORCOOH microdomains was done by immersing films in a 0.01M $Na_2(PdCl_4)_{aq}$ solution: for 3-4 days, followed by a 3-hr rinse (section 2.3.1); and for 1 hour, followed by a 20-minute rinse ('light' pre-loading, sections 2.3.2 & 2.4). The Pd-containing films were then immersed in their respective electroless metal plating baths.

Electron Microscopy

Ultra-thin (50-nm) samples for morphological examination were prepared with a Sorvall Ultra Microtome MT5000. Microtomed sections were collected onto 300-mesh gold grids. Cross-sectional morphological investigation and electron diffraction were performed on a Jeol 200CX and on a Jeol 2000FX transmission electron microscope operating at 200 kV (CMSE). Scanning transmission electron microscopy was performed on a VG-HB603 operating at 250 kV (CMSE).

Elemental analysis

Quantitative elemental copper analyses of our bulk block copolymer samples that had been subjected to a series of copper loading tests (**Table 2.2**) were performed by Galbraith Laboratories, Inc. (Knoxville, TN). The copper-containing films were first aqueously solubilized via the 'wet ash digestion' method. The copper concentrations in these digested solutions were then measured using inductively coupled plasma (ICP) emission spectroscopy.

2.3 Selective electroless copper deposition within block copolymer microdomains

2.3.1 Formula I: Initial trials

We began our electroless deposition experiments with an electroless copper since the electroless deposition of copper has been well documented. While there are many bath formulations to choose from, the majority described in the literature are formaldehyde-based. The reducing action of formaldehyde is most effective above pH 12, and a relatively high concentration of NaOH is normally employed for pH adjustment in formaldehyde-based baths.[3,4,6] Goldie[17] conducted extensive studies on the plating kinetics of a series of simple 4-component formaldehyde-based electroless copper baths. We chose to start our effort with the 'weak' bath (see **Table 2.1** for components) presented in the report based on its superior stability. We will refer to this electroless bath as **'Formula I'** bath for simplicity.

Table 2.1: Electroless copper plating bath **Formula I** (from Goldie[17])

1. Copper (II) sulfate pentahydrate	0.02 M (5 g/L)
2. Sodium potassium tartrate tetrahydrate 'Rochelle salt' (complexant)	0.089 M (25 g/L)
3. Sodium hydroxide (pH adjustor)	0.125 M (5 g/L)
4. Formaldehyde (reductant) (37 wt % aqueous solution)	0.133 M (10 mL/L)

Static casting of poly(MTD_{400}-block-$NORCOOH_{50}$) (structure in **Scheme 1.3**) yields the lamellar morphology in which the acid-functionalized (NORCOOH) block forms interconnected lamellar microdomains within the matrix of the hydrocarbon (MTD) block (see also Chapter 1.) Prior to electroless copper deposition, the 50-μm-thick diblock copolymer film was treated with $NaOH_{aq}$ solution to convert the acid groups into sodium carboxylate salt which, in turn, facilitates[1] the selective loading of palladium ions upon immersion of the film in the aqueous solution of $Na_2(PdCl_4)$.

The block copolymer's morphology is shown in **Figure 2.1A**, where the loaded palladium imparts a uniform dark contrast to the NORCOOH microdomains. The bulk of the film is made up of randomly oriented lamellar grains with an approximate lamellar long period of 40 nm. The NORCOOH microdomain thickness observed from the lamellar edge-on view is about 4 nm. Note that though the majority of lamellae are arranged in grains, we often find that within several microns from the film's free surface the lamellae orient themselves parallel to the plane of the free surface, as shown in **Figure 2.1B**. (The arrow indicates the direction towards the free surface.)

It has been previously concluded that the transport of aqueous reagents into the MTD_{400}-$NORCOOH_{50}$ block copolymer films occurs mainly through the interconnected NORCOOH microdomain network rather than through the hydrophobic MTD matrix.[18] Since electroless plating was expected to also take place selectively along these same NORCOOH 'paths', we realized the need to employ slow plating rates. This was to prevent premature 'clogging' of the NORCOOH domains near the film's free surface through which plating reagents would diffuse into the bulk of the film. To lower the deposition rate, our first plating trial was performed at half the bath concentration as listed in **Table 2.1**.

A free-standing MTD400-NORCOOH50 block copolymer film sample, pre-loaded with palladium $Na_2(PdCl_4)$, was submerged in such electroless copper bath. After about 45 minutes of treatment, the sample appeared to have a small amount of macroscopic copper plated on the free surfaces. Plating was allowed to continue for a total of 20 hrs before the sample was removed from the bath. TEM micrographs of the sample, **Figures 2.2 (A,B)**, show the representative morphology near the film's free surface. In comparison to the Pd-loaded sample prior to the electroless plating treatment (**Figure 2.1**), the contrast between the plated NORCOOH domains

and the MTD domains has become much more prominent due to the selective plating of relatively dense copper deposits in the NORCOOH lamellae. The maximum observed depth of selective copper deposition reached ~ 1μm into the bulk of the film from free surface.

Figure 2.3 illustrates an area further into the bulk of film where no copper plating occurred. The pre-loaded Pd^{2+} ions, which impart uniform staining contrast to the NORCOOH lamellae (see **Figure2.1**), have been transformed into zero-valent nanoclusters as a result of the reduction upon treatment in the electroless bath. The reduction of Pd^{2+} ions to zero-valent Pd - the active catalyst for electroless deposition - upon exposure to the reductant (formaldehyde) in similar electroless copper baths has been previously reported.[7]

Even though we succeed in inducing some selective electroless deposition within the sub-surface NORCOOH microdomains in this first trial, the depth of copper deposition was still rather superficial. Our next goal was to be able to extend the deposition of electroless copper further into the bulk of the film. We attempted to achieve this by further diluting the plating bath concentration to slow down the potential 'clogging' of the NORCOOH 'paths' to allow more time for the permeation of plating reagents into the bulk of the film. However, TEM observation of such samples revealed no improvement in the extent of plated copper in the sub-surface microdomains, possibly due to inadequate supply of the plating reagents as a result of excessive dilution.

We also attempted plating experiments at a higher plating rate using the original bath concentration as listed in **Table 2.1**. This yielded significant macroscopic plating on the film's surfaces soon after the start of treatment. TEM investigation was not performed on these samples

as the thick surface plating likely blocked the diffusion of plating reagents into the bulk of the film, and no improvement in the deposition extent was expected. (This was indeed the trend we observed in the experiments discussed in the following section, using another electroless copper bath formula.)

The above initial trials were done assuming efficient transport of the electroless plating reagents through the interconnected NORCOOH microdomains. However, as described by Clay et al.,[18] the loading capacity of a given metal cationic species into the NORCOOH domains varies significantly depending on the type of metal salt employed. Our limited success in promoting extensive electroless deposition in the NORCOOH domains raised a question regarding the uptake of the plating reagents into the block copolymer microdomains.

To investigate the transport of electroless plating reagents into the bulk film, we performed a series of loading tests using several sources of aqueous Cu^{2+} ions shown in **Table 2.2**. Free-standing film samples used for these loading experiments were pre-treated in NaOH prior to treatment in the respective solutions (refer to the LARS technique[1]) but not pre-loaded with Pd.

Table 2.2: Results of loading tests from different copper-containing sources into bulk block copolymer films (Ac = acetate = CH_3COO)

Sample / Loading solution	Order of film color intensity (blue)	% (wt) loaded copper
A. $CuAc_2$ (0.02M)	1st	5.54
B. $CuSO_4$ (0.02M)	2nd	3.23
C. $CuSO_4$ (0.02M) + Rochelle salt (0.089M)	3rd (very pale blue)	2.21
D. $CuSO_4$ (0.02M) + Rochelle salt (0.089M) + NaOH (0.125M)	4th (colorless)	Not detectable (< 0.05)

After ~4 days of treatment, films treated in $CuAc_2$ (sample A) and $CuSO_4$ (sample B) solutions appeared blue; sample A was more blue than B. (It is interesting to note that the blue color of film B was visibly brighter/deeper than the pale blue tint of the aqueous $CuSO_4$ solution itself.) Sample C ($CuSO_4$ + Rochelle salt) turned out very pale blue, and sample D ($CuSO_4$ + Rochelle + NaOH) appeared essentially the same as before the treatment (i.e., colorless). Based on the author's previous observations, the intensity of the block copolymer film's color upon loading experiments usually serves as preliminary indicator for the amount of metal ions (e.g., Cu^{2+}, Pd^{2+} - see also Chapter 1) absorbed into the NORCOOH domains. Hence, the order of color intensity displayed by the 4 test samples suggested that the relative amounts of copper uptake decreased in the order: A > B > C > D.

Results from subsequent quantitative elemental copper analyses of these 4 samples are in good agreement with the trends offered by the preliminary visual observations (**Table 2.2**). The sample treated in $CuAc_2$ solution contains the highest amount of copper ions. The addition of Rochelle salt to the $CuSO_4$ solution (B to C) reduces the amount of sequestered copper in the NORCOOH microdomains of the block copolymer film. Sample from solution D, which comprises all the same components as Formula I electroless copper bath listed in **Table 2.1**, but without formaldehyde, contained an undetectably small amount of loaded copper. A similar loading test using the complete Formula I electroless copper bath (with formaldehyde) was also performed; the resulting film also turned out colorless, suggesting that once again only a small amount of copper, if any, existed in the sample.

The results of the loading tests described above indicated poor transport of plating reagents (represented by the copper uptake) from the electroless copper bath (Formula I) into the block

copolymer. It was, therefore, reasonable to conclude that significant extent of copper plating could not be achieved via such a plating bath due to the absence of favorable permeation of plating reagents into the bulk of the film. We also performed some of these loading tests using block copolymer samples that were not pre-treated with NaOH; all of which turned out essentially colorless, indicating the absence of copper ion uptake. This is in agreement with previous studies by Clay et al.[1] who showed that loading of metal ions into the NORCOOH microdomains is much less efficient without the conversion of the (protonated) carboxyl groups to sodium carboxylates (i.e., NORCOOH to NORCOONa). The author believes that this general trend can be attributed in part to the fact that sodium carboxylate groups are more hydrophilic and thus more readily hydrated than the protonated counterparts.

At this point we decided that an investigation into other electroless copper bath formulae was necessary. Note from **Table 2.2** that the addition of NaOH (solution C to D) drastically lowered the amount of loaded copper ions to an insignificant level. This observation suggested that NaOH may be a factor contributing to the poor absorption of plating reagents. Although such hypothesis was not further verified, we employed this observation as a guideline to focus our search for a new electroless copper bath formula that did not contain NaOH. The details of these subsequent electroless copper deposition experiments are described in the next section.

2.3.2 Formula II: Optimization and deposition control

Our second set of electroless plating experiments were performed using the bath formulation described by Jagannathan and Krishnan.[19] The bath composition, which does not contain NaOH, is shown in **Table 2.3**. We will refer to this second electroless copper bath as **'Formula II'** bath for simplicity.

Table 2.3: Electroless copper plating bath **Formula II** (from Jagannathan&Krishnan[19])

1. Copper (II) sulfate pentahydrate	0.032 M (8 g/L)
2. Tetraazadodecane (complexant)	0.04 M (7 g/L)
3. Triethanolamine (buffering agent)	0.3 M (45 g/L)
4. Dimethylamine borane (DMAB) (reductant)	0.067 M (4 g/L) (**'fast-plating'**) 0.017 M (1 g/L) (**'slow-plating'**)

Preliminary loading tests similar to those described in previous section, using block copolymer samples pre-treated in $NaOH_{aq}$ solution, were performed to asses the transport of plating reagents into the NORCOOH domains. Upon treatment in the electroless copper solution, the block copolymer films turned purple (the same color as the plating bath). We interpreted this result as an indication of successful permeation of the electroless plating reagents into the film, and proceeded with our plating experiments using this Formula II electroless copper bath. Once again, no color was observed in loading tests using samples not pre-treated with NaOH. This supports our previous observations that the NORCOONa microdomains are generally more accessible to external aqueous reagents than the NORCOOH counterparts.

As described in the report[19], the plating rate of the electroless copper bath decreases with decreasing concentration of the reductant (DMAB). In this work, we employed 2 different concentrations of DMAB in order to control the rate of copper deposition (see **Table 2.3**). We will designate baths containing 0.017M DMAB as **'slow-plating'** baths, while **'fast-plating'** baths are those that contain 0.067M DMAB.

An additional modification to the previous trials, in an effort to maximize the extent of copper plating in the sub-surface NORCOOH domains, was to reduce the amount of palladium pre-loaded into the microdomains. We anticipated that a reduced amount of Pd catalyst would lead to

a slower 'clogging' of the NORCOOH microdomains; thus, allowing more time for the diffusion of plating reagents through the bulk NORCOOH network from film's free surfaces. Such modification was achieved by shortening the sample treatment time in the $Na_2(PdCl_4)$ solution to only 1 hr, resulting in a light brown color imparted to the block copolymer film. In comparison, the samples used for Formula I plating trials (previous section) were treated in the $Na_2(PdCl_4)$ solution for 3-4 days; these heavily loaded samples appeared dark-brown in color. TEM observations also revealed a corresponding reduction in the dark contrast of the stained NORCOOH microdomains due to the smaller amount of loaded Pd.

The (lightly) palladium-loaded films were then submerged in an electroless copper bath (**'slow-plating'** bath: 0.017M DMAB) for 16 hours, where the spatially sequestered palladium served as localized catalyst for the copper deposition process. **Figure 2.4** is a TEM micrograph of such sample, in which selective copper deposition along the lamellae of the NORCOOH microdomains appears dark and dense. In comparison with our initial electroless plating trials (Formula I, previous section), the depth of selective copper deposition into the bulk of the film achieved in this trial (over 4 microns) is clearly more extensive. We attribute this relative success to the improved transport of the Formula II electroless plating reagents through the sample from the film's free surfaces.

Scanning transmission electron microscopy (STEM, energy disperse X-ray analysis) was performed on the copper-treated sample in order to verify the correlation between the dense structure observed in bright-field TEM and the copper deposition. **Figure 2.5 (A,B)** shows side-by-side images of a bright-field image and the corresponding copper map. The dark structure in the bright-field image correlates well with the structure of the copper map (where light contrast indicates copper); thus confirming the identity of such structure as a copper deposit.

We also performed selected-area electron diffraction of microtomed samples (on gold TEM grids). The resulting diffraction pattern (**Figure 2.6**) consists of multiple rings, consistent with a polycrystalline copper structure. The corresponding atomic plane spacing values were calculated from the diffraction ring radii using the Bragg equation (**Table 2.4**). The d-spacing values derived from the 6 most intense diffraction rings match the face-centered cubic lattice plane spacings of copper metal.[20]

Table 2.4: Atomic plane spacing values derived from the diffraction pattern

Cu[20]						
D (Å)	2.008	1.808	1.278	1.090	0.829	0.808
(h, k, l)	(1, 1, 1)	(2, 0, 0)	(2, 2, 0)	(3, 1, 1)	(3, 3, 1)	(4, 2, 0)
Measurement						
D (Å)	2.074	1.815	1.286	1.096	0.830	0.814
Error (%)	-0.66	0.39	0.62	0.54	0.05	0.73

Figures 2.4 and **2.5** reveal a gradient in the apparent density and thickness of the copper deposit, which exists from the free surface towards the center of the film. **Figure 2.7 (A,B)** are higher-magnification images of a similarly treated sample taken at regions adjacent to and approximately 3.5 μm away from the sample's free surface, respectively. The deposit appears dense and continuous near the free surface, having an estimated lamellar thickness of 25 nm and a lamellar period of 55 nm. At 3.5 μm away from the same free surface, the copper deposit forms individual, roughly spherical clusters of size 15 - 20 nm along the NORCOOH microdomains with a 40-nm lamellar period.

We emphasize the spatially confined production of the copper structure inside the pre-existing lamellar microdomains of the NORCOOH block and the virtual absence of copper inside the alternating layers of the MTD hydrocarbon block. Extensive growth of copper near the film's

surface is evident from the observed thickening of the deposited copper beyond the original NORCOOH microdomain thickness (and the corresponding expansion of the lamellar period), as well as the deposition-induced buckling of the lamellae. Nevertheless, we have seen no evidence of any 'break-out' events where the growth of the copper structure overwhelmed the pre-existing lamellar morphology of the block copolymer.

The observed selective deposition along the NORCOOH microdomains in the absence of 'break-out' indicates that the transport of plating reagents occurs mainly through the NORCOOH microdomains. That is, the palladium-doped NORCOOH network serves a dual role, both as the reagent transport pathway and as the template for copper deposition. The observed gradient of copper deposit density perpendicular to the free surface evidently resulted from limitations on the supply of the plating reagents to the NORCOOH microdomains further away from the film's free surface compared to those microdomains located near the free surface. The diffusion of these reagents from the free surface towards the bulk of the film may also become further limited as the transport path near the free surface becomes increasingly clogged by the growing copper deposit.

Along this line of reasoning, we expected that an increased plating rate might result in a more rapid clogging of the NORCOOH network, which could lead to a reduced deposition depth. **Figure 2.8 (A,B)** are TEM micrographs of samples plated in **'fast-plating'** baths (0.067M DMAB) for 1.8 hours and 16 hours, respectively. The 'fast-plating' bath has approximately 3 times the plating rate of the 'slow-plating' bath[19] (0.017M DMAB) which was used in all of the experiments discussed thus far. By comparison, for the same plating time of 16 hours, the fast-plating sample (**Figure 2.8B**) exhibits a much smaller copper deposition depth than the slow-plating sample (**Figure 2.4**). (Notice in **Figure 2.8** that the light TEM contrast of loaded

palladium is clearly distinguishable from the heavy contrast near the free surface of the copper deposit.)

While this observation may be attributed to the rate of clogging of the NORCOOH nanochannels, macroscopic deposition of copper on the fast-plating sample's free surfaces may have also contributed a macroscopic retardation to the diffusion of plating reagents into the bulk of the film. We note that the free surfaces of the fast-plating sample are visibly covered with solid copper coatings, while the slow-plating sample's copper coatings are very sparse in comparison.

Aside from adjusting the deposition rate, we were also able to control the depth of copper deposit by varying the plating time, i.e., time allowed for the diffusion of plating reagents into the film. After 16 hours of slow-plating, the maximum depth of copper deposit is approximately 4 μm (**Figure 2.4**), compared to the approximate 8-μm depth of copper deposit after 41 hours shown in **Figure 2.9**. We also observed an increase in copper deposit depth with an increase in plating time in fast-plating samples (**Figure 2.8A**: 1.8 hours plating time, compared to **Figure 2.8B**: 16 hours).

Our preliminary attempt to investigate qualitatively the connectivity of the copper deposit was to view the copper structure through the lamellae's thin dimensions. **Figure 2.10** shows a region of a specimen in which the edge-on lamellae rotate to reveal the lamellar planes. The upper section of **Figure 2.10** represents a transmission view through the thin dimensions of single copper-plated lamellar layers since the thickness of microtomed sections was 50nm, which is approximately equal to the lamellar period. At this length scale, the deposit appears to be a collection of spherical copper clusters in close contact with one another. That is, though not fully dense, the structure of the individual copper layers appears to be percolated.

2.4 Selective electroless deposition of cobalt & nickel

In the previous section we confined our comments to the observations of electroless copper deposition in a lamellar block copolymer. We also recognized the possibility of depositing other metals, with potentially interesting properties different from those of the lamellar copper structure (e.g., magnetic nickel and cobalt). To demonstrate the application of our approach to selectively deposit other electroless metals within the block copolymer microdomains, we conducted preliminary plating experiments using electroless plating of nickel and cobalt.

The 50-μm-thick MTD_{400}-b-$NORCOOH_{50}$ samples were subjected to treatments in each of the electroless cobalt and electroless nickel baths described in **Tables 2.5** and **2.6**. In the same manner as the previous section, these bulk films were lightly pre-loaded with Pd catalyst prior to submersion in the respective plating solutions. Plating rates of the electroless bath were kept low by keeping the concentration of the reduction (DMAB) minimal in an attempt to enhance the extent of deposition in the sub-surface microdomains.

Table 2.5: Electroless cobalt plating bath[21]
(Bath pH adjusted to 5.0 by adding sulfuric acid)

1. Cobalt (II) sulfate heptahydrate	25 g/L
2. Sodium succinate hexahydrate	25 g/L
3. Sodium sulfate (anhydrous)	15 g/L
4. Dimethylamine borane (DMAB)	1 g/L

After approximately 70 hrs of treatment in the respective electroless baths, samples were microtomed for TEM investigations. The cobalt-plated sample, **Figures 2.11A**, exhibited evidence of selective cobalt deposition as dark contrast near the film's free surface. Similarly to the electroless copper deposits described in the previous section, the growth of cobalt deposits

appears to have thickened the NORCOOH domains beyond the original 4-nm thickness. The observed maximum depth of cobalt growth into the bulk from the film's free surface was approximately 2 μm (**Figure 2.11B**).

Table 2.6: Electroless nickel plating bath[22]
(Bath pH adjusted to 6.0 by adding ammonium hydroxide)

1. Nickel (II) sulfate hexahydrate	40 g/L
2. Sodium citrate dihydrate	20 g/L
3. Lactic acid	10 g/L
4. Dimethylamine borane (DMAB)	1 g/L

The nickel-plated samples also exhibited some evidence of selective deposition in the block copolymer template, **Figure 2.12**. The depth of electroless nickel growth into the bulk of the film appears still less extensive than exhibited by the cobalt-plated samples. Once again the reduction of pre-loaded Pd^{2+} ions to Pd^0, and the associated formation of Pd nanoclusters, is visible in the NORCOOH microdomains away from the free surface (see also **Figure 2.3**). We note that macroscopic depositions of cobalt and nickel on the samples' surfaces, which resulted in shiny, metallic appearance (not seen in **Figures 2.11 & 2.12**) are magnetically polarizable - i.e., they exhibit attraction to permanent magnets. Cobalt, nickel, and their alloys are known to be ferromagnets.

In general, the amounts of cobalt and nickel depositions within the sub-surface NORCOOH microdomains achieved in these initial trials were smaller than in the previous (optimized) copper-plated samples. Preliminary loading tests (described in section 2.3.1) produced the block copolymer films that were essentially colorless, indicating that the transports of the plating reagents into the NORCOOH microdomains from the electroless cobalt and nickel baths

employed in these initial plating trials are unfavorable. Nevertheless, we have demonstrated, as a proof of concept, that our approach is not limited only to the selective plating of copper. With further optimization - e.g., via adjustment of the plating condition or changing bath formulation - improvements in the extent of sub-surface selective deposition of cobalt and nickel may be achievable. Finally, we expect that such an approach would be applicable to deposition of other electroless metals as well.

2.5 Casting oriented parallel lamellae in thin films of MTD_{400}-block-$NORCOOH_{50}$

As mentioned in section 2.3.1, within several microns of our bulk block copolymer film's free surfaces the microphase-separated lamellae generally align themselves parallel to the plane of the surfaces. This oriented lamellae served as templates for the construction of layered copper structure alternating with layers of insulating MTD lamellae (section 2.3.2). Such layered structure led to our speculation on a potential anisotropy in the electrical conductivity with respect to the lamellar orientation. In order to probe the electrical directionality of such layered copper-polymer structure, near-perfect parallel lamellae needed to be constructed.

We believe that the observed parallel orientation of the lamellae near the film's surfaces was induced by preferential interfacial interactions that led to segregation of the block components to the interfaces (i.e., NORCOOH to the hydrophilic glass substrate.) Surface segregation of block copolymer microdomains leading to parallel orientation of block lamellae near the interfaces has been previously reported.[23-25] However, due to kinetic limitations, the long-range propagation of such surface-induced parallel orientation into the bulk is practically not possible.

Therefore, we realized that a near-perfect parallel orientation of our block copolymer lamellae could potentially be captured via solution casting of very thin films. A very slow rate of solvent

evaporation would also be necessary to promote a well-defined, semi-long-range ordering of the microphase-separated structure in our block copolymer.[26] In our previous trials, casting thin films from small volumes of the block copolymer solutions directly in air - i.e., rapid solvent evaporation - led to morphologies that were not well defined.

The substrates employed in our initial trials were 36-μm-thick PET sheets (Melinex® polyester films 142-gauge, no pretreatment/coatings, donated by DuPont). These substrates were chosen because they do not swell upon exposure to the casting solvents (THF and toluene) and because they can be microtomed simultaneously with the block copolymer thin films deposited onto them (for cross-section TEM.)

Our first attempt to minimize the evaporation rate of the casting solvent was to cast thin films in a solvent-saturated atmosphere. As shown in **Scheme 2.2**, a piece of (flat) PET substrate was placed inside a THF-saturated sealed container (with a THF reservoir in bottom of container). A small amount of the block copolymer solution (3 mg/mL THF) was deposited onto the substrate without overflowing the film via a needle puncturing through a septum at the top of the lid (done so to minimize the release of THF from the container atmosphere.) The solution was left to dry over 20 hrs before the sample was removed from the THF atmosphere.

The resulting morphology, **Figure 2.13A**, revealed by staining the NORCOOH microdomains with gaseous dimethylcadmium, exhibits some degree of microphase separation. (Staining was carried out by placing microtomed samples above liquid $CdMe_2$ in a sealed container for 10hrs under a nitrogen atmosphere, followed by vacuum drying.) However, the microdomains appear somewhat fragmented, and no grains of oriented lamellae were found (in contrast to the bulk

film's morphology which was cast over 3 days, shown in **Figure 2.1**.) There was no evidence of surface-induced parallel lamellae at either film's surfaces. This indicated that the THF evaporation rate was still too high.

The same thin film sample was also loaded aqueously with $Na_2(PdCl_4)$ prior to microtoming. The resulting morphology, **Figure 2.13B**, is consistent with one obtained via gaseous $CdMe_2$ staining (**Figure 2.13A**). However, the aqueous staining imparts a more uniform contrast to the NORCOOH microdomains, while the 'spotty' staining of $CdMe_2$ is likely due to formation of nanoclusters of cadmium compounds (possibly oxides or hydroxides) upon exposure to air. This comparison represents our general experience that aqueous staining is preferable to gaseous $CdMe_2$ staining as a method to impart unambiguous contrast to water-permeable, carboxyl-containing microdomains of block copolymers. The rest of the samples presented in this section were stained with aqueous $Na_2(PdCl_4)$ solution.

We attempted to reduce the rate of solvent evaporation of our casting method further by diluting the casting solution (1.5 mg/mL) and using larger volume (~600 μL) of casting solution. In order to hold larger volume of solution on the substrate, we constructed temporary 'cups' from the flat PET sheet. This was done by raising the edges of a square PET sheet while the center of sheet (base of the 'cup', area ~1.5 cm^2) was held down to a flat glass slide via a 2-sided tape. The sides of the cup were then held upright by a tube-fastening clip. The cup setup was then placed in a THF-saturated container, and solution was again deposited into the boat via a needle. The solution was left to dry over 1-2 days. Such an effort to slow down the casting solvent evaporation rate further improved the thin film's morphology. **Figure 2.14** illustrates the microphase separated lamellar structure that appears better defined than the previous attempt.

Figure 2.14 also illustrates some degree of parallel orientation of lamellae at the interface with the PET substrate.

Our next attempt to attain a parallel orientation involved plasma treatment of the PET substrates. This approach was suggested by the fact that that bulk film used in our electroless deposition experiments, and which exhibits parallel lamellae near the free surfaces, was cast in a glass petri dish – a more hydrophilic substrate. Thus, we expected that an improvement in parallel orientation might be achievable by rendering the PET surfaces more hydrophilic as well. To do so, the PET films were subjected to an air plasma treatment (2 minutes at 100W using a Harrick Scientific PDC-32G air plasma cleaner.) As a result, the measured advancing water contact angle value decreased from 78° (before treatment) to 30°, indicating that the treatment successfully rendered the PET surfaces more hydrophilic.

The result of film casting on the plasma-treated PET substrate (via a PET 'cup' in the THF-saturated atmosphere, **Figure 2.15**) shows some additional improvement in the general ordering of the lamellar microdomains, and the individual grains (comprising oriented lamellae) appeared more prominent than in the previous trials. In the region adjacent to the plasma-treated PET substrate (right-hand edge) some parallel block copolymer lamellae are visible.[27] This morphology appeared to be the best result thus far in our attempts to attain surface-induced parallel lamellae in our MTD_{400}-$NORCOOH_{50}$ block copolymer thin films.

To further reduce the rate of solvent evaporation, we also attempted casting block copolymer thin films from a solution of mixed solvents: half-toluene and half-THF by volume (toluene being less volatile than THF.) This effort failed, however, as the addition of toluene to the THF solution

affects the microphase-separation process of the diblock copolymer; the final morphology was an ill-defined one that does not resemble the original sheet-like lamellae seen in films cast from THF.

We also realized that annealing block copolymers above their glass transition temperatures is another means to induce rearrangement of their microphase-separated morphologies. Such approach to achieve equilibrium morphology could lead to the surface-induced parallel lamellar orientation.[23-25] However, our block copolymer possesses very high glass transition temperatures: the MTD block's T_g ~210°C, and the NORCOOH block's T_g is speculated to be even higher. Still, we attempted annealing a bulk film sample of the block copolymer at 230°C under vacuum for 5 hrs. As a result, the film turned to a brown color and curled up, indicating some degree of oxidation and degradation. TEM observation of the annealed sample, loaded with aqueous $Na_2(PdCl_4)$, revealed no visible rearrangement of the lamellar structure: on average the individual grains of oriented lamellae did not grow larger, nor did the region of parallel lamellae near the free surfaces. We did not proceed with more rigorous annealing procedures. (Such effort may require the use of ultra-high vacuum to prevent extensive oxidative degradation.)

For future attempts to obtain better surface-induced parallel lamellae, we recommend using a larger volume of more diluted casting solution and reducing the rate of THF evaporate further. Casting thinner films (below ~1μm) could also effectively enhance the desirable effects of surface-induced parallel alignment throughout the thickness of the films. The use of more hydrophilic substrates, i.e., stronger preferential interfacial interactions, may be helpful. However, a drawback we noticed from casting films on relatively hydrophilic substrates (e.g., glass and plasma-treated PET) was the frequent delamination of the block copolymer films from the substrates during the aqueous treatments. Another challenge involving the use of our

particular PET substrates was the difficulties obtaining uniform, flat microtomed sections as the PET sections often curled up and/or fragmented during microtoming.

2.6 Summary

We have produced novel nanocomposites consisting of layered metallic structures embedded within a hydrocarbon polymer matrix via electroless deposition processes. Our approach relies on the diffusion of the electroless copper plating reagents through the aqueously permeable microdomain network of a diblock copolymer. The same network also simultaneously serves as template for the spatially selective electroless metal deposition, which in turns presents some limitation to the transport of plating reagents through the bulk of the film. Nevertheless, our process represents an efficient technique to deposit dense metallic structures within the sub-surface morphology of a block copolymer. Finally, the extent of metal deposition can be controlled by variation of the deposition rate and/or time, as well as via the selection of the optimal plating bath components.

2.7 References

(1) Clay, R. T.; Cohen, R. E. *Supramolecular Science* **1998**, *5*, 41-48.

(2) Clay, R. T.; Cohen, R. E. *New Journal of Chemistry* **1998**, *22*, 745-748.

(3) Shipley, C. R. *Plating and Surface Finishing* **1984**, *71*, 92-99.

(4) Deckert, C. A. In *ASM Handbook*; ASM International: Materials Park, OH, 1990; Vol. 5.

(5) *Electroless Plating: Fundamentals and Applications*; Mallory, G. O.; Hajdu, J. B., Eds.; American Electroplaters and Surface Finishers Society: Orlando, FL, 1990.

(6) Wynschenk, J. *Plating and Surface Finishing* **1983**, *70*, 28-29.

(7) Jackson, R. L. *Journal of the Electrochemical Society* **1990**, *137*, 95-101.

(8) Vanderputten, A. M. T.; Debakker, J. W. G. *Journal of the Electrochemical Society* **1993**, *140*, 2229-2235.

(9) Cho, J. S. H.; Kang, H. K.; Wong, S. S.; Shachamdiamand, Y. *Mrs Bulletin* **1993**, *18*, 31-38.

(10) Brandow, S. L.; Chen, M. S.; Wang, T.; Dulcey, C. S.; Calvert, J. M.; Bohland, J. F.;

Calabrese, G. S.; Dressick, W. J. *Journal of the Electrochemical Society* **1997**, *144*, 3425-3434.
(11) Hidber, P. C.; Helbig, W.; Kim, E.; Whitesides, G. M. *Langmuir* **1996**, *12*, 1375-1380.
(12) Hidber, P. C.; Nealey, P. F.; Helbig, W.; Whitesides, G. M. *Langmuir* **1996**, *12*, 5209-5215.
(13) Boontongkong, Y.; Cohen, R. E.; Rubner, M. F. *Chemistry of Materials* **2000**, *12*, 1628-1633.
(14) Zehner, R. W.; Sita, L. R. *Langmuir* **1999**, *15*, 6139-6141.
(15) Hashimoto, T.; Tsutsumi, K.; Funaki, Y. *Langmuir* **1997**, *13*, 6869-6872.
(16) Clay, R. T.; Cohen, R. E. *Supramolecular Science* **1995**, *2*, 183-191.
(17) Goldie, W. *Plating and Surface Finishing* **1964**, *51*, 1069-1074.
(18) Clay, R. T.; Cohen, R. E. *Supramolecular Science* **1997**, *4*, 113-119.
(19) Jagannathan, R.; Krishnan, M. *IBM Journal of Research and Development* **1993**, *37*, 117-123.
(20) Swanson, H. E.; Tatge, E. *Standard x-ray diffraction powder patterns*; National Bureau of Standards: Washington, D.C., 1953; Vol. 1.
(21) Pearlstein, F.; Weightman, R. F. *Journal of the Electrochemical Society* **1974**, *121*, 1023-1028.
(22) Riedel, W. *Electroless nickel plating*; ASM International: Metals Park, OH, 1991.
(23) Coulon, G.; Russell, T. P.; Deline, V. R.; Green, P. F. *Macromolecules* **1989**, *22*, 2581-2589.
(24) Russell, T. P.; Coulon, G.; Deline, V. R.; Miller, D. C. *Macromolecules* **1989**, *22*, 4600-4606.
(25) Kellogg, G. J.; Walton, D. G.; Mayes, A. M.; Lambooy, P.; Russell, T. P.; Gallagher, P. D.; Satija, S. K. *Physical Review Letters* **1996**, *76*, 2503-2506.
(26) Kim, G.; Libera, M. *Macromolecules* **1998**, *31*, 2569-2577.
(27) Note that though the particular microtomed section of the block copolymer thin film shown in **Figure 2.15** was apparently detached from its PET substrate, the author believes that the free surface on the right-hand side, where the parallel lamellae reside, is the surface previously in contact with the PET substrate. This is based on the general appearance of this and other microtomed sections of our block copolymer thin films - some with adjacent PET sections still intact - collectively observed over several TEM sessions. Such delamination of the block copolymer thin film may be attributed to possible hydration of the interface between the NORCOOH lamellar layer and the adjacent the plasma-treated PET surface during the aqueous loading treatments.

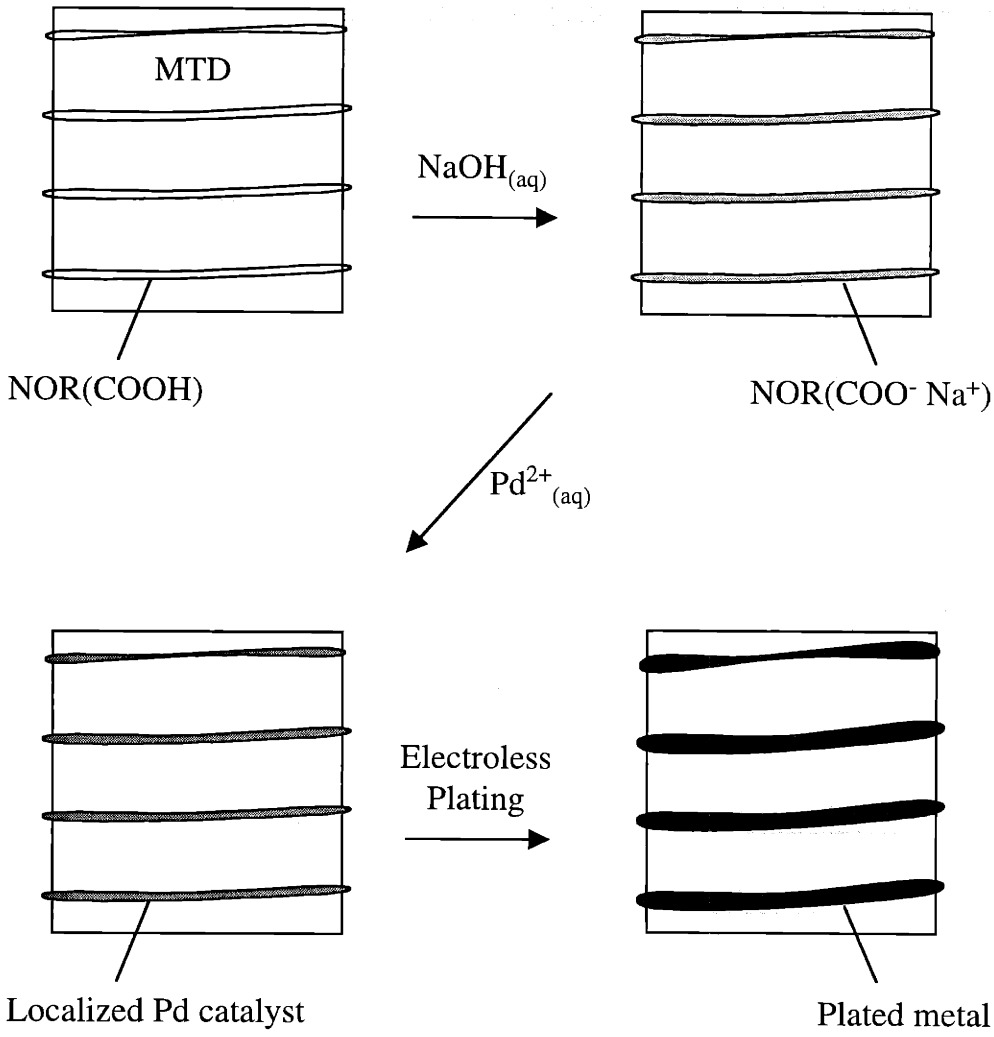

Scheme 2.1: Selective electroless metal deposition process

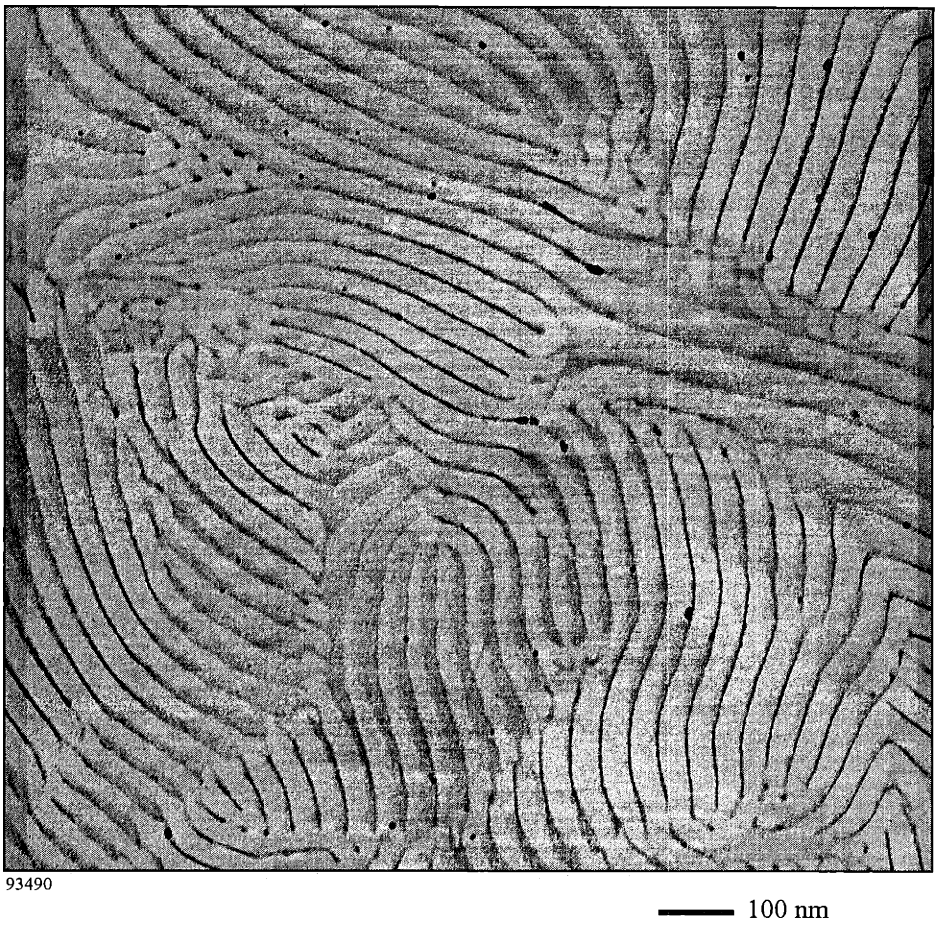

Figure 2.1A: Bulk morphology of poly($MTD_{400}NORCOOH_{50}$) film cast from THF; film loaded with $Na_2(PdCl_4)_{aq}$

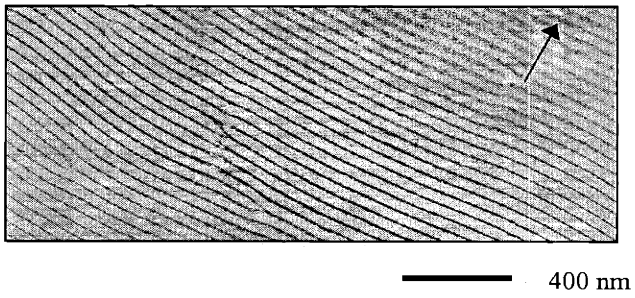

Figure 2.1B: Morphology near film's free surface (arrow indicates direction towards free surface.)

(A)

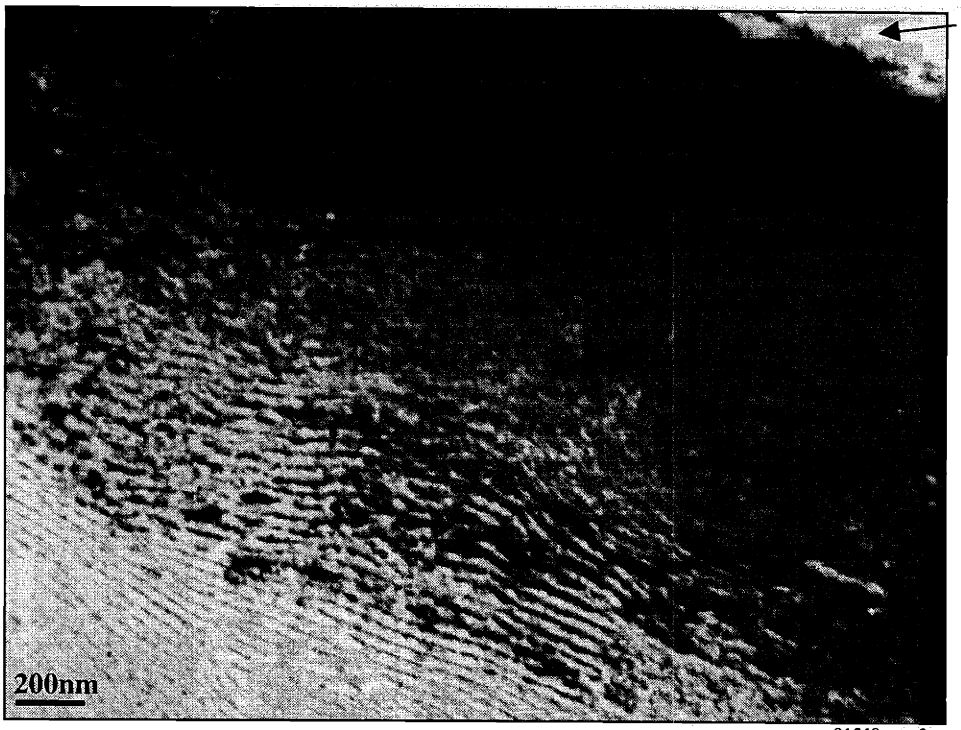

(B)

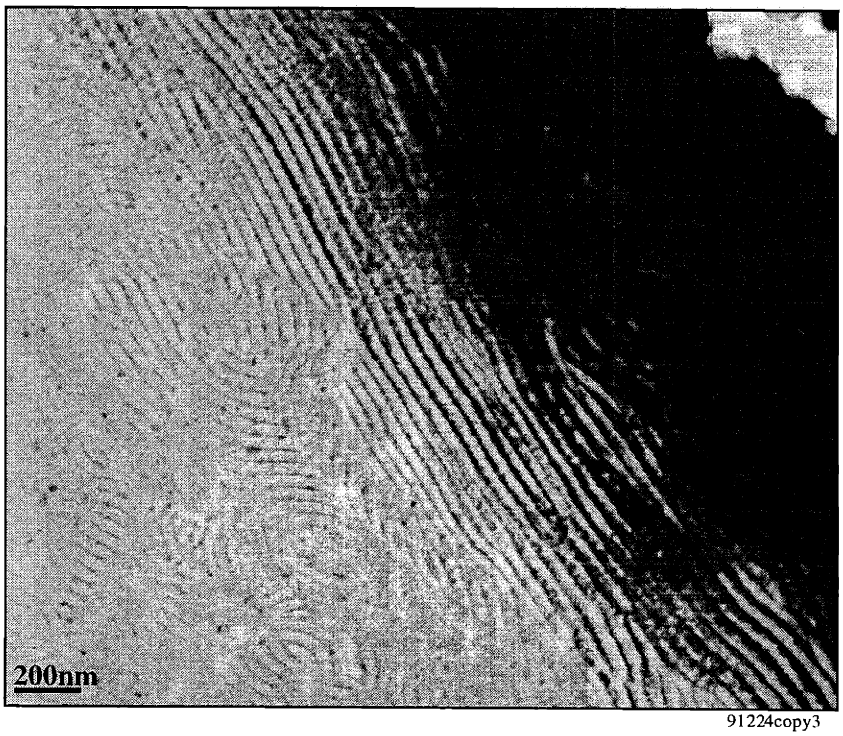

Figure 2.2 (A,B): Selective electroless copper deposition in NORCOOH microdomains via treatment in electroless copper bath **Formula I**

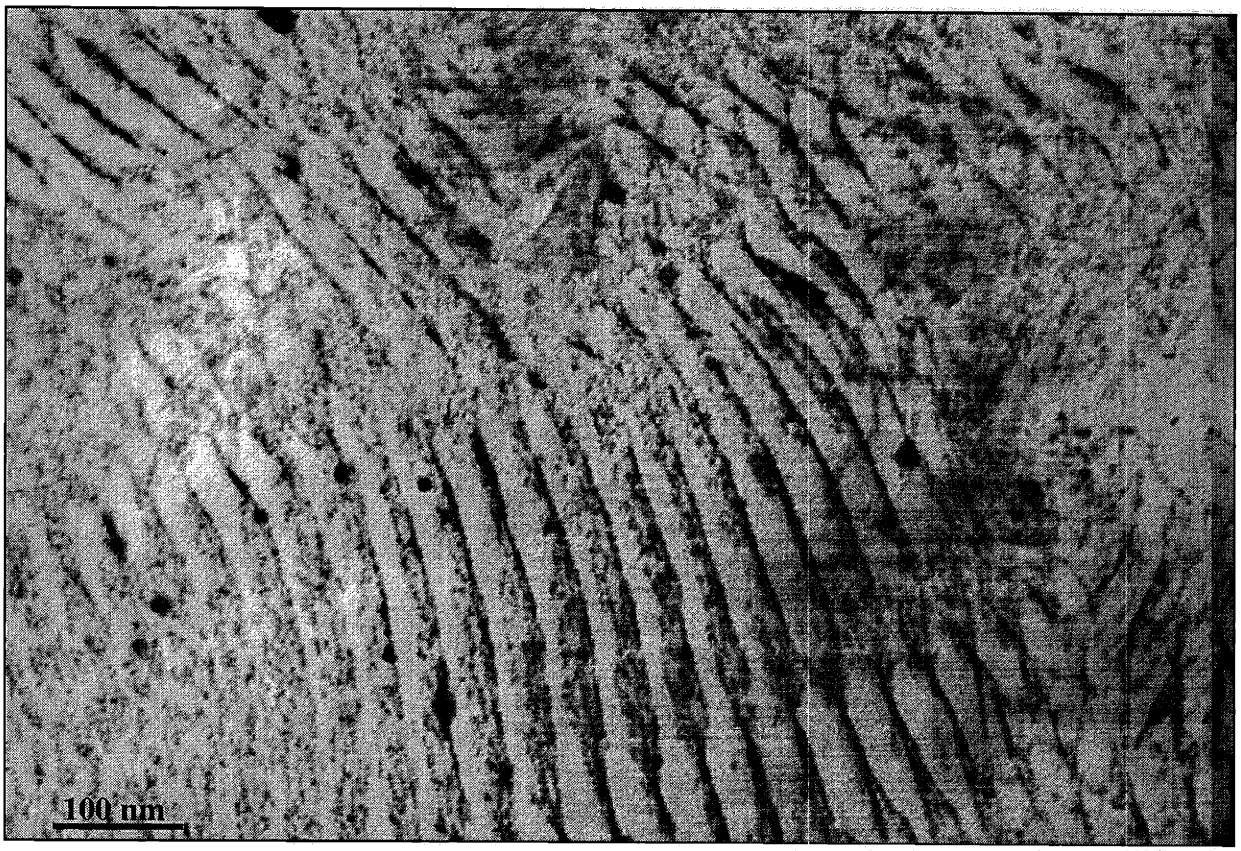

Figure 2.3: Reduction of pre-loaded Pd^{2+} ions and formation of Pd^{0} nanoclusters upon treatment in the electroless copper bath

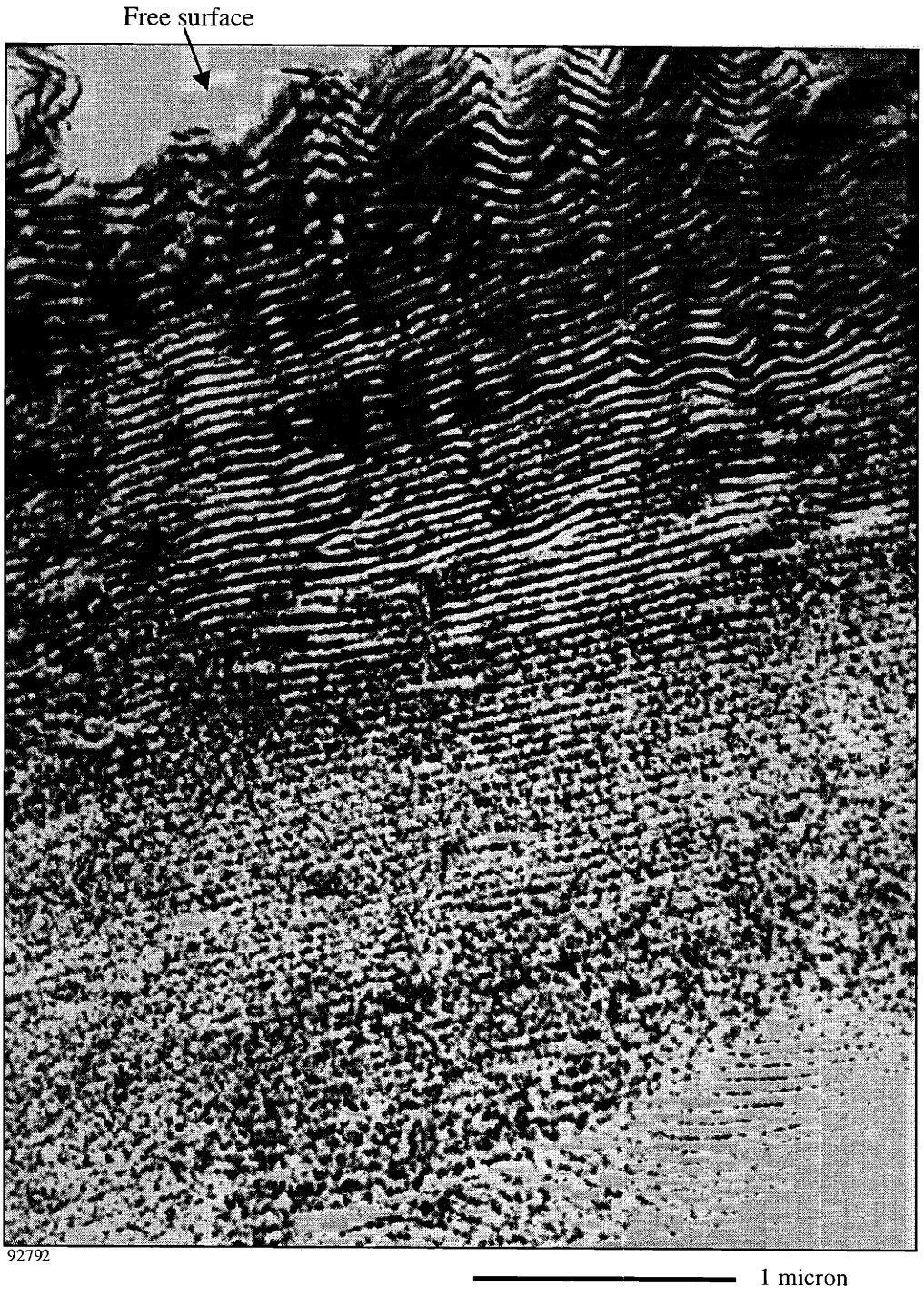

Figure 2.4: Selective electroless copper deposition via treatment in 'slow-plating' **Formula II** electroless copper bath for 16 hours

Figure 2.5: Scanning transmission electron micrographs (STEM) of sample treated in 'slow-plating' Formula II electroless copper bath for 16 hours

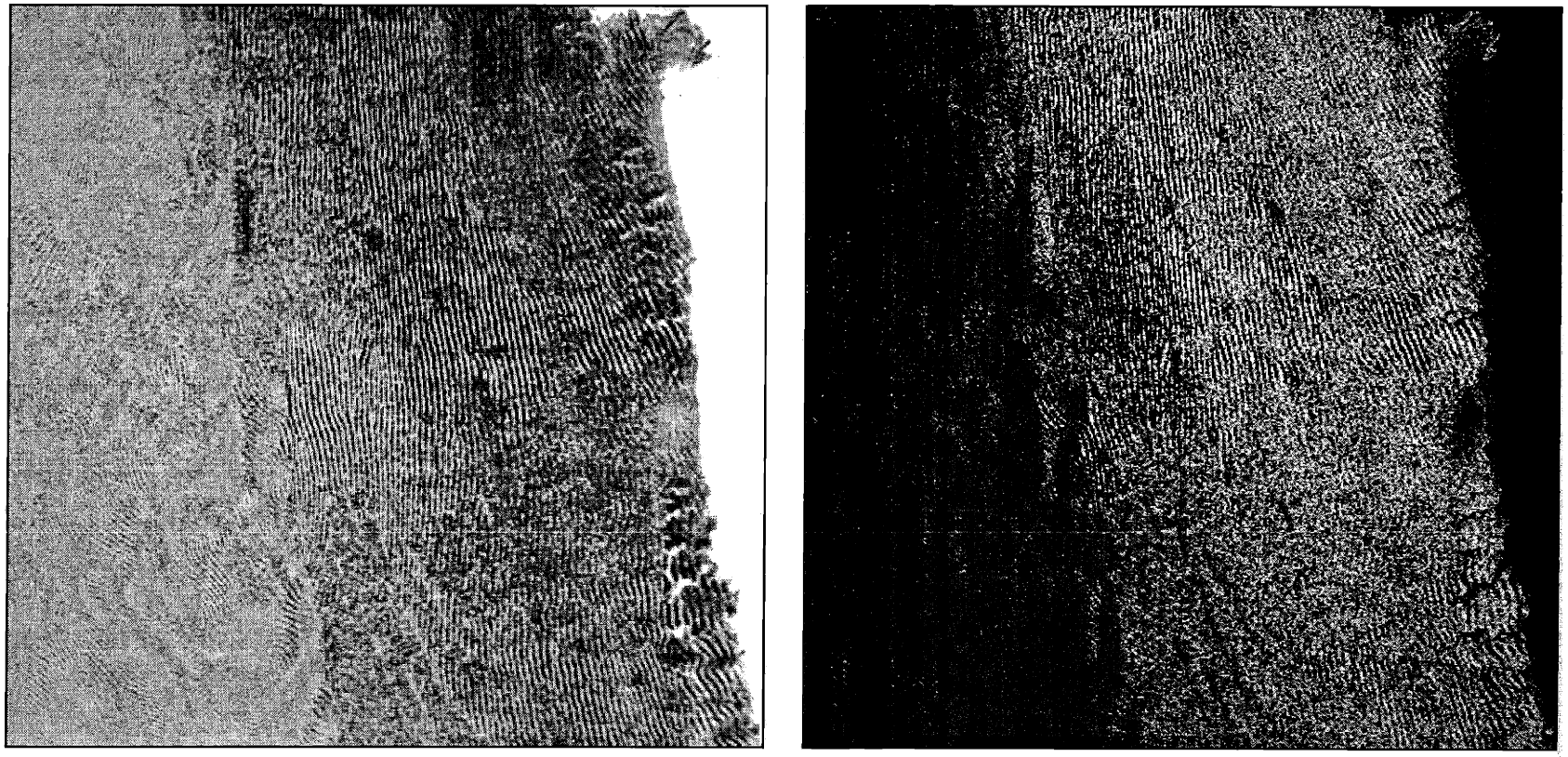

1 micron

(A) Bright-field image

(B) Associated copper map

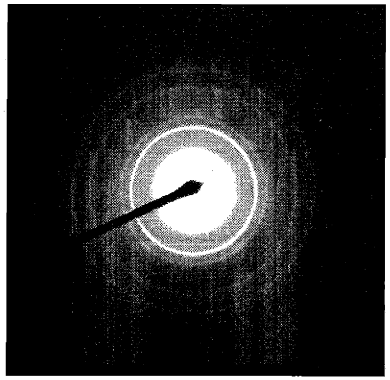

Figure 2.6:
Selected-area electron diffraction pattern of the copper deposit

Figure 2.7: Film treated in 'slow-plating' electroless copper bath for 16 hours

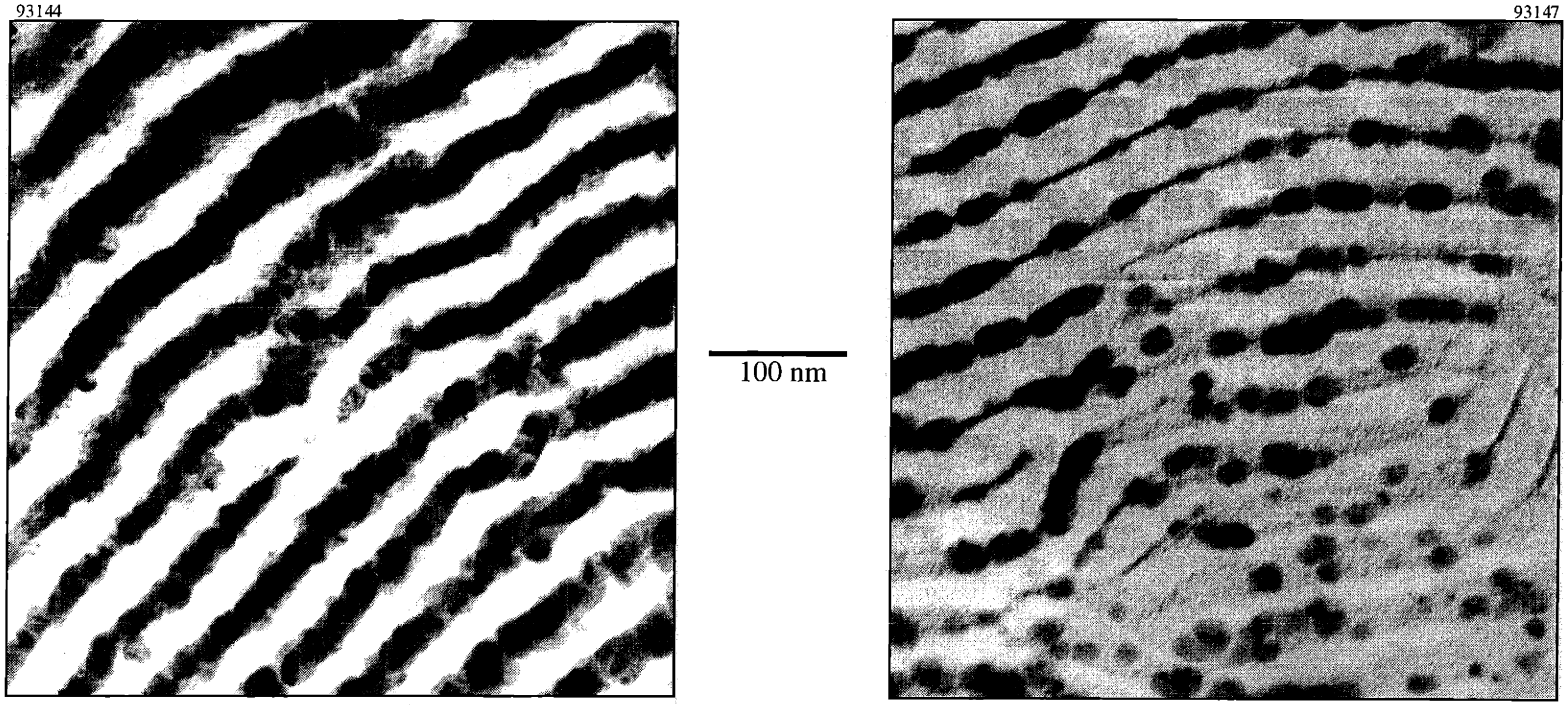

(A) Region adjacent to the film's free surface

(B) Region approximately 3.5μm away from the free surface

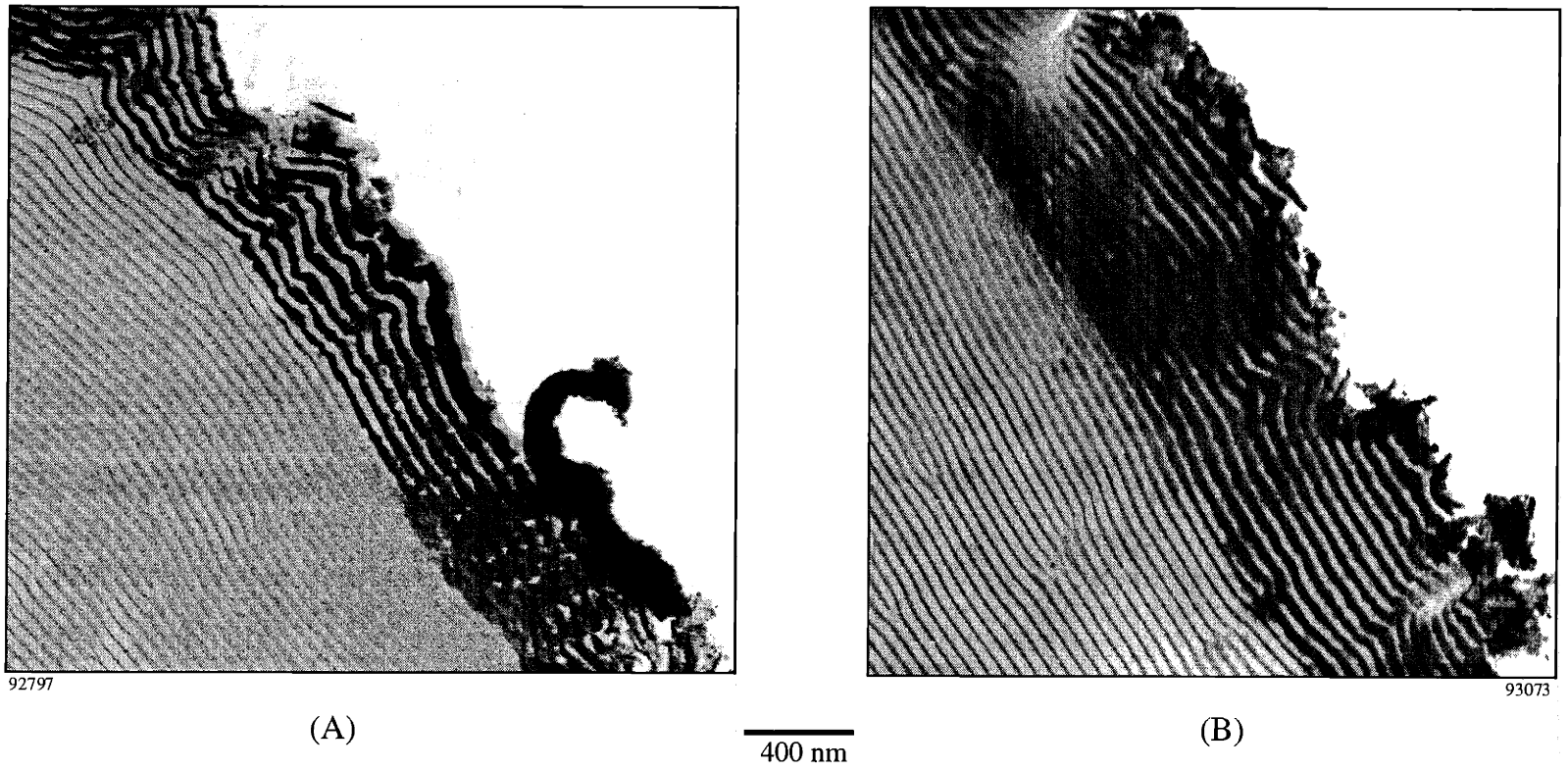

Figure 2.8: Films treated in 'fast-plating' electroless copper bath for
(A) 1.8 hours
(B) 16 hours

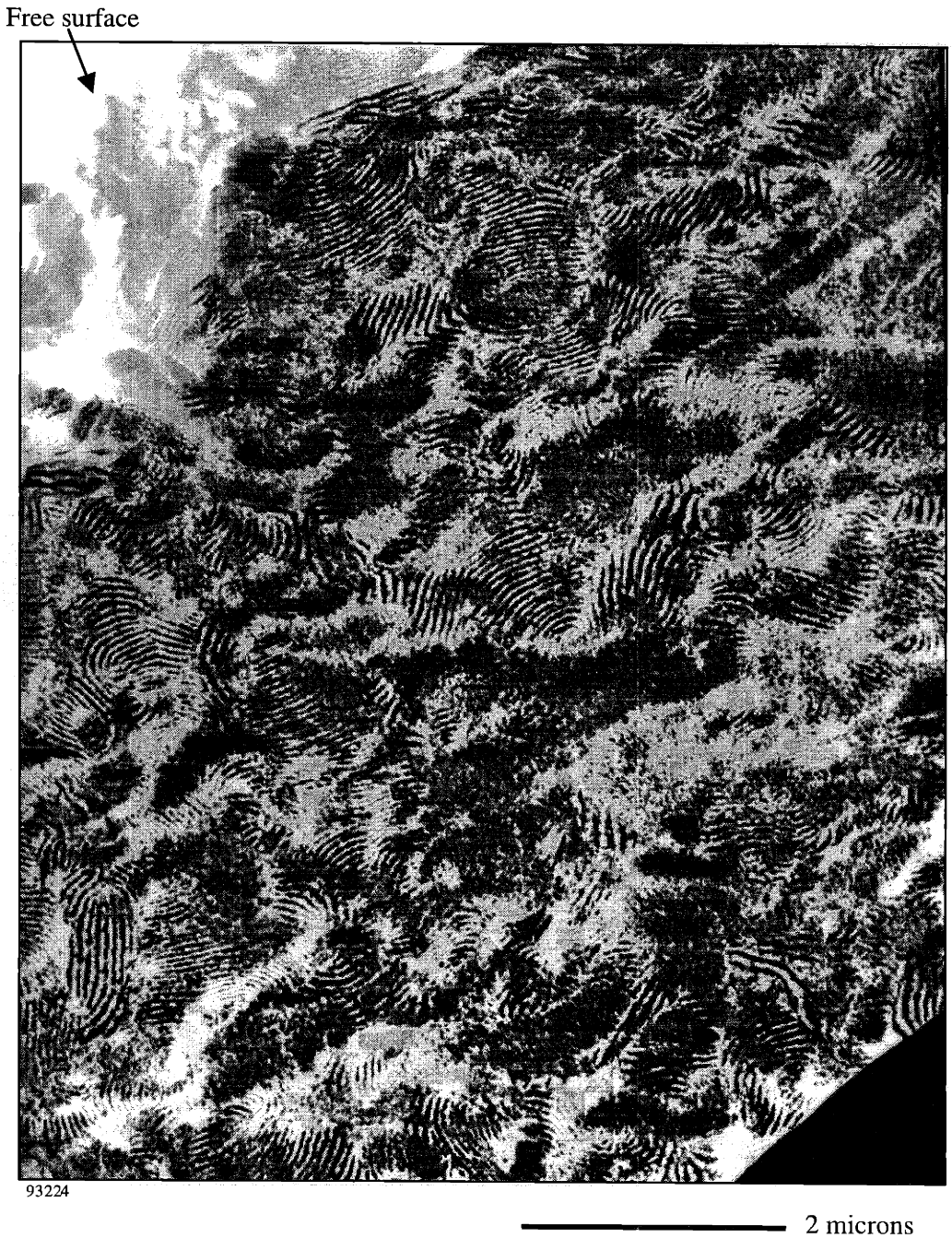

Figure 2.9: Film treated in 'slow-plating' electroless copper bath for 41 hours (Note: lamellae are arranged in randomly oriented grains)

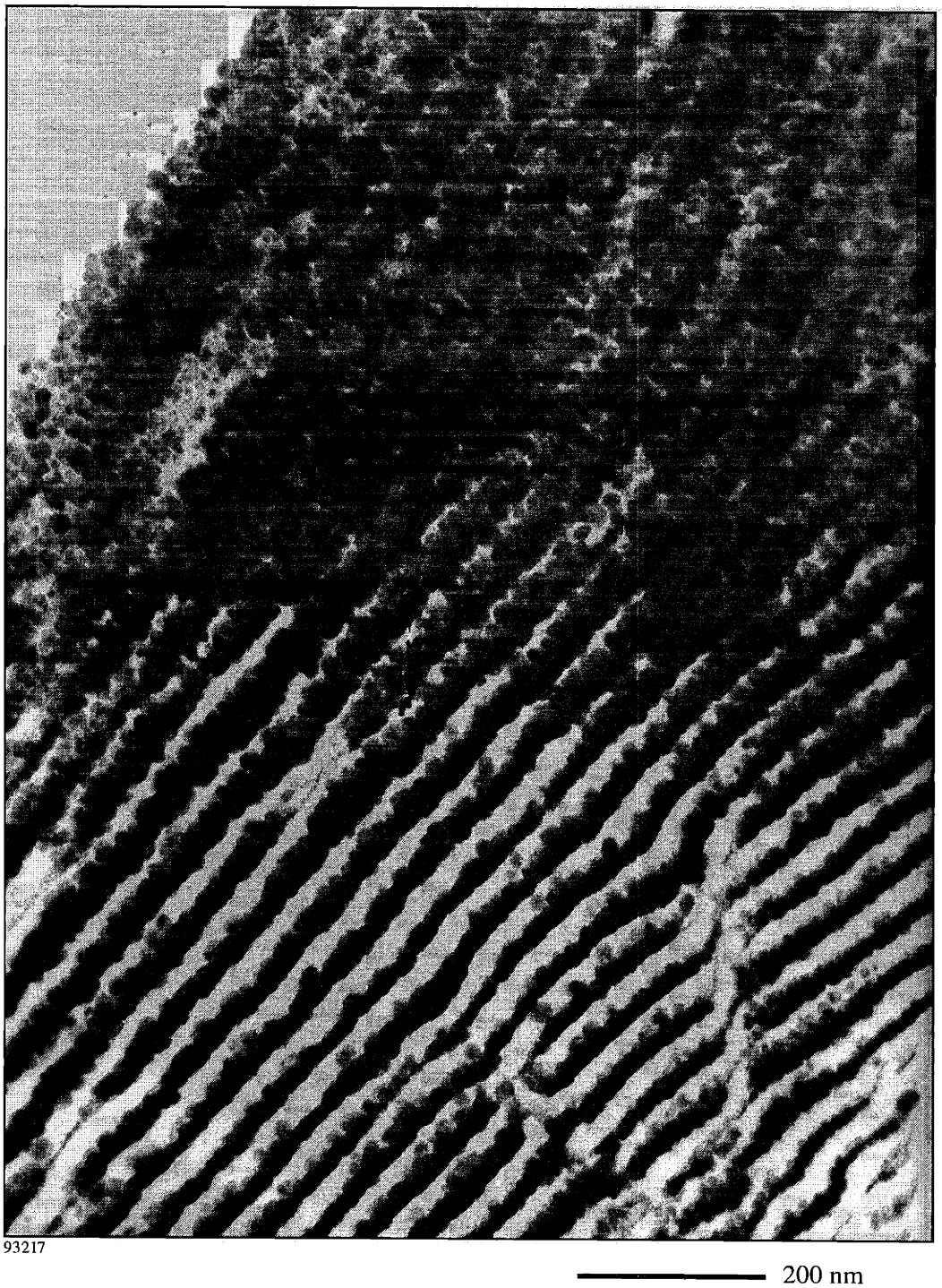

Figure 2.10: View through the thin dimensions of individual lamellar copper structure (Note: defect at center of image resulted from damage to the negative)

(A)

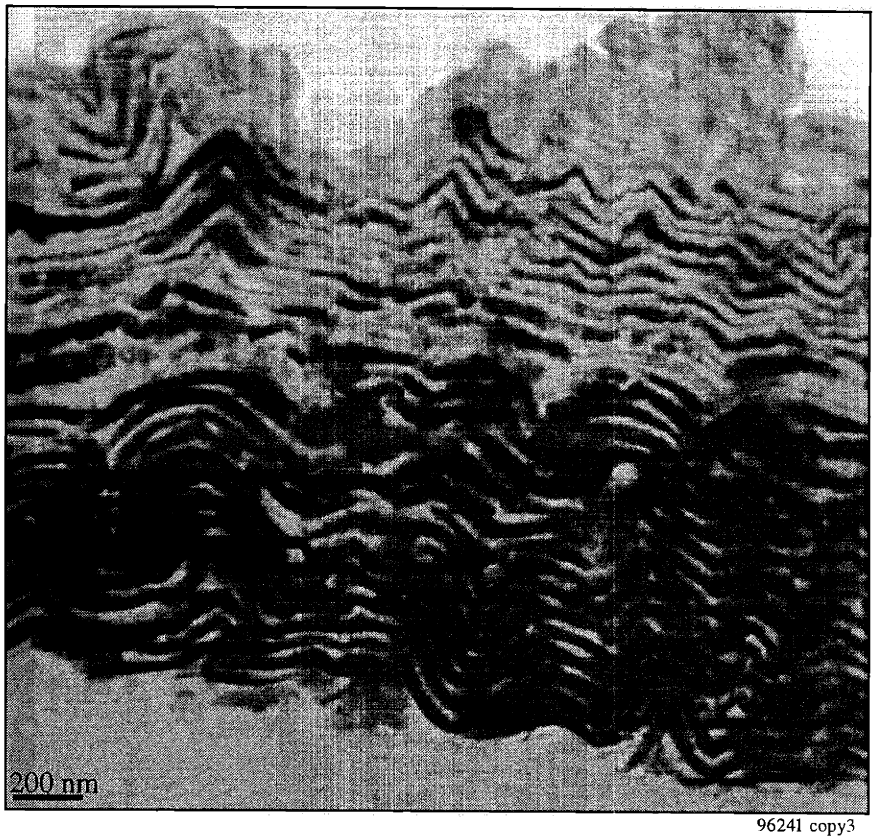

(B)

Figure 2.11 (A,B): Selective electroless **cobalt** deposition

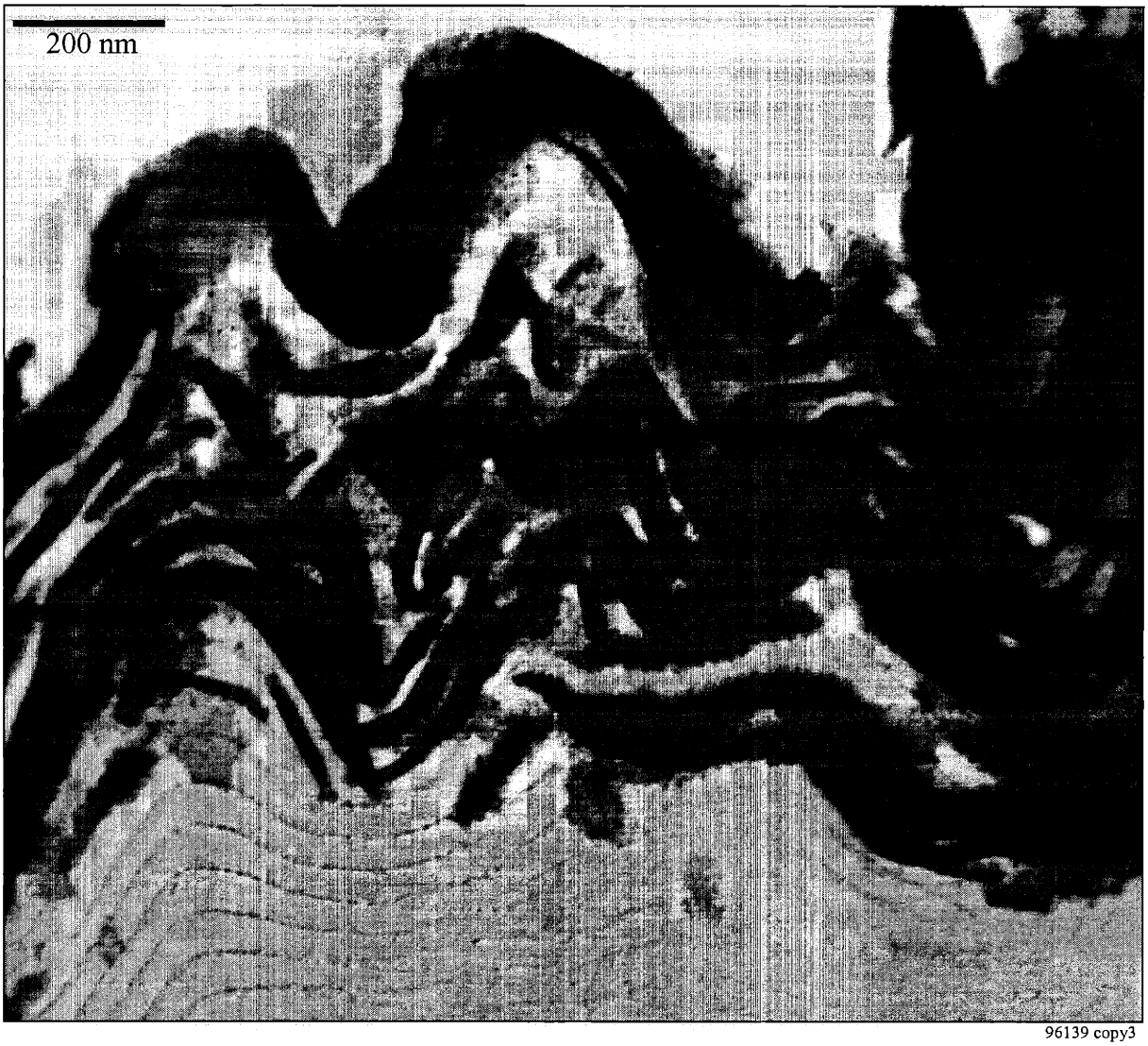

Figure 2.12: Selective electroless **nickel** deposition

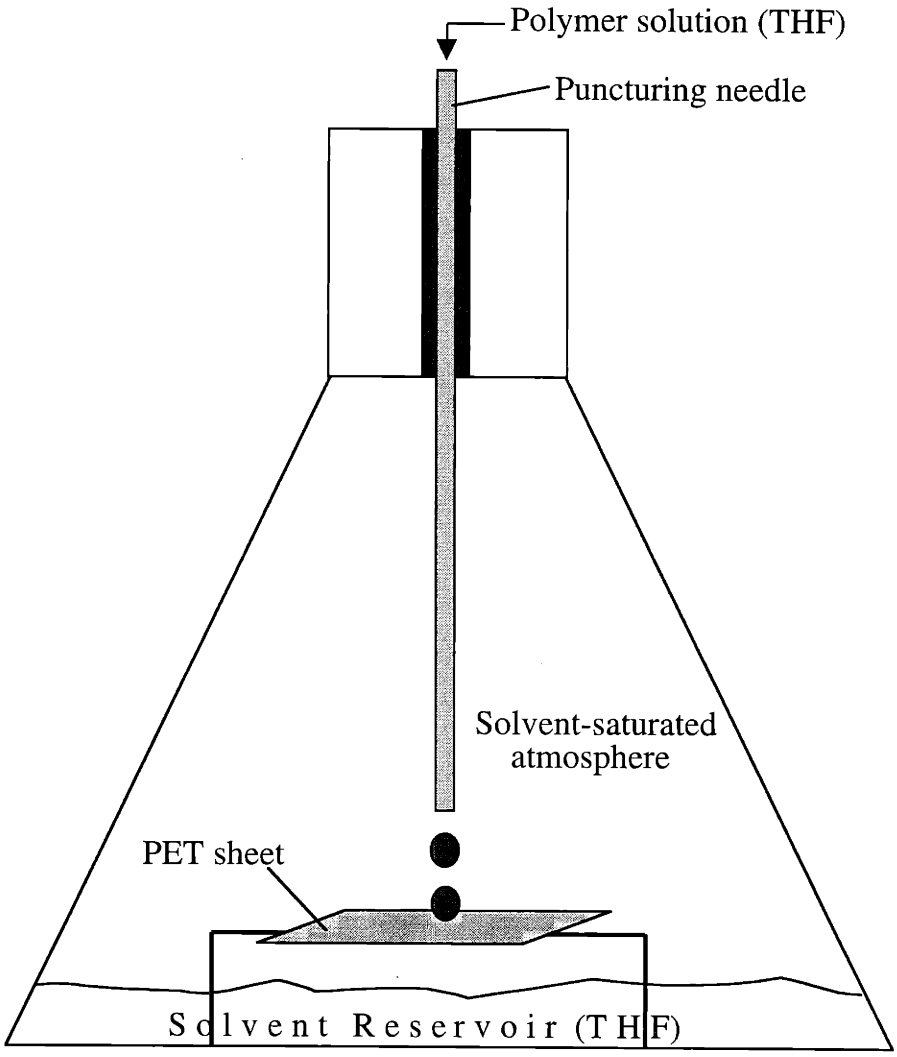

Scheme 2.2: Thin film casting at reduced solvent evaporation rate

(A)

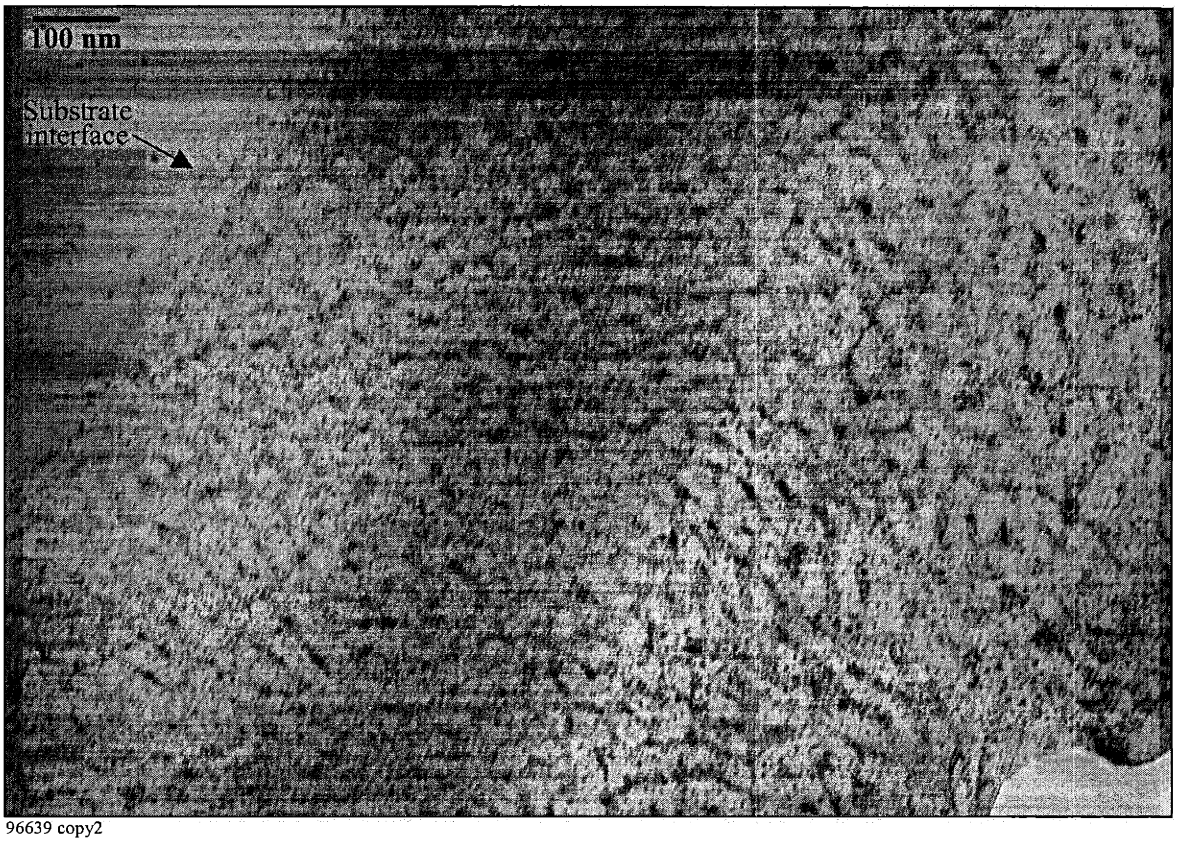

96639 copy2

97099 copy2

(B)

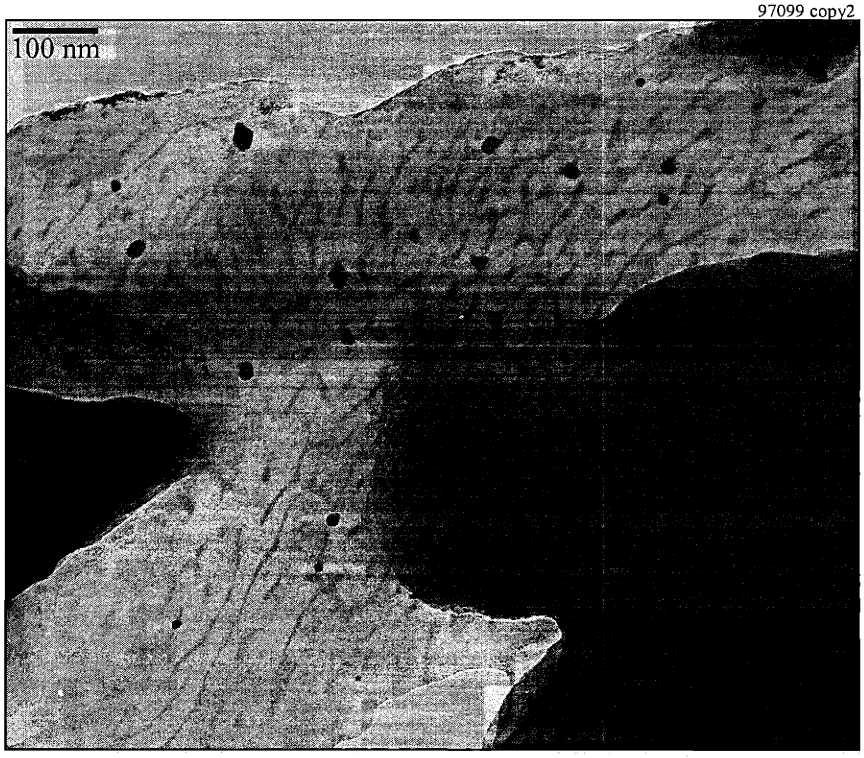

Figure 2.13: Thin film of poly($MTD_{400}NORCOOH_{50}$) cast at reduced solvent evaporation rate, stained with: (A) $CdMe_{2(g)}$ (B) $Na_2(PdCl_4)_{aq}$

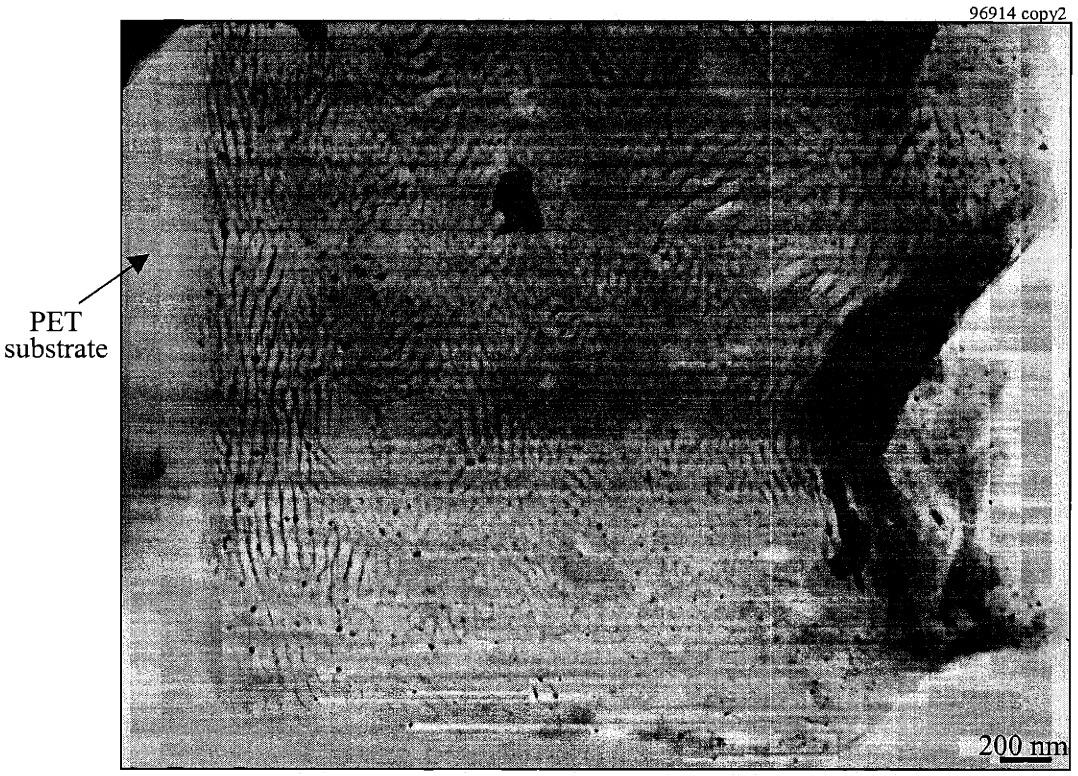

Figure 2.14: Thin film of poly($MTD_{400}NORCOOH_{50}$) cast at reduced solvent evaporation rate via PET 'cup'

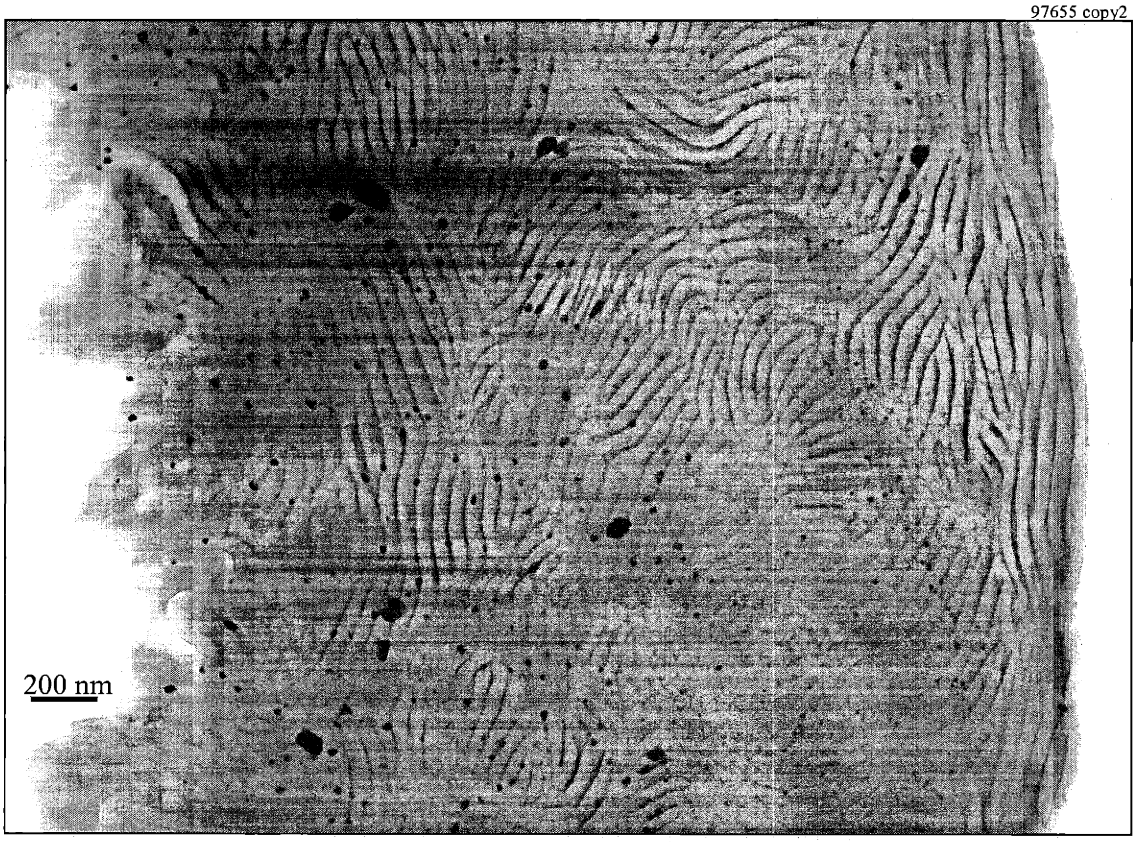

Figure 2.15: Thin film of $MTD_{400}NORCOOH_{50}$ cast onto plasma-treated PET substrate

Chapter 3
Cavitated Block Copolymer Micellar Thin Films: Laterally Ordered Arrays of Open Nanoreactors

3.1 Introduction

Amphiphilic block copolymer molecules, similar to low-molecular weight surfactants, aggregate to form micelles in selective solvents above a certain critical micelle concentration (CMC). In particular, diblock copolymers are known to assemble into spherical reverse micelles in organic solvents, with the insoluble polar blocks collapsing together to form the core and the soluble non-polar blocks forming the corona which extends into the solvent environment.[1-3] Such spherical aggregates are generally very monodispersed in size; it is commonly believed that they are formed via closed association of a fixed number of macromolecules per micelle.

At the next level of self-organization, micelles assemble to form highly ordered structures owing to superior size uniformity and high kinetic stability of the individual micellar building blocks. Of relevance to this current report is the laterally ordered hexagonal arrays of deposited micelles formed upon casting spherical micelles onto flat solid substrate, which has been the subject of recent investigations by several research groups.[4-6] Since the dimensions of block copolymer micelles fall in the approximate 10-100nm range, the self-assembly of micelles into ordered patterns is of interest in terms of potential applications in nanotechnology. For example, the polar cores of laterally ordered micelles have been employed as templates in which 2D arrays of inorganic nanoclusters can be created.[7,8]

The preceding chapters of this document illustrate aqueous-based approaches to synthesizing in-situ inorganic nanoclusters within carboxylic acid-functionalized microdomains of microphase-

separated bulk block copolymers. The initial objective of our current investigation was to apply similar aqueous approaches to create 2D arrays of nanoscale inorganics using thin film templates of in-plane microphase-separated, carboxyl-containing block copolymers. Laterally microphase-separated block copolymer thin films have been achieved via a number of elegant methods.[9-14] However, these methods often rely on stringent control over certain parameters: film thickness, relative interfacial energies among block components and surfaces, commensurability, external fields, and the ability to produce nanopatterned substrates, for example. In comparison, the direct casting of kinetically stable micelles from selective solvents onto solid substrates represents a facile means to obtain laterally ordered block copolymer microdomains for use as 2D templates.

As such, we employed laterally ordered micellar thin films formed via direct casting of a styrene(PS)-acrylic acid(PAA) diblock copolymer reverse micelles from a toluene solution, in which the carboxyl-functionalized cores could serve as the nanoreactors. In addition to the successful use of PAA micelle cores as in-situ templates, we also report a notable structural transformation of the micellar thin films which occurs upon cavitation[15] of the individual deposited micelles. Such process takes place during the aqueous treatment employed to selectively load metal ions (nanocluster precursors) into the PAA microdomains, and leads to the creation of unique 2D hexagonal arrays of nanoscale surface cavities. We demonstrate that the cavitation of the individual micelle is a result of swelling of PAA micelle cores and rupture of PS shells during the treatment of micellar thin films in aqueous solution of NaOH – the first step of the 2-step metal loading technique.[16] Finally, the use of these cavitated, metal-loaded PAA domains as open nanoreactors is presented.

3.2 Experimental

Materials

Polystyrene-block-acrylic acid (PS-b-PAA) (M_n 16,400-block-4,500, with a 1.05 polydispersity) from Polymer Source, Inc. was used as received. The following chemicals were also used as received: sodium hydroxide (98.9%) obtained from Mallinckrodt; calcium hydroxide (95+%), lead (II) acetate trihydrate, silver (I) acetate, cadmium (II) acetate dihydrate (98%), and tetraaminepalladium chloride from Aldrich; copper (II) acetate monohydrate (98+%) from Strem. All aqueous solutions were made with deionized water.

The silicon nitride membrane-substrates were purchased from Structure Probe, Inc. Each TEM-grid-sized substrate (diagonal width 3mm) consists of a 100nm-thick amorphous, low-stress Si_3N_4 membrane supported on top of a 0.2mm-thick silicon wafer that has been back-etched in the center to create a see-through square window of size 0.46mm. All substrates were rinsed with toluene prior to film casting.

Sample preparation

The block copolymer was mixed with toluene (HPLC grade, not anhydrous) at a 2.5mg/mL concentration, resulting in a slightly cloudy, slightly viscous mixture. Heating the mixture to ~140°C yields an optically clear solution which remains clear when allowed to cool back to room temperature. Each thin film sample was produced by spin-casting: first covering the substrate with a small amount of the (room-temperature) polymer solution, followed immediately by spinning the substrates at 1,600 rpm for 1 minute. Residual toluene was removed from samples under vacuum.

The 2-step metal loading treatment (**Scheme 1.1B**) involves submerging samples first in a 0.04M $NaOH_{aq}$ solution for 16-24 hours, followed by a 1-minute rinse in deionized water. Samples are

then treated in their respective metal salt solutions (0.4mM $PbAc_2$, 0.02M $CdAc_2$, 0.04M $CuAc_2$, 5mM AgAc, and 5mM $Pd(NH_3)_4Cl_2$, where Ac = CH_3COO) for 20-40 hours, followed by a 2-4-minute rinse.

H_2S gas was generated for use in PbS nanocluster synthesis by adding ~4 drops of bis(trimethylsilyl) sulfide (Aldrich) into ~15mL of water. The $H_2S_{(g)}$ source vial and samples were then placed together in a closed jar for 30 hours at room temperature. Afterwards, residual $H_2S_{(g)}$ was removed from samples under vacuum.

Microscopy (CMSE)

Transmission electron microscopy (TEM) was performed on a Jeol 200CX operating at 200 kV. Scanning transmission electron microscopy (STEM) was performed on a VG-HB603 operating at 250 kV. Atomic force microscopy (AFM) was performed on a Digital Instruments Dimension 3000 Nanoscope IIIA scanning probe microscope operating in Tapping® mode using a silicon cantilever (nominal specified tip radius of 5-10nm). Scanning electron microscopy (SEM) was performed on a Jeol 6320FV field-emission high-resolution microscope operating at 2 kV.

3.3 Characterization of the cavitated micellar thin films

Each thin film sample was prepared by spin-casting the solution of PS-b-PAA diblock copolymer (Mw 16.4k-b-4.5k, equivalent to 158 and 62 repeat units for PS and PAA blocks, respectively) onto a 100-nm-thick silicon nitride membrane supported on a silicon substrate, back etched to create a window. The amorphous 'TEM-transparent' silicon nitride membrane is featureless; thus, it allows for direct plan-view TEM observation through the thin film deposited on it without the need for potentially damaging flotation/transfer procedures. Researchers have successfully used silicon nitride membranes as substrates for matching TEM-AFM studies of block copolymer thin films.[17]

To load metals into the PAA domains of the thin films, we followed the 2-step ion exchange protocol described in Chapter 1. The technique yields selective loading of metal ions in the carboxyl-containing domains of block copolymers. The first step ($NaOH_{aq}$ treatment) neutralizes the COOH groups in the acid-functionalized domains to $COO^- Na^+$. The subsequent uptake of desired metal ions is facilitated[16] as the heavier metal ions replace the Na^+ ions, which bind relatively weakly to the COO^- groups. The loaded metal also effectively provides contrast for TEM observations.

The casting solution's concentration of 2.5 mg/mL PS-b-PAA in toluene is significantly above the critical micelle concentration generally observed for amphiphilic block copolymers in selective solvents (for example, a CMC of 0.065 mg/mL for PS-b-P2VP in toluene[18] has been reported.) Therefore, formation of reverse micelles is expected. Initially, the mixture at room temperature was visibly cloudy and more viscous than pure toluene. This mixture was spin-cast onto silicon nitride substrates and loaded with $PbAc_2$ ('Ac' = acetate = CH_3COO) via the aqueous loading technique mentioned above. **Figure 3.1A** is a plan-view (bright-field) TEM image of such a film. It features cylindrical micelles in which the PAA cores, stained with Pb, appear dark.

Heating the cloudy mixture (in a sealed vial) transforms the elongated micelles into ones of lower aspect ratios. **Figure 3.1B** is a TEM image of a film cast after heating the mixture at 108°C for 20 minutes (film casting is done after the solution has cooled back to room temperature.) The elongated micelles observed before heating have been 'broken up' into mostly elliptical aggregates. Further increase in the temperature of the heating cycle yields increasing fraction of spherical aggregates. Heating above ~140°C produces visibly transparent solutions with a

consistency similar to that of toluene; casting from such solutions yields only spherical aggregates.

Figure 3.2 shows a representative top-down morphology of thin films cast (at room temperature) after heating the solution at ~150°C for 20 minutes. The film comprises a quasi-regular array of circular features (sized 10-15nm) which represent the Pb-stained PAA domains (cores) of the micellar aggregates. The spacing between adjacent stained PAA cores is approximately 33nm. A 2D Fourier transformation of the highlighted area in **Figure 3.2** yields a pattern of six-fold symmetry, reflecting the hexagonal packing of the PAA domains. This thin film morphology is the focus of this current investigation.

In **Figure 3.3**, a bright-field TEM image of a Pb-loaded sample (**A**), is shown next to its associated Pb elemental map (**B**) generated via scanning transmission electron microscopy (STEM, energy-disperse X-ray analysis) wherein Pb appears bright. (Note that resolution in STEM mapping is lower than in bright-field mode.) The obvious correlation between the 2 images confirms that the dark staining of PAA domains seen in bright-field mode is in fact due to the loaded Pb. In a similar fashion, we have successfully loaded the hexagonal PAA array with several other metal species, including Cu, Cd, Ag, and Pd. **Figures 3.4 & 3.5** show PS-b-PAA thin film samples loaded with $CdAc_{2(aq)}$ and $CuAc_{2(aq)}$, respectively. (Note that Cd and Cu loadings impart relatively faint TEM contrast to the thin film morphology as these elements are lighter than Pb.)

A key morphological feature repeatedly observed in these metal-loaded samples (**Figures 3.2-3.5**) is the fact that metal staining occurs around the perimeter of the roughly spherical PAA domains,

but is absent from the domain centers. Such features raised questions regarding the structure of the PAA domains in the thin films. In another indicative observation illustrated in **Figure 3.5**, part of the thin film stained with $CuAc_{2(aq)}$ appears to have peeled off the silicon nitride substrate and folded over the other part of the same film still attached to the substrate. Within the overlapped region (right side), brightest illumination (i.e., maximum transmitted electron) occurs where the Cu-loaded PAA domains in the folded (top) film layer superimpose those in the substrate-bound layer underneath (examples are indicated with arrows.) By comparison, lower brightness is observed where the PAA domains of the top film overlap the matrix of the film underneath, and vice versa. This contrast effect suggests the existence of voids in the centers of these stained PAA domains.

Topographical survey of the metal-loaded films via atomic force microscopy (AFM) reveals that their surfaces comprise hexagonal arrays of localized depression (to be referred to as 'cavities' or 'holes' in this report), as shown in **Figure 3.6** for a sample loaded with $CdAc_{2(aq)}$. The length scale and the arrangement of the cavities correlate very well with the features of metal-loaded PAA domains (with unstained centers) observed via plan-view TEM. The existence of a hole in the individual PAA core is therefore responsible for the absence of metal loading from the center of the PAA microdomains. The formation mechanism of this structure will be addressed below.

Figure 3.7A is a higher-magnification AFM image of the Cd-loaded thin film. The associated 2D profile indicates cavity depth of at least 7nm – likely an underestimated value since the diameter of the AFM probe is comparable to the size of the PAA domains. (Probes with smaller diameter such as carbon nanotubes may provide a more accurate depth measurement.) Analysis of AFM profiles near edges of deposited thin films similar to one shown in **Figure 3.7B** yields an average deposited film thickness of ~22nm. Similar surface topography has also been observed in

samples loaded with other metals. **Figure 3.8 & 3.9** represent the AFM profiles of Cu- and Pb-loaded thin films, respectively.

In an attempt to examine the cross-sectional structure of the cavitated micellar films, a high-resolution scanning electron microscope (SEM) was employed. Thin films on silicon nitride membranes (supported on silicon wafers) were cleaved, positioned edge-up, and coated with a thin layer (~2nm) of sputtered gold. **Figure 3.10A** shows a cross-sectional SEM profile (secondary electron mode) of a sample previously loaded with palladium after NaOH treatment. Bright-contrast features present in the micellar thin film layer (top layer), likely representing the array of cavitated PAA domains, are of length scales comparable to those observed via AFM and TEM.[19] (Notice that the 100-nm layer of silicon nitride membrane supporting the micellar thin film is distinguishable from the silicon substrate underneath it.) **Figure 3.10B** illustrates a region of overlapping spherical features within the deposited film, which is consistent with the double-layer micelle deposition seen via TEM (refer to discussion on multi-layered micelles in section 3.5, **Figures 3.17**). Due to limitations on the image resolution and the available sampling area, we were unable to reliably determine the depth of the cavitated holes via SEM observations.

3.4 Cavitation[15] of the deposited micelles

It is important to note that the hexagonal arrays of cavities observed in metal-loaded thin films do not occur upon film casting, nor due to sample degradation on exposure to electron beam (in TEM), but rather during the aqueous metal loading process described earlier. AFM height image of a representative block copolymer thin film before any aqueous treatment, **Figure 3.11A**, shows that the 'as-cast' sample consists of protruding spherical features rather than cavities. The as-cast film topography reflects the structure of deposited reverse micelles,[4,5] where PS block forms the corona and PAA block the core. Similar to the metal-loaded PAA domains seen via TEM and

AFM, these as-cast spherical micelles also assemble into hexagonal arrays, with the same center-to-center spacing (~33nm).

As mentioned earlier, the casting of amphiphilic block copolymers from selective solvents, and the subsequent formation of laterally ordered hexagonal arrays of spherical micelles, has already been reported.[4-6] The observed close-packing of the deposited micelles may be attributed to capillary forces between these colloidal particles during solvent evaporation.[20,21] In addition, it has been shown that upon film casting, toluene-swollen (PS) corona/shells of adjacent micelles fuse together to form a continuous film matrix, while the cores of the individual micellar aggregates maintain their integrity.[6] In our system, such film formation process is evident from the observation (peeling/folding of the thin film) of **Figure 3.5**.

Direct adsorption of whole block copolymer micelles from organic solvents onto solid substrates[22] is made possible by the kinetic stability of the micellar aggregates. Relatively slow dissociation and exchange kinetics of aggregated block copolymer molecules in selective solvents[5,23] enables direct transfer of micellar structures into dry films during rapid casting processes (**Scheme 3.1**). This solvent-free structure is not the thermodynamically stable morphology for our diblock copolymers thin films. Annealing the micellar films above the glass transitions of both blocks (170°C for 2 days under vacuum) yielded a morphology of in-plane cylinders of PAA embedded in PS matrix. We note that THF-cast freestanding films of the block copolymer revealed a bulk morphology containing hexagonal PAA cylinders in PS matrix.

As mentioned above, the transformation of the film structure, from that of as-cast micelle array to the array of cavities, takes place during the aqueous NaOH treatment (first step of the 2-step metal

loading process – **Scheme 1.1B**). **Figure 3.11B** shows the topography of a micellar film after treatment in 0.04M $NaOH_{aq}$ solution (26 hrs). The hexagonal arrangement and spacing between the NaOH-induced cavities match those of the as-cast spherical micelles (**Figure 3.11A**). Therefore, we concluded that the holes are created at the centers of the individual micelles. We attribute the observed structural transformation primarily to the strong tendency of PAA to swell in the presence of base and the fact that each PAA domain is confined by a thin shell of glassy polystyrene.

To consider the swelling of PAA core, we refer to the swelling behavior of carboxyl-containing polymer latex particles in alkaline solutions.[24-27] Upon exposure to a basic medium, carboxylic acid groups, incorporated into latex particles to stabilize them against flocculation, become negatively charged. This neutralization leads to the hydration and the associated volume increase due to water uptake as the particles become increasingly hydrophilic. Wiese and Rupaner[24] observed 'alkali swelling' of poly(n-butyl acrylate) latex containing 15wt% methacrylic acid monomer above pH 8. A maximum volume increase by a factor of 30 exhibited by the swollen particles occurs at pH 10.2.

In other instances, subsequent removal of water from swollen latex leads to the formation of microvoid(s) inside the particles.[25,26] (Hollow latex particles have been employed as components to impart opacity to paints.) The degree of alkali swelling is known to increase with the amount of carboxylic acid groups incorporated into the latex.[27] Additional factors that influence alkali swelling include the glass transition temperature and hydrophilicity of the latex polymer, which determine the latex's ability to accommodate volume expansion (i.e., chain mobility in aqueous environment). For example, swelling of carboxyl-containing polystyrene latexes is negligible[27]

due to the glassy and hydrophobic nature of PS. However, alkali swelling of carboxyl-containing PS latex can be achieved above the T_g of the polymer.[26]

We believe that significant swelling of the PAA domains upon NaOH treatment (pH 12.6), employed in this work to facilitate metal loading, occurs in a manner similar to the swelling of carboxyl-containing latex. The fact that the PAA micelle core consists essentially of pure carboxylic acid groups provides a strong driving force for the hydration of the PAA core upon neutralization of PAA carboxyl groups; thus, substantial swelling can be expected. The volume expansion of the PAA domains leads to the rupture of the PS corona towards the film's free surface as indicated by **Scheme 3.2**. As the PAA cores become neutralized by the base, increasing amounts of water permeate into the core. Corresponding rise of pressure in the core eventually results in the fracture of the hydrophobic styrene top (corona) layer since any elastic deformation of the PS shell to accommodate the core's volume expansion is very limited. (Our hypothesis relies on successful diffusion of aqueous reagents through the top PS corona layer. This appears to be justified based on our observations of metal loading without NaOH treatment, discussed later.)

Alkali swelling of latex particles is observed with several hydroxide bases of monovalent cations,[24,26] for example LiOH, NaOH, KOH, and NH_4OH. However, the swelling of particles is strongly dependent on the valency of the base's counter-cation. In contrast to monovalent bases, the use of divalent $Ca(OH)_2$ produces no swelling effect; the latex particles maintain their original sizes independent of the solution pH.[24] Such absence of swelling is attributed to ionic crosslinking of neutralized acid groups within the matrix of the latex by the divalent Ca^{2+} ions which effectively inhibits volume expansion.

We performed an analogous experiment by treating our as-cast micellar thin films in a 0.0156M (saturated) $Ca(OH)_{2(aq)}$ solution. AFM investigation of the samples, illustrated in **Figure 3.12A**, revealed a film topography with spherical micelles still intact (the micelle dimensions appear somewhat diminished, however,) while cavities are clearly absent. TEM observation of the sample, **Figure 3.12B**, confirms the successful loading of calcium from solution into the PAA domains. Thus, our results indicate that ionic crosslinking of PAA provided by the loaded Ca^{2+} ions successfully suppresses the swelling and subsequent cavitation of the PAA cores.

Wiese et al.[24] also reported that similar suppression of swelling due to ionic crosslinking could be achieved using other divalent cations (Zn^{2+} and Mg^{2+}). By the same token, we attempted additional loading experiments by treating samples directly in the aqueous loading solutions of $PbAc_2$ and $CdAc_2$ and bypassing the NaOH treatment (equivalent to **Scheme 1.1A**.) Similar to the results of $Ca(OH)_2$ treatment, we observed that swelling and cavitation of the micelles is again suppressed. AFM profile of a sample treated with $PbAc_2$, **Figure 3.13A**, exhibits spherical micelles resembling those of the as-cast sample. The corresponding TEM micrograph, **Figure 3.13B**, clearly shows that the selective sequestering of Pb into the PAA microdomains proceeded successfully. Essentially identical results (**Figure 3.14**) were obtained from direct sample treatment in a CdAc2(aq) solution, bypassing NaOH.

Metal ions loaded into these samples in the absence of prior NaOH treatment impart relatively uniform staining contrast (**Figures 3.12B, 3.13B, and 3.14B**) to the PAA domains, instead of the previously shown uneven (ring-like) staining characteristic of NaOH-treated, cavitated PAA cores (**Figures 3.2-3.5**). Such observation represents additional evidence for the absence of void formation in the cores in these closed micelles. We note that the successful loading of the divalent cations into the PAA core in the absence of cavitation implies that aqueous reagents are

indeed able to permeate through the PS shell into the core of the closed micelle. It is our speculation that the diffusion of aqueous reagents, including NaOH, through the hydrophobic styrene-rich corona is possible (within our experimental timeframe) because the top PS corona layer that covers the PAA cores is very thin (most likely less than 10nm since the film thickness is only ~22nm.)

To further investigate the surfaces of the micellar thin films, water contact angle experiments were performed. Silicon wafers with a 150-nm-thick deposited silicon nitride surface layer were used as templates in place of the TEM-transparent silicon nitride membrane substrates since the TEM-grid sized membrane substrates are too small to obtain accurate contact angle measurements from. (Sample preparations were performed in the same way as described earlier, and identical AFM results were obtained using these larger substrates.) **Table 3.1** summarizes the results from advancing water contact angle measurements on the respective sample surfaces. The as-cast sample prior to any aqueous treatment (film surface represented by **Figure 3.11A**) exhibits an average contact angle of 66°. In comparison, cavitation of the deposited micelles upon NaOH treatment renders the film surface (represented by **Figure 3.11B**) more hydrophilic, as indicated by a decrease in the water contact angle value to 52°. (A much larger drop in water contact angle is not expected since polystyrene still constitutes a large portion of the thin film's surface in spite of the observed cavitation.)

Table 3.1: Comparative water contact angle measurements

Surface	Water contact angle (Advancing, average)	Stand. Dev.
1. As-cast PS-b-PAA micellar thin film	66.5°	3.3°
2. Micellar film treated in 0.04M $NaOH_{aq}$ (cavitated micelles)	52.4°	2.3°
3. Micellar film treated in 0.0156M $Ca(OH)_{2(aq)}$	63.0°	3.0°
4. PS sheet (neat)	83.7°	2.6°
5. PS sheet treated in 0.04M $NaOH_{aq}$	88.0°	2.0°
6. Silicon nitride substrate	40.1°	2.5°
7. Glass slide	18.1°	0.8°

A separate test revealed that the surface of bulk polystyrene does not exhibit reduction in water contact angle when subjected to the same NaOH treatment. Therefore, the observed decrease in contact angle as a result of treating the micellar thin films in NaOH may be directly attributed to the cavitation of the PAA cores, rather than to a general increase in hydrophilicity of the surrounding PS matrix. This observation also suggests that PAA's carboxylic acid groups within these open micelles are accessible from the film's surface. As a further confirmation, relatively small change in surface hydrophilicity is observed after sample treatment in $Ca(OH)_{2aq}$: an average water contact angle of 63° reasonably reflects the expected absence of cavitation in these ionic-crosslinked (closed) micelle cores (represented by **Figure 3.12**.)

3.5 Micellar thin films as in-situ array templates

The selectivity of metal loading within the cavitated (open) micelles introduces a potential for utilizing these micellar thin films as templates for in situ synthesis of nanocluster arrays. We demonstrate this by loading a sample with silver (via $AgAc_{aq}$ solution, after $NaOH_{aq}$ treatment) followed by reduction in a hydrogen atmosphere (~2atm at 85C for 30 hrs). Successful reduction of the PAA-bound Ag^+ ions to Ag^0 -- evident by the absence of characteristic ring-like staining of the cavitated PAA domains imparted by loaded metal ions -- resulted in a hexagonal array of

silver clusters ~4nm in size within the thin film template as shown in **Figure 3.15**. The relatively uniform silver cluster size observed may be attributed to the inherent size monodispersity of the individual micelles and their PAA cores. The use of micelles as templates to achieve nanocluster size uniformity has been demonstrated in a number of block copolymer micellar systems.[7,8,28]

As an extension of the electroless metal deposition effort outlined in Chapter 2, we also employed the cavitated micellar thin films as templates for selective Ni plating. In similar manner to previous chapter, the PAA domains were first selectively loaded with Pd^{2+} ions via aqueous $Pd(NH_3)_4Cl_2$ solution, which served as catalyst for the subsequent electroless nickel deposition (see **Table 2.6** for bath composition). **Figure 3.16A** shows a strip of micellar thin film next to regions of the substrate without deposited micelles. **Figure 3.16B** shows a higher-magnification image of a larger film. These TEM images indicate that nickel plating occurred beyond the PAA domains, both on the surrounding PS matrix and on the substrate. Nevertheless, a definite selectivity of Ni plating within the cavitated PAA domains, evident from the especially dark TEM contrast of the hexagonal PAA domains, was already achieved in this preliminary attempt despite the relatively high Ni deposition rate used. We anticipate that an improvement in the deposition selectivity within the PAA domains could be achieved by optimizing the plating conditions, i.e., reducing the amount of pre-loaded Pd catalyst and lowering the Ni plating rate.

Thus far, we have discussed the morphology observed in relatively thin regions of the micellar films in which only single layers of micelles have been deposited. In most samples, however, spin casting yields variations in film thickness. An increase in thickness is generally accompanied by a transition in the observed plan-view morphology towards that of stacking multiple micelle layers. Shown via TEM in **Figure 3.17A** is the transition from a region of the familiar monolayer (upper-left corner) towards a bilayered region in which the 2 overlapping micelle layers assemble

out-of-register (center) and in-register (lower-right corner) with each other. (Refer to **Figure 3.10B** for cross-sectional SEM profile of bilayered deposited micelles.) A transition from a bilayer to triple-layered deposited micelles has also been observed in still thicker film regions.

Attempts to synthesize PbS nanoclusters within the micellar thin films were made by exposing samples loaded with Pb^{2+} ions to H_2S gas. However, we noticed during TEM observations that the some of the resulting nanoclusters became unstable upon contact with the electron beam, and appeared to 'evaporate' from the micellar film template.[29] **Figure 3.17B** depicts the same transition region of the originally Pb-loaded sample (as **Figure 3.17A**) after the sample has been exposed to H_2S and the electron beam (in TEM). Rearrangement of materials upon beam contact has effectively removed the nanoclusters from the cavitated PAA domains. The depletion of cluster materials from the micellar monolayer area (thinner region, upper-left) left behind mostly empty array of holes (bright contrast) in the polymer matrix. In the bilayered region (lower-right), the nanoclusters have been depleted from one of the overlapping micelle layers, while a hexagonal array of clusters remains in the other.

We attribute the depletion of the cluster material from the micellar templates to the fact that the individual micelle cores are open to the free surface. Therefore, in the bilayered region of **Figure 3.17B**, depletion of cluster materials was limited to the open nanoreactors of the top micelle layer. The cluster materials in the bottom micelle layer were stabilized against the electron beam by the coverage provided by top layer. Hence, the nanoclusters are retained in the 'covered' nanoreactors in the bottom micelle layer. We do not know the exact mechanism by which these nanoclusters become mobilized upon contact with the electron beam. Nevertheless, the above observation serves as an example of the unusual characteristics associated with our cavitated micellar thin films.

The transfer of the nanocluster material out of the micellar template led to the formation of larger aggregates on the film's surface, shown in **Figure 3.18**. We believe that these Pb-based surface objects (Pb contents of which have been verified via STEM elemental mapping) of various sizes and shapes (rod-like, elliptical, rhombic, etc) are crystals of PbS and its derivatives (e.g., $PbSO_4$).[30] Prominent features which signify such material rearrangement are the observed depletion zones surrounding the surface objects. These depletion zones, which exist throughout the surfaces of such samples, comprise arrays of empty cavities (previously loaded with Pb) and can be readily distinguished from the adjacent regions where the nanoclusters still remain in the micelles. This observation also illustrates the fact that such depletion of nanoclusters from cavitated micelle cores did not take place over the entire surface areas of those samples investigated.

To examine our hypothesis that such depletion occurs because the cavitated micelle cores are open to the free surface, we preformed a similar experiment using a sample of 'closed' micelles; i.e., as-cast sample loaded with $PbAc_{2(aq)}$, bypassing $NaOH_{aq}$ (film structure before H_2S exposure is represented by **Figure 3.13**.) TEM investigation of the sample revealed that the large majority of the resulting PbS nanoclusters are retained within the micellar templates (**Figure 3.19**), and very few depletion zones or surface objects characteristic to the cavitated micellar templates were observed. This implies that the coverage at the free surface provided by the intact top polystyrene shell effectively stabilizes the nanoclusters within the closed PAA cores.

3.6 Additional observations

We note that similar structural transformation of the as-deposited hexagonal micelles to that of cavitated micelles has been successfully reproduced on other more hydrophilic substrates

including glass and silicon wafer (with native oxides), shown in **Figures 3.20A & 3.20B**, respectively. (Note that several distinguishable spherical objects in **Figure 3.20B** may represent deposited spherical micelles that have not yet cavitated.) In addition, it has been reported that the adsorption of micelles leads to the same lateral ordering on both polar and non-polar solid substrates:[4,31] direct adsorption of whole micelles was observed on non-polar substrates, while polar surfaces were reportedly covered first with a monolayer brush of adsorbed free block copolymer chains, onto which the micelles subsequently adsorb. Thus, we anticipate the ability to generate such micellar thin films on a variety of other surfaces as well.

Finally, the author makes note of certain experimental difficulties encountered with the current micellar thin film system. They include the occasional delamination of the thin films from their substrates during the aqueous treatment steps. Also, spin-casting on silicon nitride membranes leads to film non-uniformity, both in terms of areal coverage (dewetting of the casting solution from the silicon nitride substrate) and in terms of thickness (variation in number of deposited micelle layers.) These practical challenges should be taken into consideration towards scale-up efforts that may be required for future applications of the system.

3.7 Summary

The deposition of styrene-acrylic acid block copolymer reverse micelles from toluene solution, and the formation of micellar thin films comprising laterally ordered arrays of PAA microdomains in the PS matrix, is demonstrated, along with successful use of such thin films as templates to synthesize corresponding arrays of inorganic nanoclusters. Upon exposure to the solution of a monovalent base, cavitation of the individual deposited micelles occurs due to hydration and swelling of the PAA cores, in analogy to swelling behavior of carboxyl-containing polymer latex particles in alkaline solution. The cavitation of the micelles transforms the as-cast film structure

into in-plane surface cavities that are also arranged in the same hexagonal arrays. These cavities connect the PAA domains, originally covered by PS (corona) layer, to the free surface. Thus, the cavitated PAA domains serve effectively as open nanoreactors for nanocluster synthesis as demonstrated. Finally, the process presented here represents a facile method to create patterned surfaces comprising nanoscale carboxyl-functionalized (i.e., chemically reactive) sites.

3.8 References

(1) Price, C. In *Developments in Block Copolymers*; Goodman, I., Ed.; Applied Science Publishers: London, 1982; Vol. 1; pp 39-80.

(2) Tuzar, Z.; Kratochvil, P. In *Surface and Colloid Science*; Matijevic, E., Ed.; Plenum Press: New York, 1993; Vol. 15; pp 1-83.

(3) Moffitt, M.; Khougaz, K.; Eisenberg, A. *Accounts of Chemical Research* **1996**, *29*, 95-102.

(4) Meiners, J. C.; Ritzi, A.; Rafailovich, M. H.; Sokolov, J.; Mlynek, J.; Krausch, G. *Applied Physics A-Materials Science & Processing* **1995**, *61*, 519-524.

(5) Spatz, J. P.; Sheiko, S.; Moller, M. *Macromolecules* **1996**, *29*, 3220-3226.

(6) Breulmann, M.; Forster, S.; Antonietti, M. *Macromolecular Chemistry and Physics* **2000**, *201*, 204-211.

(7) Spatz, J. P.; Roescher, A.; Moller, M. *Advanced Materials* **1996**, *8*, 337-340.

(8) Spatz, J. P.; Mossmer, S.; Hartmann, C.; Moller, M.; Herzog, T.; Krieger, M.; Boyen, H. G.; Ziemann, P.; Kabius, B. *Langmuir* **2000**, *16*, 407-415.

(9) Kellogg, G. J.; Walton, D. G.; Mayes, A. M.; Lambooy, P.; Russell, T. P.; Gallagher, P. D.; Satija, S. K. *Physical Review Letters* **1996**, *76*, 2503-2506.

(10) Fasolka, M. J.; Harris, D. J.; Mayes, A. M.; Yoon, M.; Mochrie, S. G. J. *Physical Review Letters* **1997**, *79*, 3018-3021.

(11) Huang, E.; Rockford, L.; Russell, T. P.; Hawker, C. J. *Nature* **1998**, *395*, 757-758.

(12) Rockford, L.; Liu, Y.; Mansky, P.; Russell, T. P.; Yoon, M.; Mochrie, S. G. J. *Physical Review Letters* **1999**, *82*, 2602-2605.

(13) Thurn-Albrecht, T.; DeRouchey, J.; Russell, T. P.; Jaeger, H. M. *Macromolecules* **2000**, *33*, 3250-3253.

(14) Peters, R. D.; Yang, X. M.; Kim, T. K.; Sohn, B. H.; Nealey, P. F. *Langmuir* **2000**, *16*, 4625.

(15) We note that the term 'cavitation' conventionally refers to the formation of local vapor-filled cavities in liquids induced by pressure reduction below a critical value, often as a result of rapid liquid motion (e.g., cavitation behind the blades of a ship propeller.)[32] Our use of the term 'cavitation' (as well as 'cavities') does not imply a meaningful correlation between this conventional engineering definition and the observations of our micellar thin film system.

(16) Clay, R. T.; Cohen, R. E. *Supramolecular Science* **1998**, *5*, 41-48.

(17) Morkved, T. L.; Lopes, W. A.; Hahm, J.; Sibener, S. J.; Jaeger, H. M. *Polymer* **1998**, *39*, 3871.

(18) Tassin, J. F.; Siemens, R. L.; Tang, W. T.; Hadziioannou, G.; Swalen, J. D.; Smith, B. A. *Journal of Physical Chemistry* **1989**, *93*, 2106-2111.

(19) We believe that the features of bright contrast in the SEM images represent the cavitated PAA domains. The unusually enhanced brightness may be attributed to an enhanced electron scattering as a result of selective Pd loading in PAA cores, and to an increased electron emission at the edges of such small cavities.

(20) Kralchevsky, P. A.; Nagayama, K. *Langmuir* **1994**, *10*, 23-36.

(21) Spatz, J. P.; Herzog, T.; Mossmer, S.; Ziemann, P.; Moller, M. *Advanced Materials* **1999**, *11*, 149-153.

(22) Meiners, J. C.; QuintelRitzi, A.; Mlynek, J.; Elbs, H.; Krausch, G. *Macromolecules* **1997**, *30*, 4945-4951.

(23) Forster, S.; Antonietti, M. *Advanced Materials* **1998**, *10*, 195-217.

(24) Wiese, H.; Rupaner, R. *Colloid and Polymer Science* **1999**, *277*, 372-375.

(25) Vanderhoff, J. W.; Park, J. M.; Elaaser, M. S. *ACS Symposium Series* **1992**, *492*, 272-281.

(26) Okubo, M.; Nakamura, M.; Ito, A. *Journal of Applied Polymer Science* **1997**, *64*, 1947-1951.

(27) Verbrugge, C. J. *Journal of Applied Polymer Science* **1970**, *14*, 897-909.

(28) Moffitt, M.; McMahon, L.; Pessel, V.; Eisenberg, A. *Chemistry of Materials* **1995**, *7*, 1185-1192.

(29) Note that oxidative side reactions have been reported when synthesizing PbS in the presence of oxygen.[30] Since H_2S exposure of our Pb-loaded samples was carried out in ambient atmosphere, the procedure may have resulted in nanoclusters of other compounds, e.g., $PbSO_4$, etc. We did not attempt to identify the chemical composition of these nanoclusters.

(30) Dutta, A. K.; Ho, T. T.; Zhang, L. Q.; Stroeve, P. *Chemistry of Materials* **2000**, *12*, 1042-1048.

(31) Meiners, J. C.; Elbs, H.; Ritzi, A.; Mlynek, J.; Krausch, G. *Journal of Applied Physics* **1996**, *80*, 2224-2227.

(32) *McGraw-Hill Encyclopedia of Science & Technology*; 7th ed.; McGraw-Hill: New York, 1992; Vol. 3.

Figure 3.1: Plan-view TEM of PS-b-PAA thin films spin-cast from 2.5 mg/mL mixture in toluene onto silicon nitride membrane; films loaded with $PbAc_{2(aq)}$

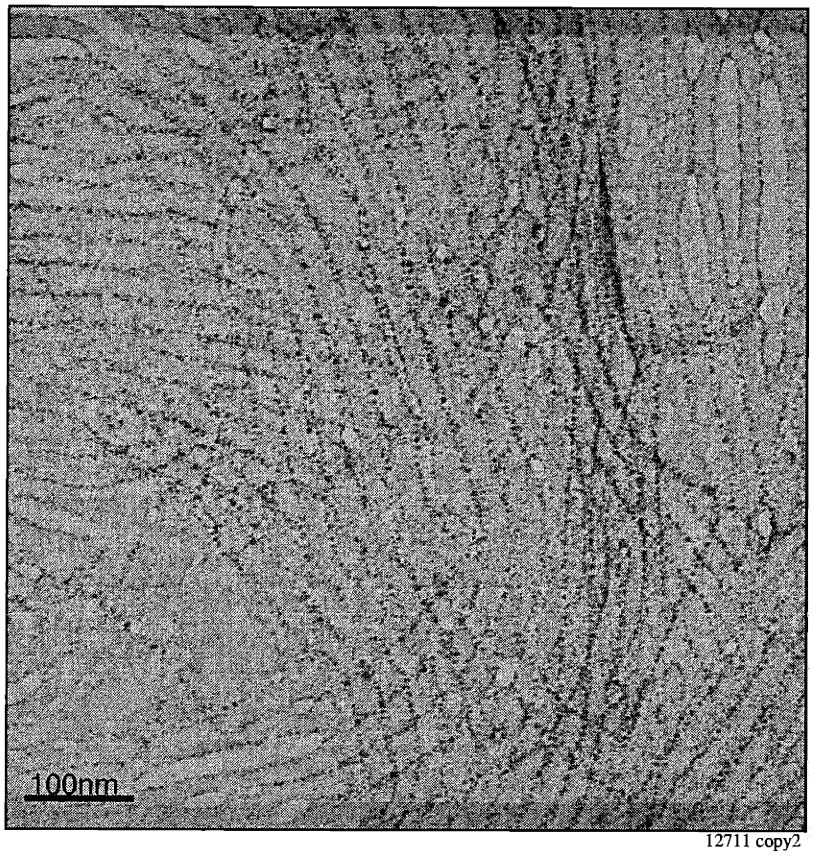

(A) film cast from room-temparature mixture

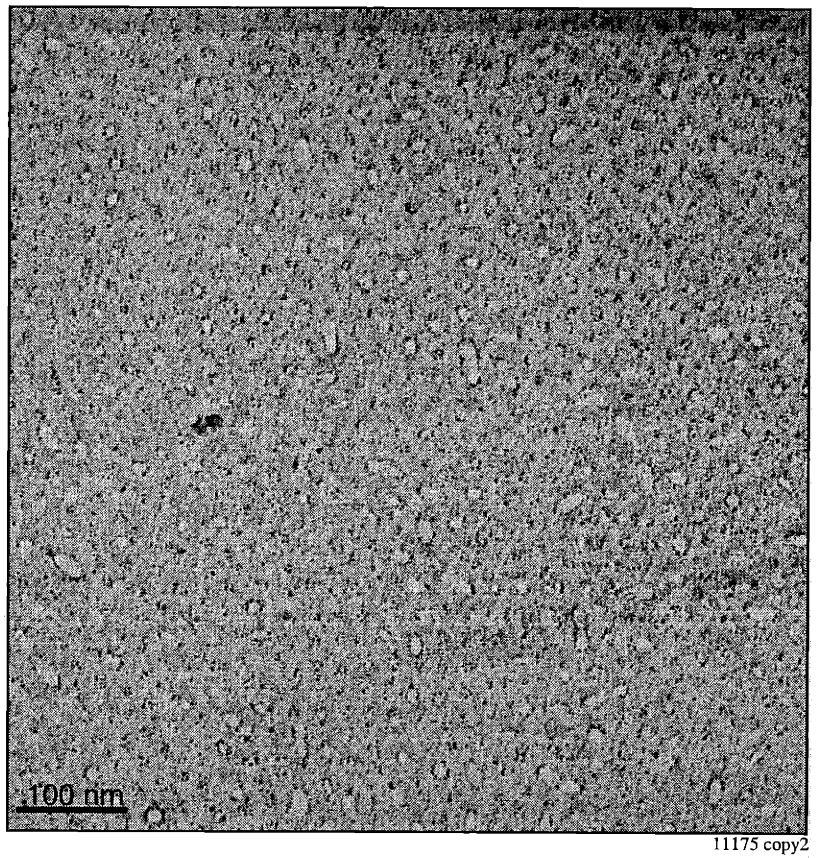

(B) film cast after a 108°C heating cycle

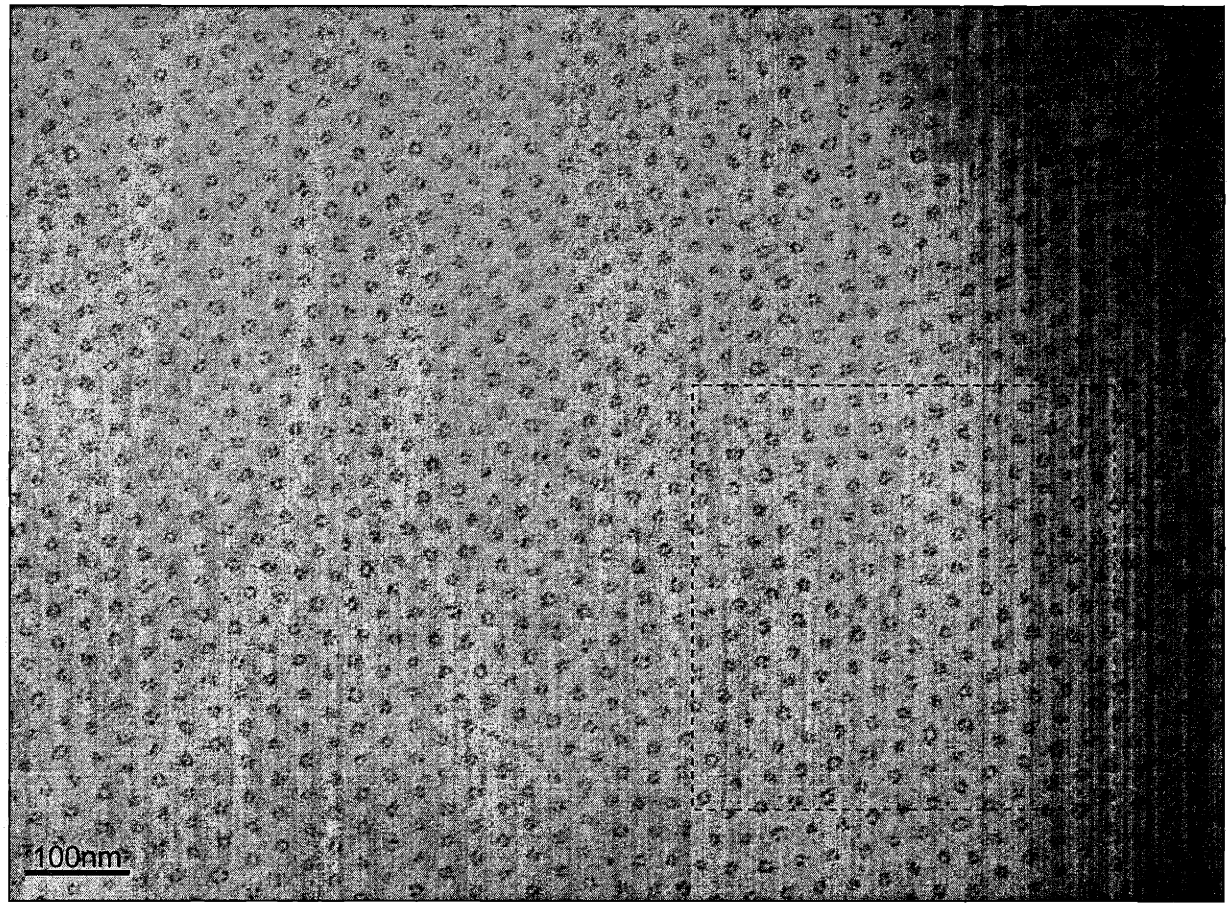

2D Fourier transform image

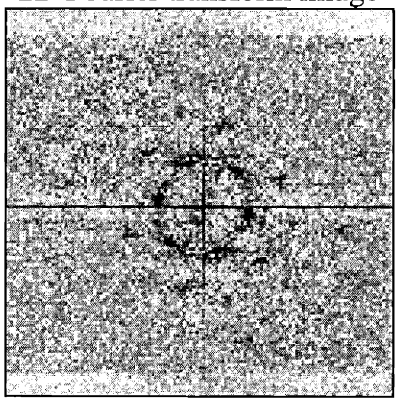

Figure 3.2: Plan-view TEM of PS-b-PAA thin film spin-cast after heating solution at 150°C for 20mins (and cooling to room temperature); film loaded with $PbAc_{2(aq)}$ (Inset: 2D Fourier transform image of the highlighted area)

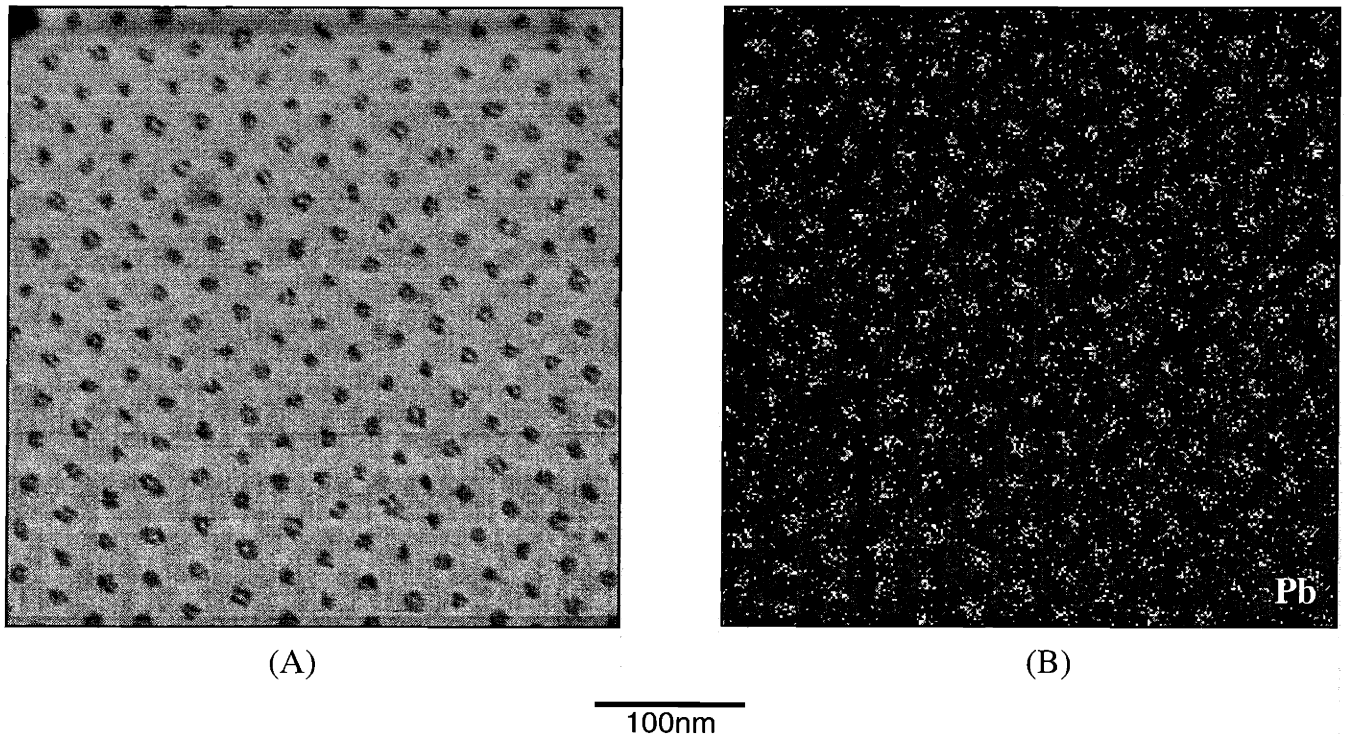

Figure 3.3: Scanning transmission electron micrograph (STEM) of PS-b-PAA micellar film loaded with $PbAc_{2(aq)}$
A. bright-field mode
B. associated elemental Pb map (Pb appears bright)

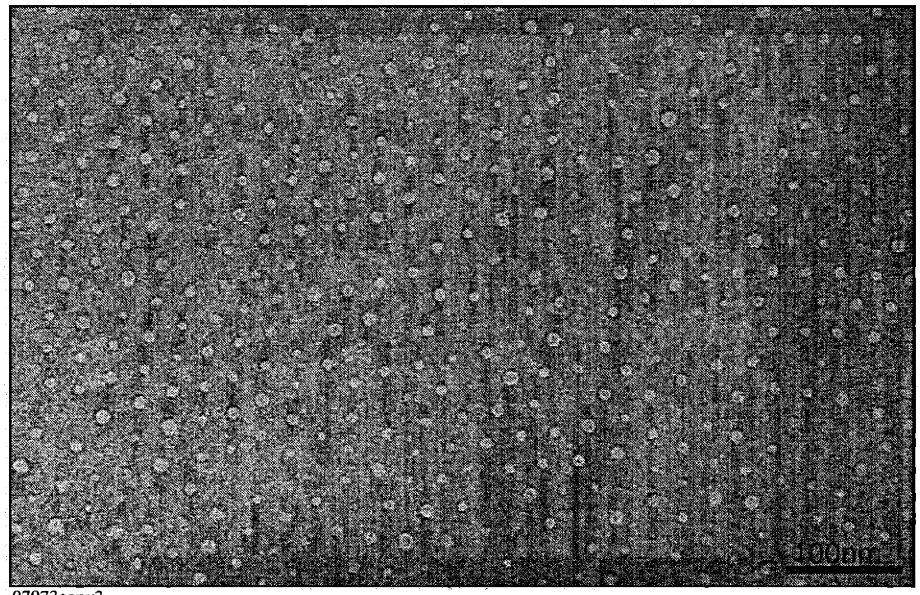

Figure 3.4: Plan-view TEM of micellar thin film on silicon nitride membrane loaded with $CdAc_{2(aq)}$

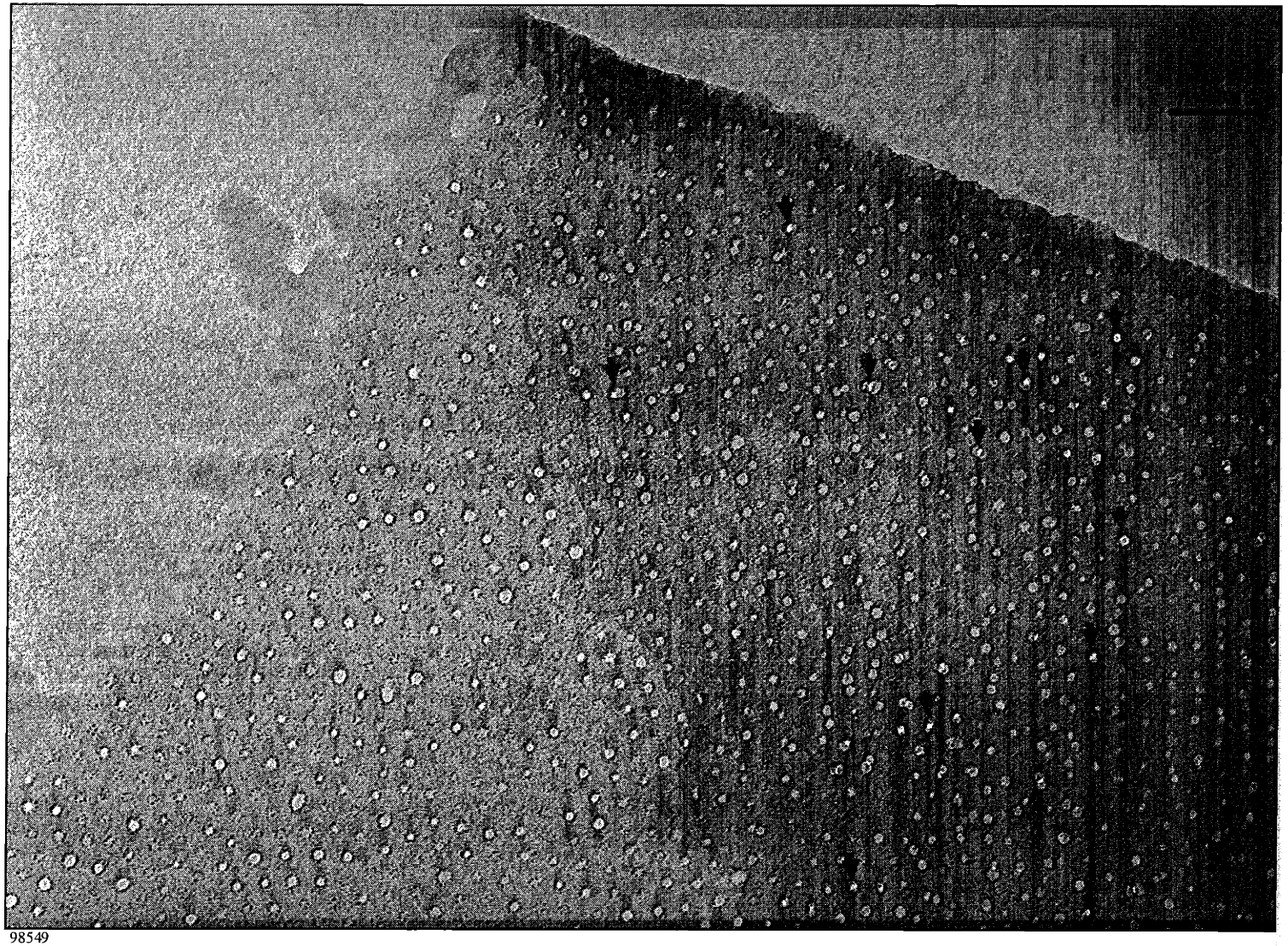

Figure 3.5: Plan-view T EM of micellar thin film on silicon nitride membrane loaded with $CuAc_{2(aq)}$
(Arrows indicate examples of enhanced illumination through overlapping PAA domains)

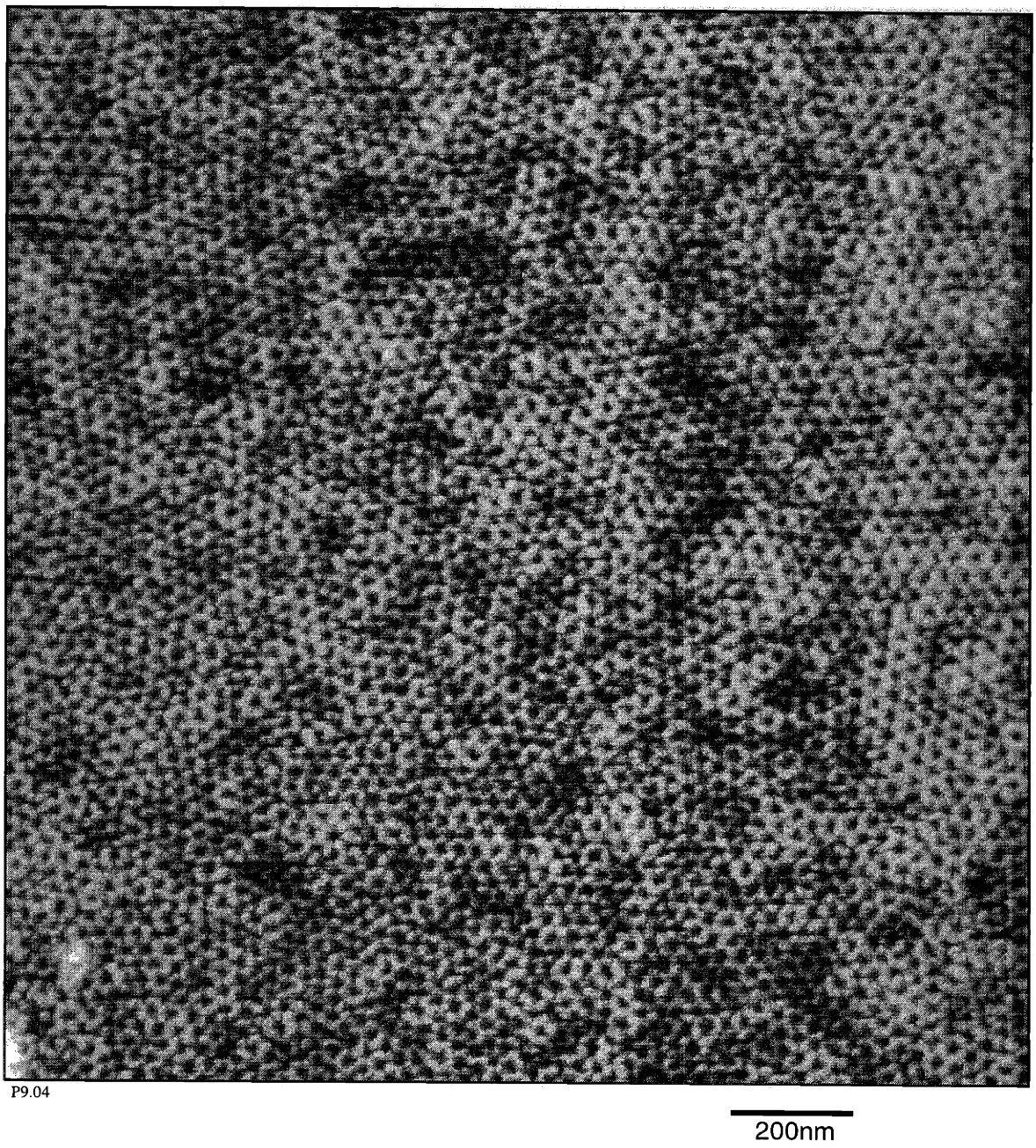

Figure 3.6: AFM height image of micellar thin film loaded with $CdAc_{2(aq)}$

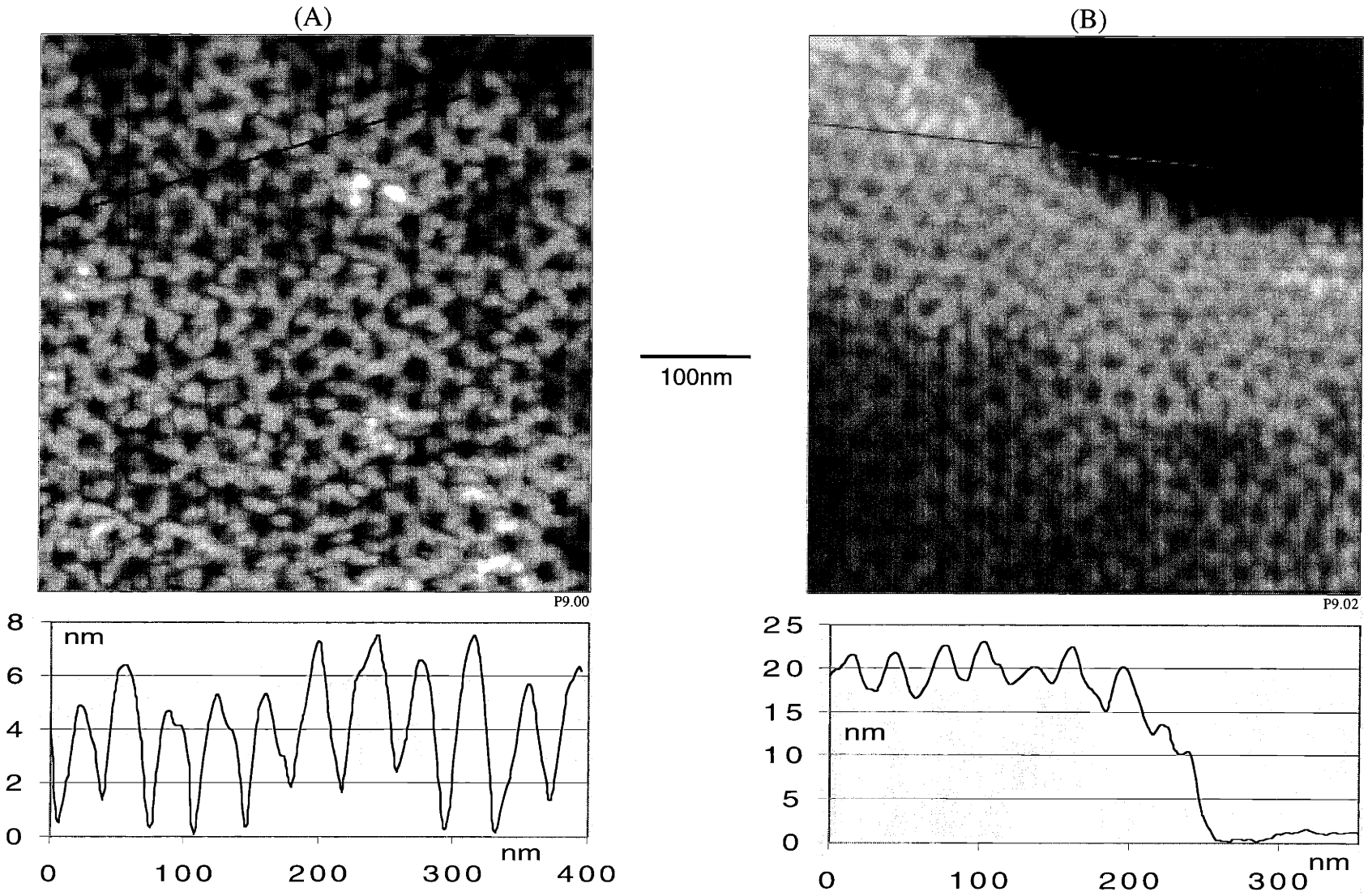

Figure 3.7 (A,B): AFM height images of micellar film loaded with $CdAc_{2(aq)}$ and associated 2D profiles

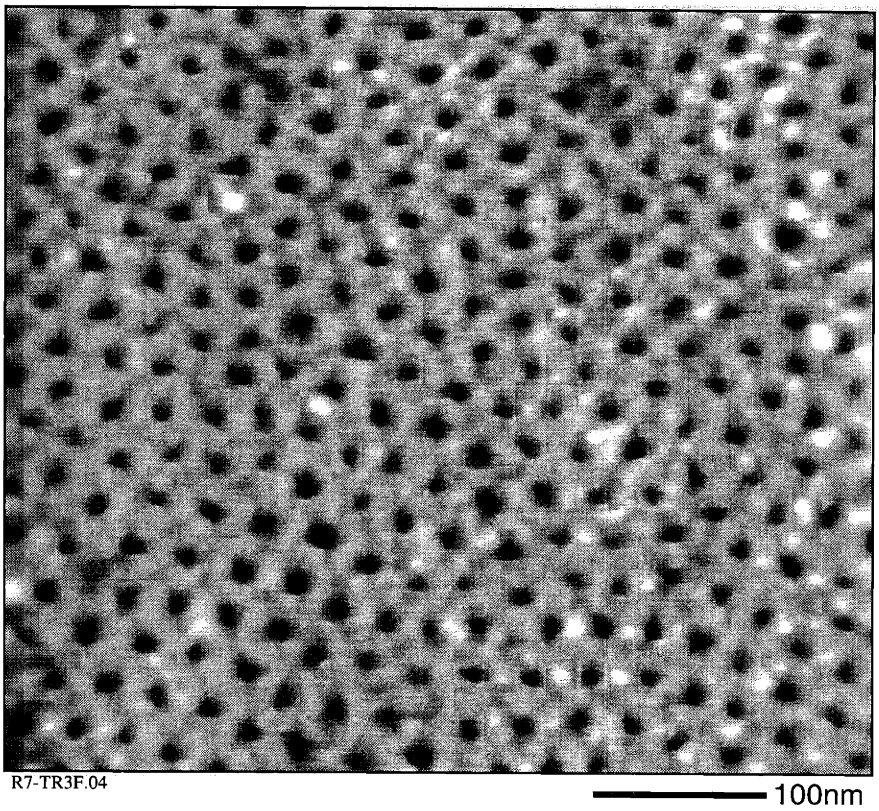

Figure 3.8: AFM height image of micellar thin film loaded with $CuAc_{2(aq)}$

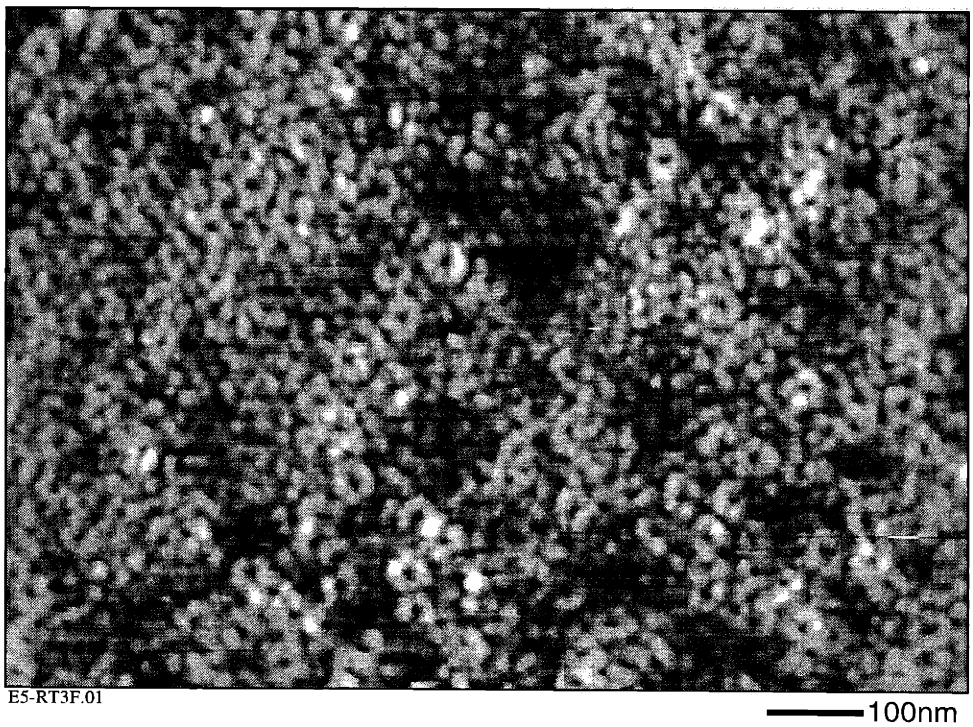

Figure 3.9: AFM height image of micellar thin film loaded with $PbAc_{2(aq)}$

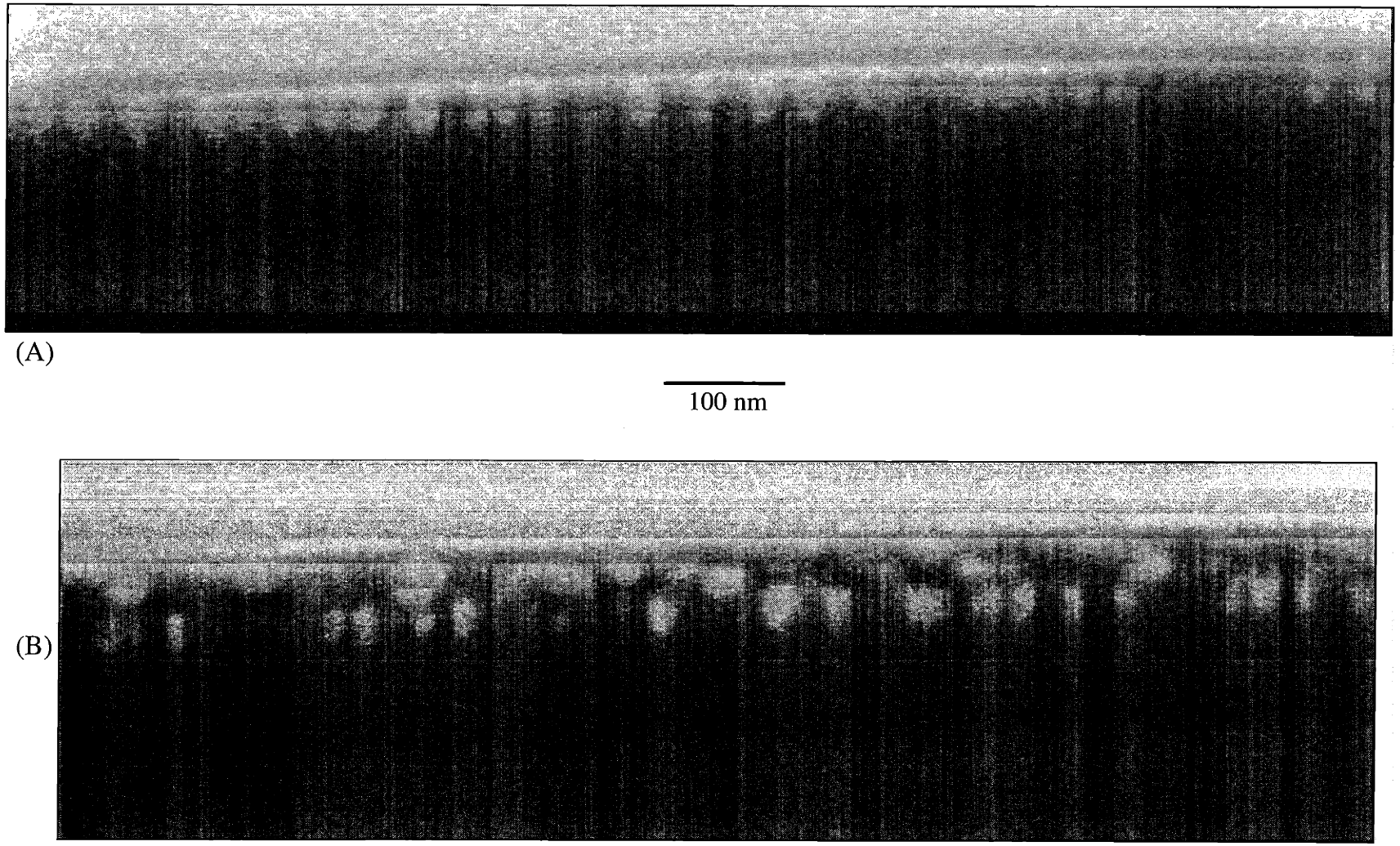

Figure 3.10 (A,B): Cross-sectional SEM profiles of PS-b-PAA thin film on silicon nitride membrane loaded with $[Pd(NH_3)_4]Cl_{2(aq)}$ (SEM by Yonathan Thio)

Figure 3.11: AFM height images of PS-b-PAA micellar thin films
(A) as-cast film (B) film treated in 0.04M $NaOH_{(aq)}$

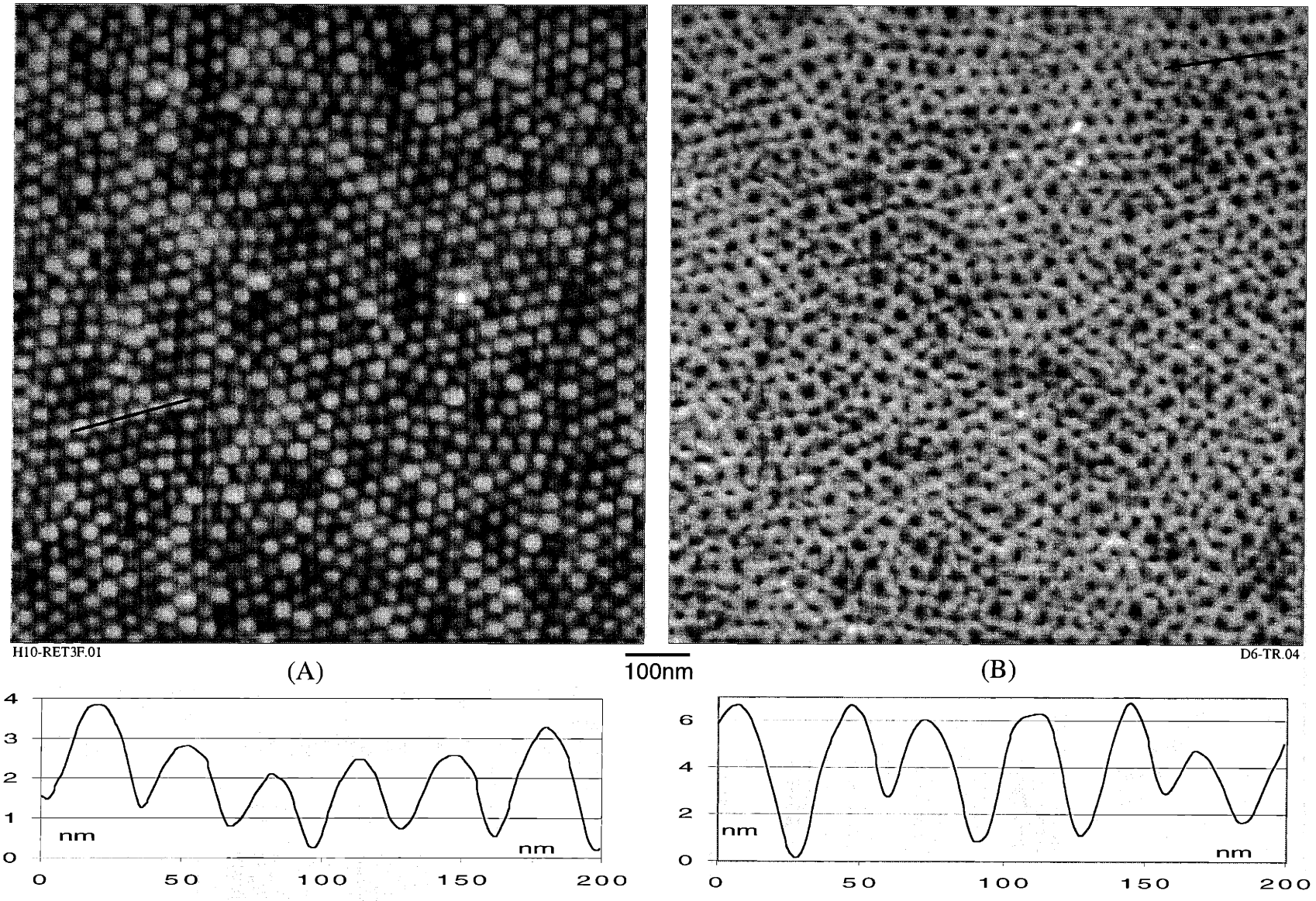

Scheme 3.1: Casting of entire spherical block copolymer micelles from selective solvent onto solid substrate

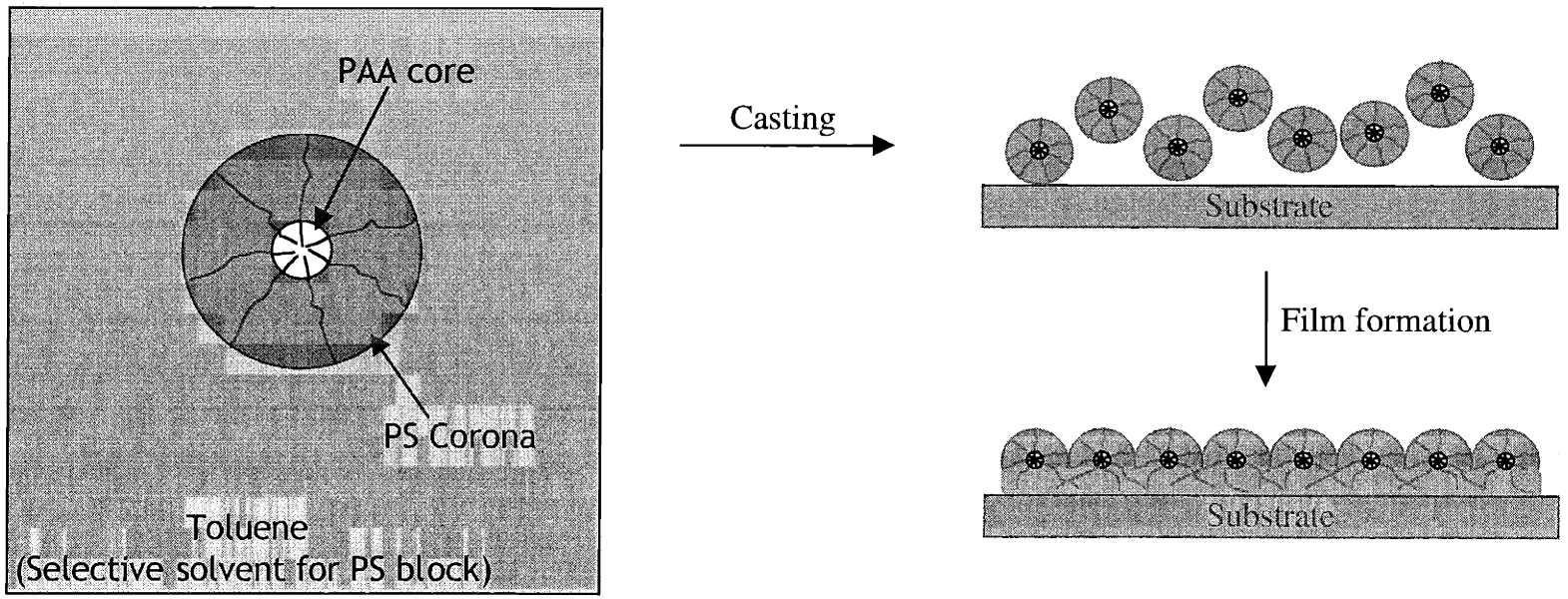

Scheme 3.2: Cavitation process of deposited PS-b-PAA micellar thin film upon treatment in $NaOH_{aq}$

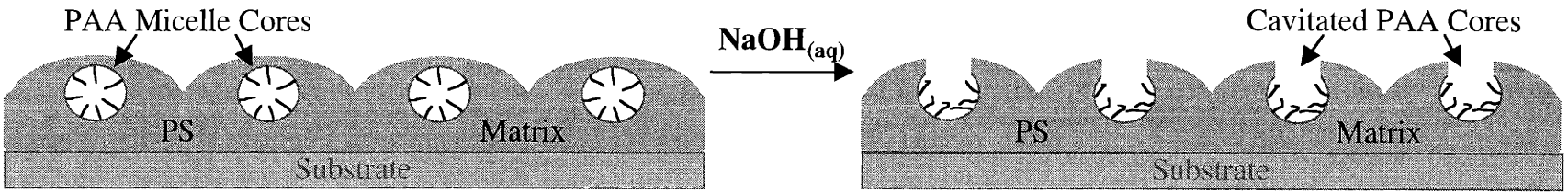

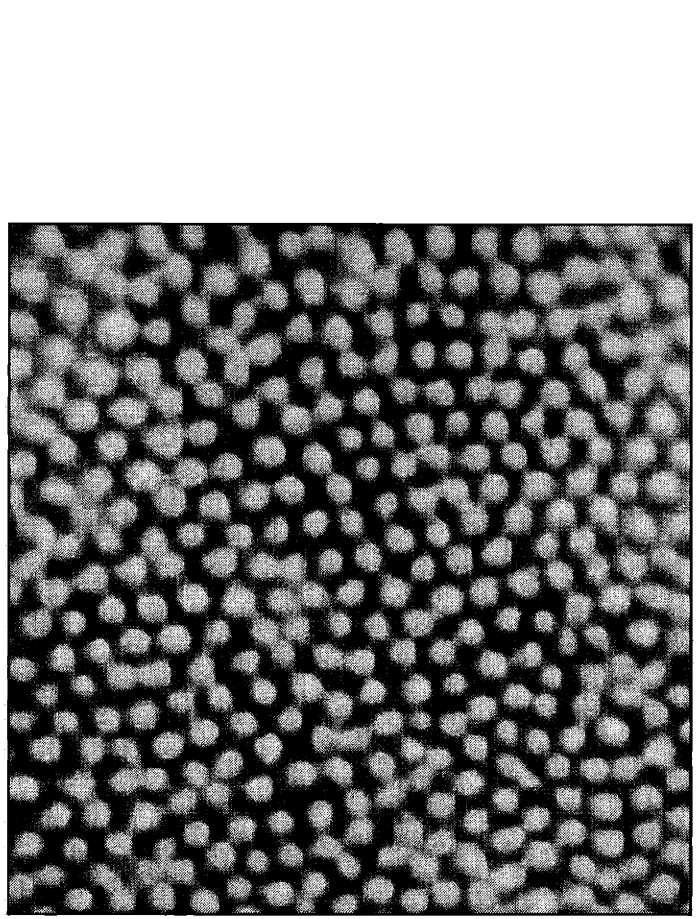

(A)

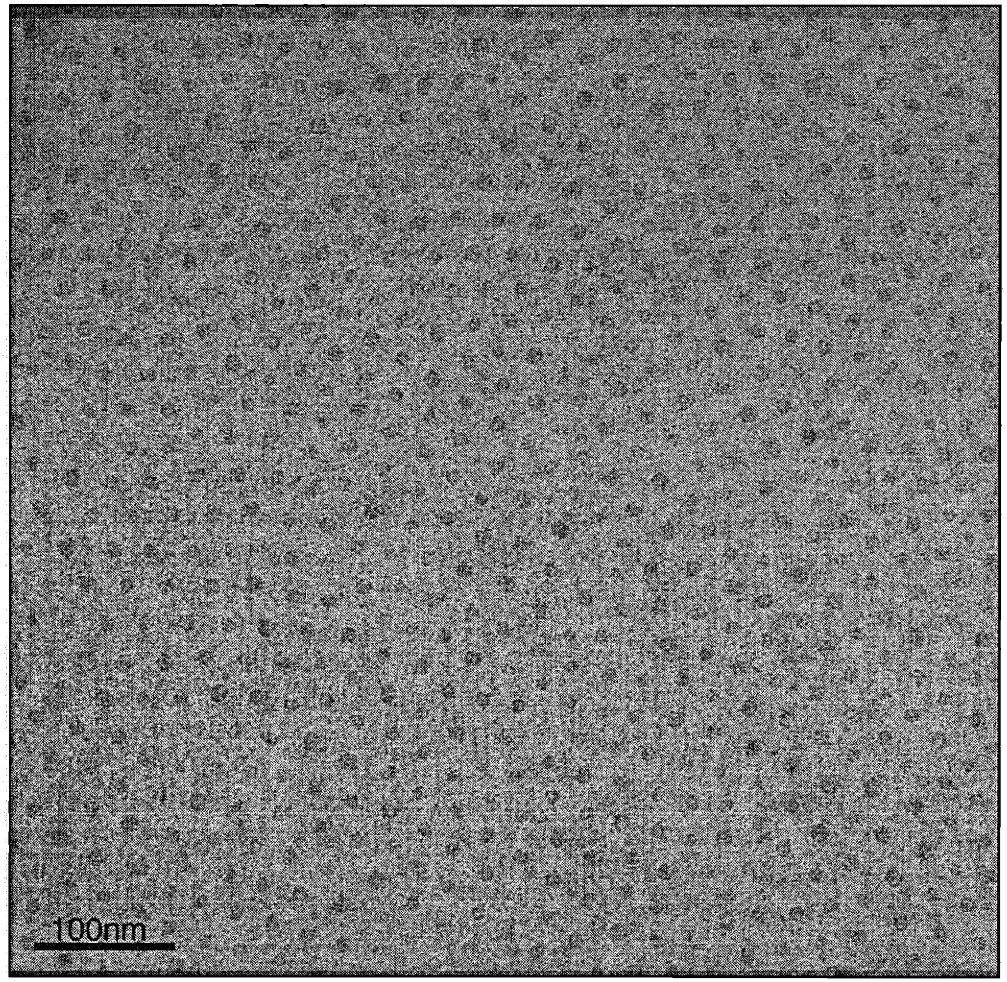

(B)

Figure 3.12: PS-b-PAA micellar thin film treated in $Ca(OH)_{2(aq)}$
A. AFM height image
B. plan-view TEM micrograph

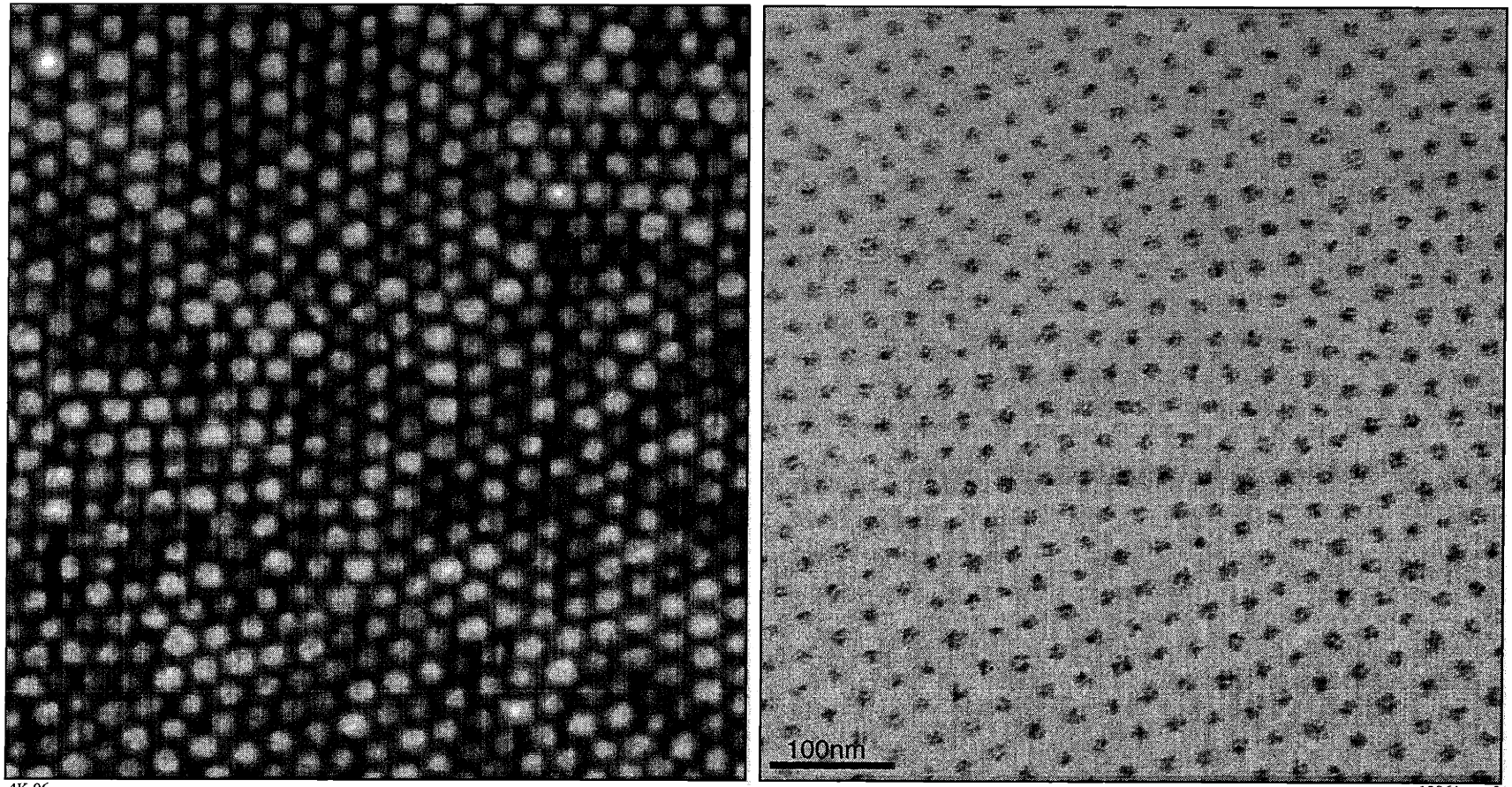

(A) (B)

Figure 3.13: PS-b-PAA micellar thin film treated in $PbAc_{2(aq)}$, bypassing $NaOH_{aq}$
A. AFM height image
B. plan-view TEM micrograph

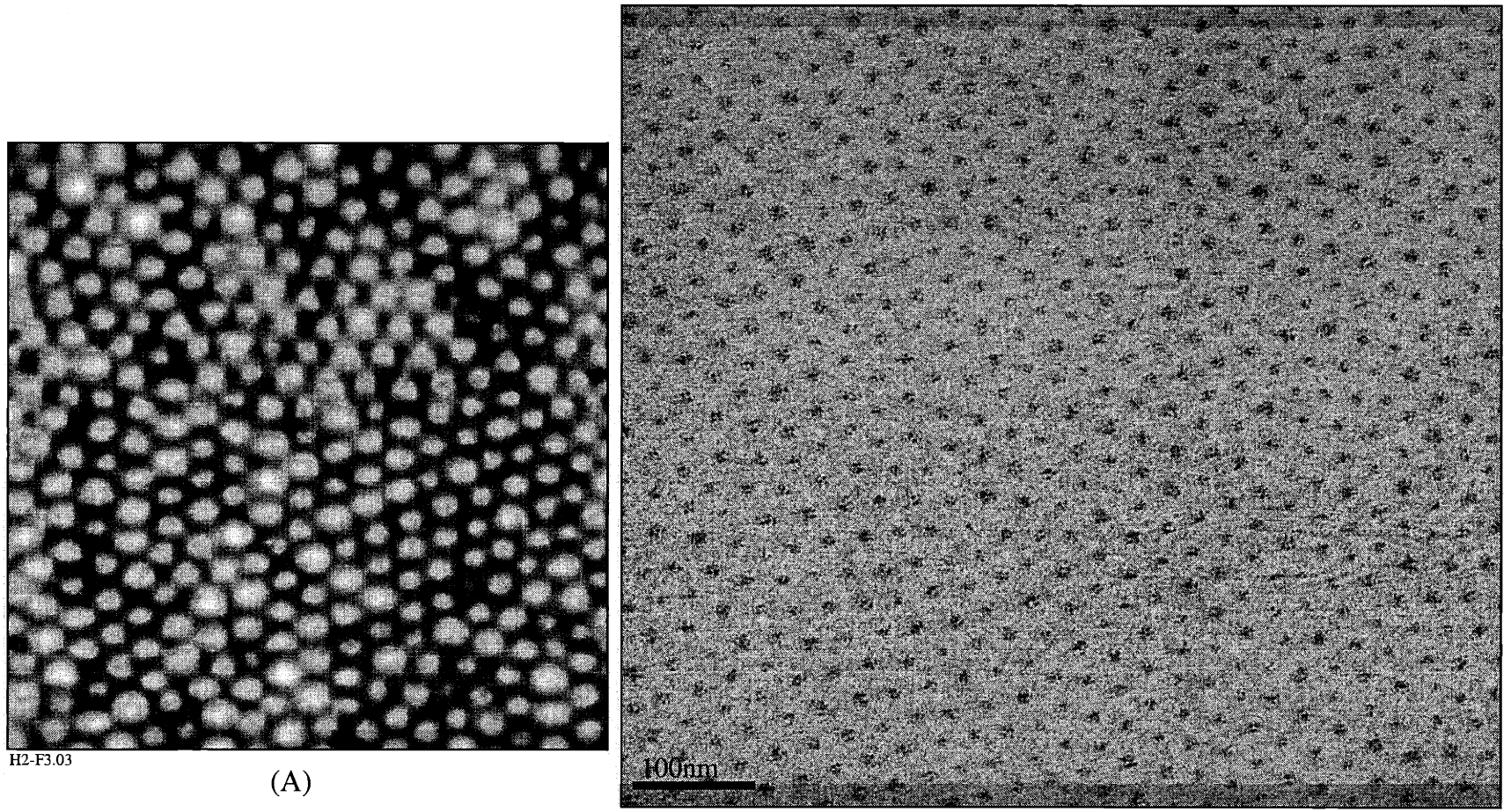

(A)

(B)

Figure 3.14: PS-b-PAA micellar thin film treated in $CdAc_{2(aq)}$, bypassing $NaOH_{aq}$
A. AFM height image
B. plan-view TEM micrograph

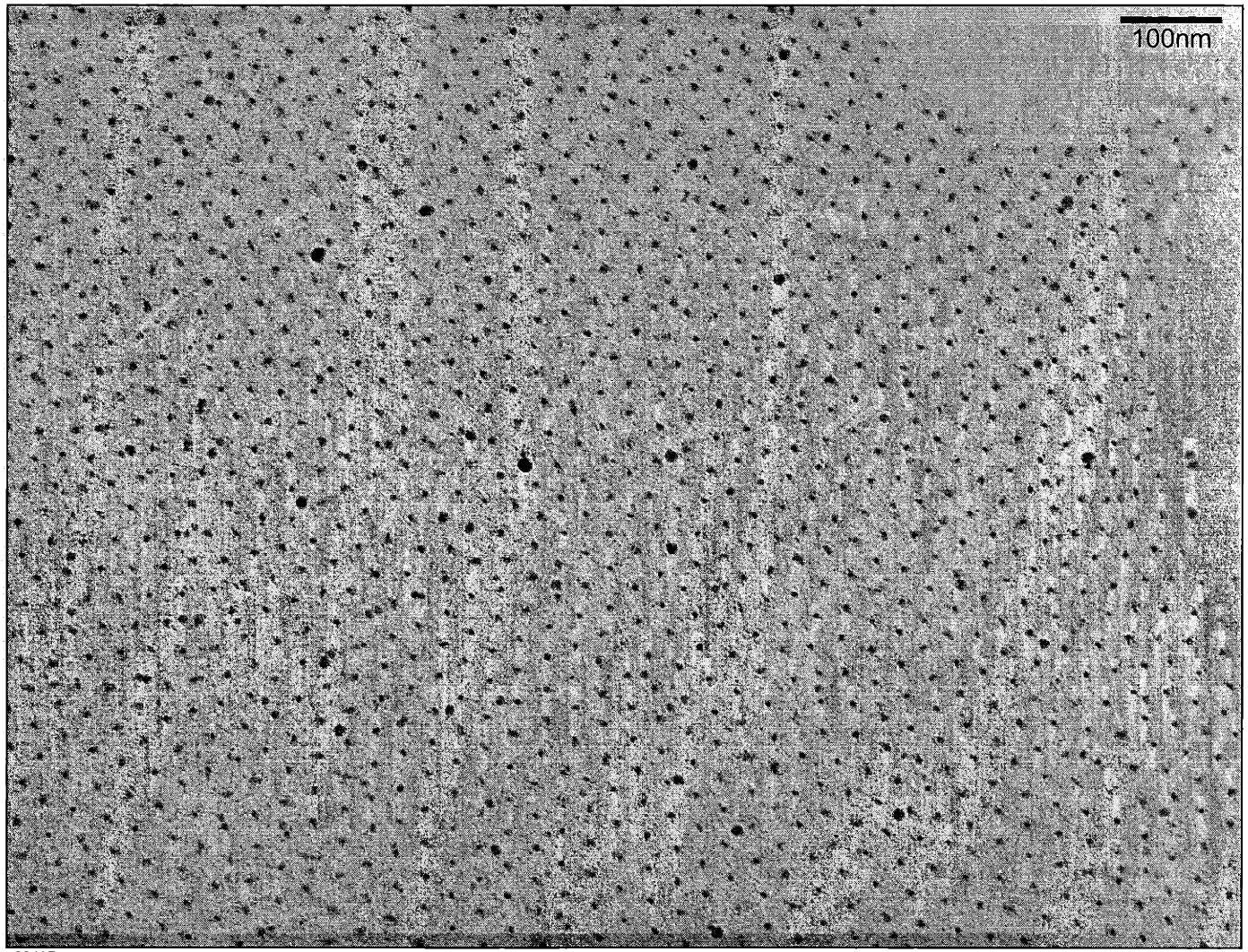

Figure 3.15: Plan-view TEM of PS-b-PAA micellar thin film containing Ag nanoclusters

(A)

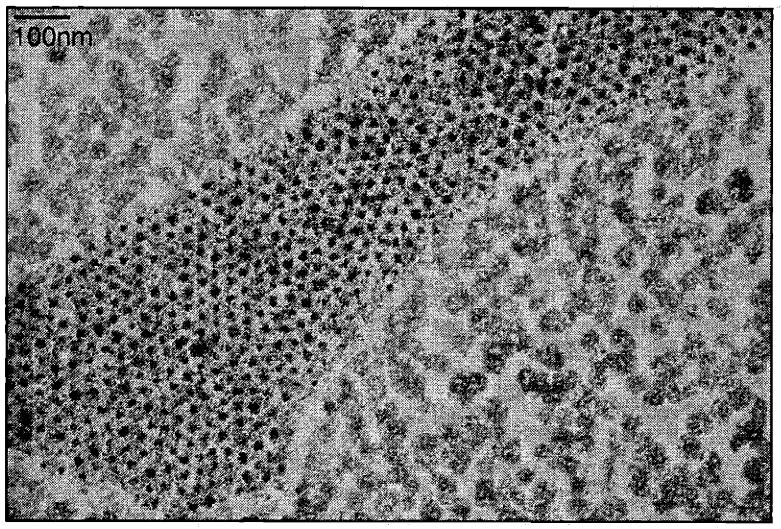

11404

(B)

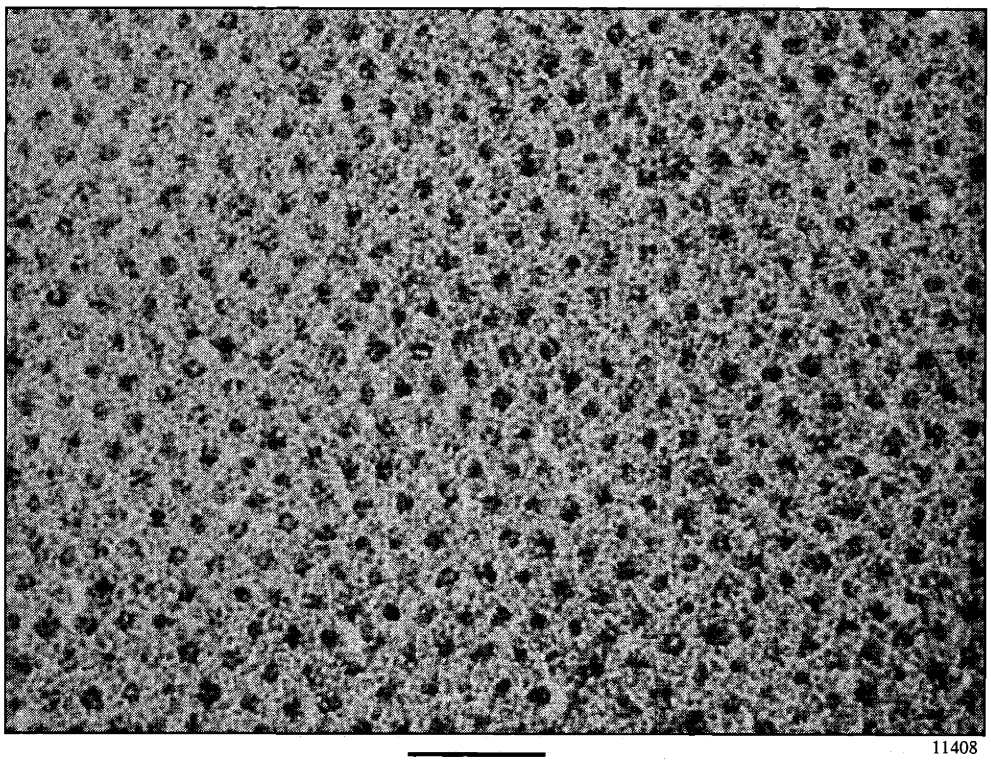

11408

100 nm

Figure 3.16(A,B): Plan-view TEM of micellar thin film treated in an electroless Ni plating bath

Figure 3.17: Plan-view TEM of micellar thin film loaded with $PbAc_{2(aq)}$

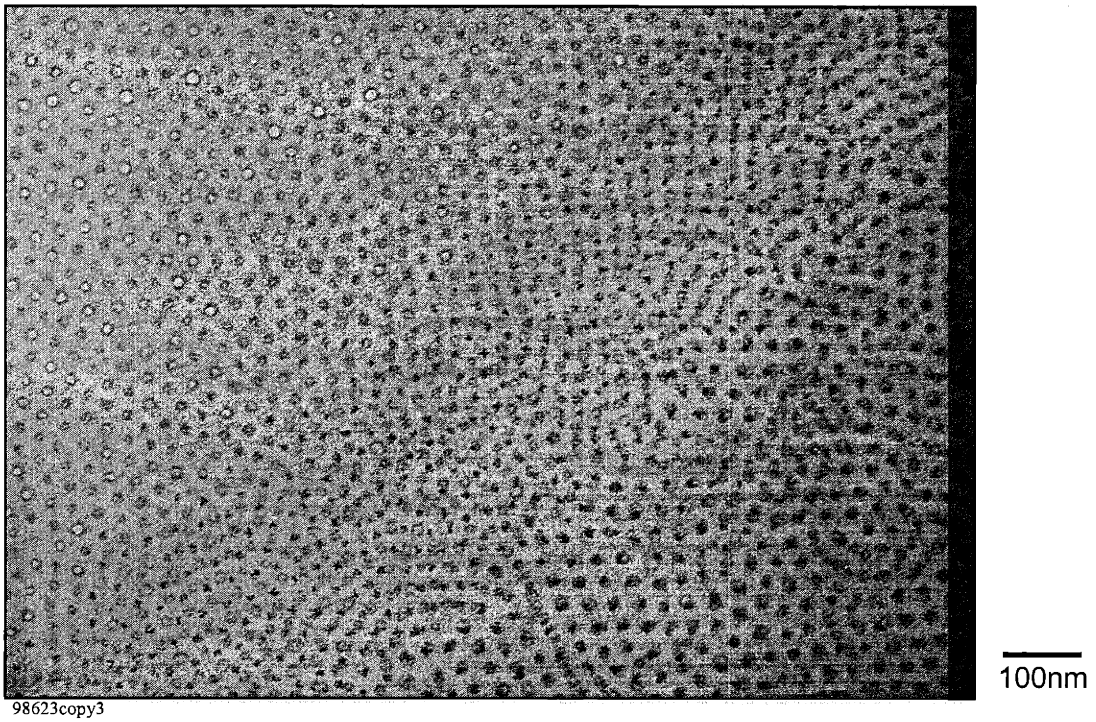

(A) observed transition in plan-view morphology associated with increasing film thickness

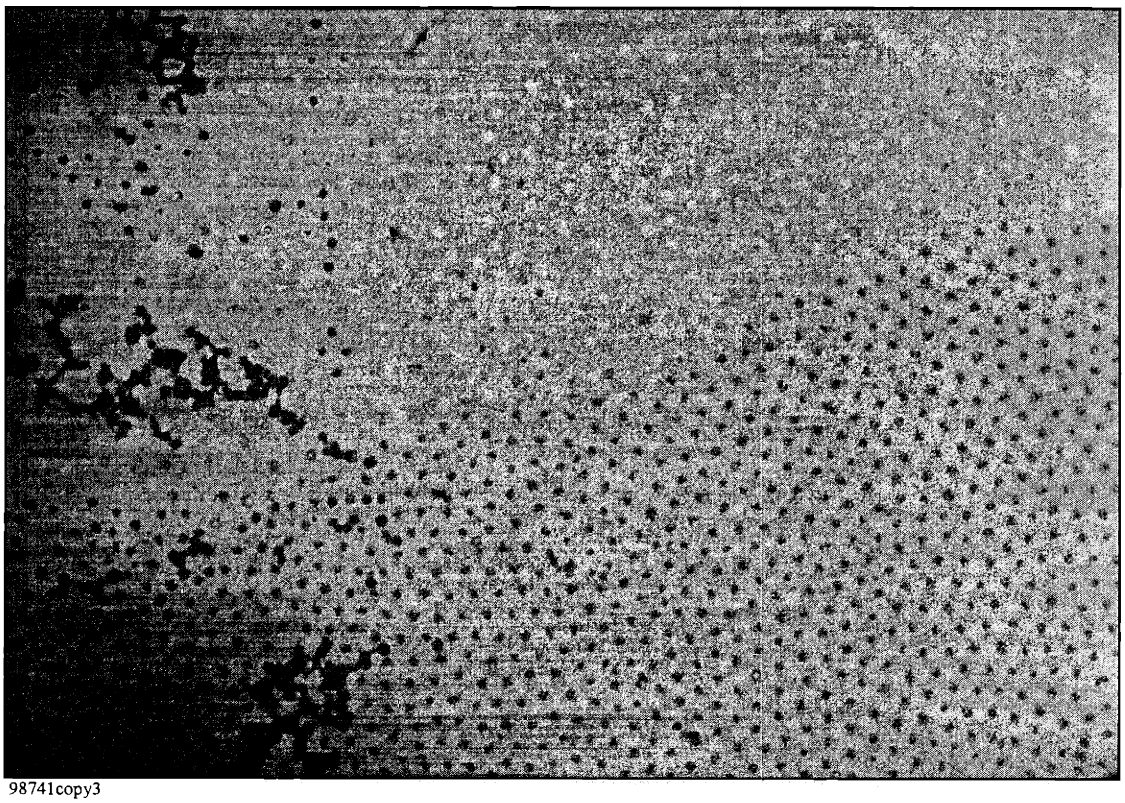

(B) after exposure to $H_2S_{(g)}$: depletion of cluster material from cavitated PAA domains on exposure to electron beam (same sample region as **Figure 3.17A**)

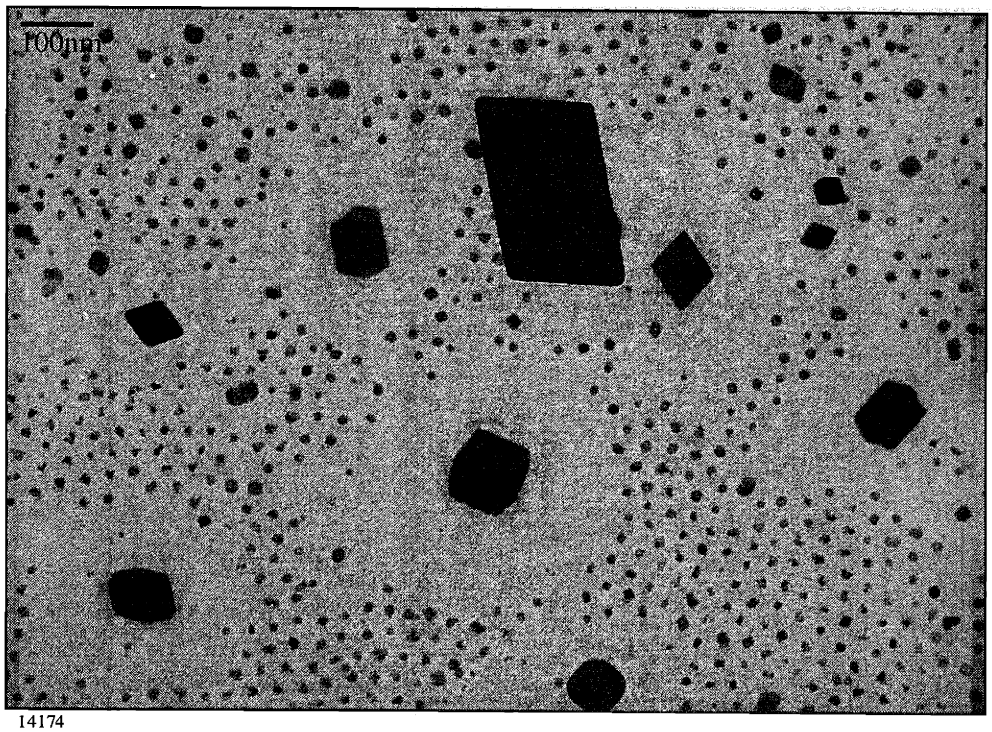

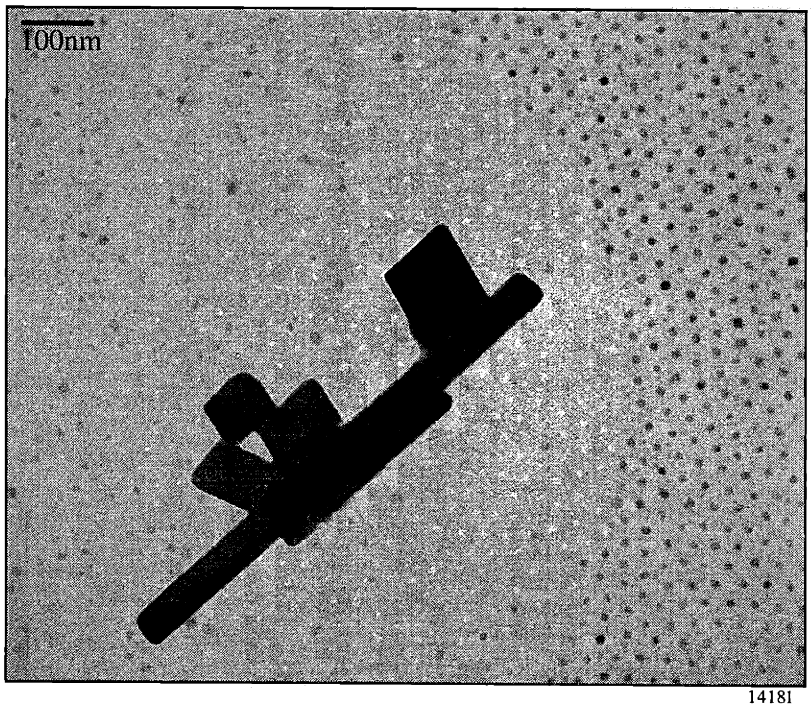

Figure 3.18(A,B): Surface objects formed on micellar film loaded with $PbAc_{2(aq)}$ and exposed to $H_2S_{(g)}$, with the observed depletion zones

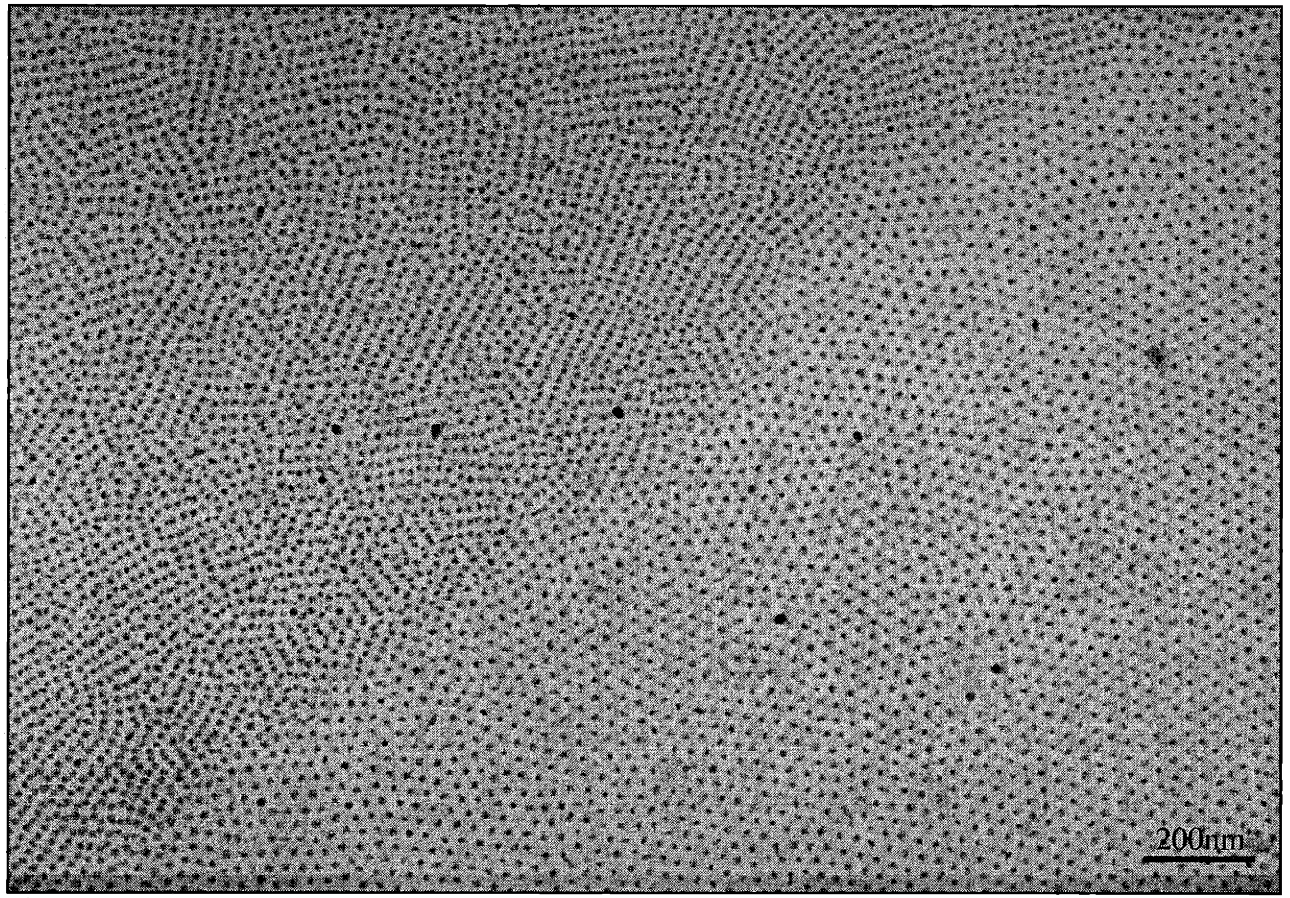

Figure 3.19: Representative plan-view TEM of thin film loaded with $PbAc_{2(aq)}$, bypassing $NaOH_{aq}$, and exposed to $H_2S_{(g)}$
(Note: morphological transition associated with film thickness variation)

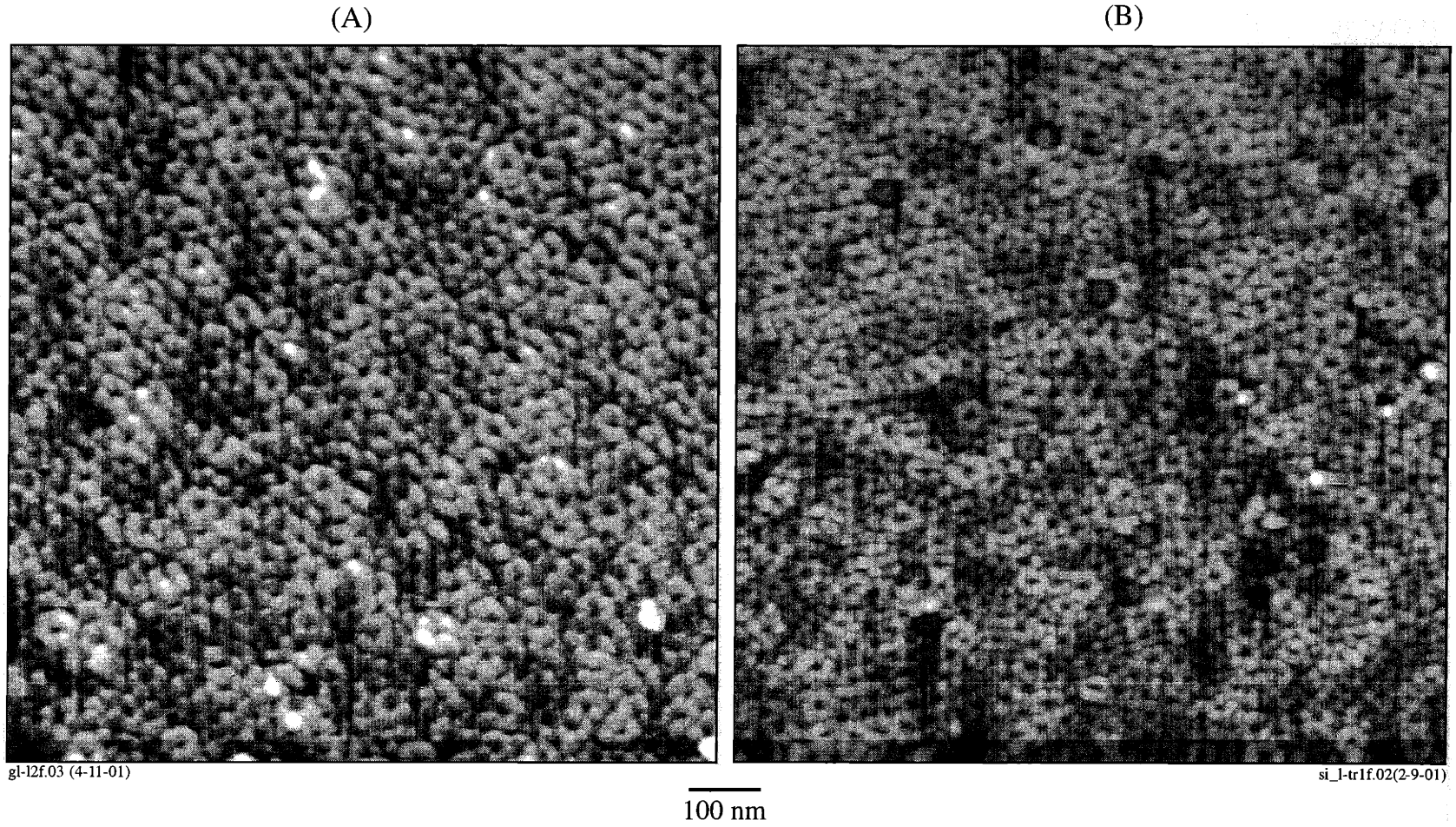

Figure 3.20: AFM height images of cavitated micellar thin films loaded with $CdAc_{2(aq)}$ supported on
A. glass slide
B. silicon wafer

Chapter 4
Thesis Summary

4.1 Conclusions

The first part of this thesis demonstrates that electroless metal deposition can be successfully induced within the subsurface lamellar NORCOOH microdomains of the $MTD_{400}NORCOOH_{50}$ diblock copolymer, using preloaded palladium as localized catalyst. The application of electroless deposition technique is a variation of the aqueous load-and-reduction (LARS) method (**Scheme 1.1**) developed by the Cohen group to synthesize in situ nanoclusters within block copolymers domains. The LARS technique relies on separate load and reduction steps to synthesize nanoclusters that are generally small (a few nanometers in size) and sparsely distributed in the microdomains. An advantage of electroless plating over such a serial technique is the effective combination of the load and the reduction steps into one continuous process through the autocatalytic reduction of the metal ions upon deposition. Thus, electroless plating represents a facile alternative to the serial LARS techniques to selectively deposit large amounts of metals in the carboxyl-containing microdomain templates.

Experimental results of Chapter 2 show that dense metallic structures can be generated within the microdomain of a bulk block copolymer over a relatively short time period. Selectivity of the deposition process results from the fact that both the transport of plating reagents from external reservoirs and the metal deposition take place along the same hydrophilic microdomain paths. However, while the rate of deposition can be rapid, the method is limited by the rate of diffusion of plating reagents into the interconnected carboxyl-containing microdomains. Continuous build-up of deposited metal along the microdomains near the sample's free surfaces hinders further diffusion of additional plating reagents into the bulk of the sample. Such limitation on reagent

transport is a drawback of this methodology, and a careful balance between the competing deposition and diffusion rates is necessary to achieve optimal deposition, especially within bulk block copolymer templates.

An initial goal of the latter part of this thesis was to apply the aqueous inorganic synthesis approach to templates of block copolymer thin films with laterally ordered microdomains to create in-plane arrays of nanoscale inorganics. An additional goal was to demonstrate the generality of the aqueous technique towards other carboxyl-containing block copolymer species aside from the ROMP-based block copolymers previously employed by our research group. As such, we employed block copolymer micellar thin films comprising hexagonal arrays of polyacrylic acid spherical domains embedded within the continuous matrix of polystyrene. The thin films were produced via direct deposition of reverse micelles assembled in toluene, where PAA forms the core and PS the corona. Successful use of these PAA domains as templates in which 2D hexagonal arrays of inorganic nanoclusters can be synthesized is illustrated in Chapter 3.

In addition to meeting the above goals, novel aspects regarding the structural development of micellar thin films themselves are also presented. Upon treatment in monovalent base (NaOH) solution – performed to facilitate the subsequent uptake of transition metal ions into the carboxyl-containing domains (**Scheme 1.1B**) – the hydrophilic PAA domains swell and eventually cavitate as a result of hydration. This cavitation process leads to the formation of in-plane arrays of surface cavities that expose the PAA cores to the free surface; thus, creating open nanoreactors in which nanoclusters can be synthesized. We also provide experimental evidence to show that such cavitation of the PAA domains can be suppressed via ionic cross-linking of the PAA chains by sequestered divalent metal cations. That is, metal loading of the PAA domains can also be

achieved without the cavitation process by omitting the NaOH treatment step (**Scheme 1.1A**), and the resulting PAA cores remain shielded from the free surface by the intact PS corona layer. These closed nanoreactors offer additional stability – relative to their cavitated (open) counterparts – to nanoclusters synthesized within them. The option to employ either the open or the closed micelles as templates represents a potentially useful adaptability of the system.

The self-assembled micellar films may be useful towards current efforts on miniaturization of devices. The ability to selectively decorate the PAA cores with magnetic particles - possibly via electroless cobalt deposition - could contribute to enhancing data storage capacity in magnetic recording media[1] owing to high areal density of the micellar self-assembly. The composite thin films may also be used as nanolithographic masks.[2] In addition to using the micellar films as in situ templates for functional nanoscale inorganics, we are also currently planning to employ these films as biological substrates: there is interest in the study of the influence of nanoscale substrate topography on the adhesion and behavior of cells.[3] Besides its unique and adjustable surface topography, the micellar films also offer the possibility of creating bio-specific substrates via chemical tethering of cell-binding ligands to the carboxylic acid groups present through the cavitated PAA domains.

4.2 Directions for future investigations

4.2.1 Selective electroless metal deposition

As an extension of the work presented in Chapter 2, the deposition of other electroless metals within block copolymer microdomains may be investigated in order to take advantage of various functional properties offered by different metals. In terms of nanocluster synthesis, electroless deposition may be employed – perhaps in combination with the LARS technique – as a means to increase the size of in situ nanocluster; thus, tuning their size-dependent properties. Also, one

may wish to explore different varieties of polymeric structures as templates for electroless deposition to create novel nanocomposites. For example, selective electroless deposition may also occur in other water-permeable block copolymer microdomains that are not carboxyl-functionalized. In addition to block copolymers, selective electroless metal plating has recently been achieved in the templates of heterostructured polyelectrolyte multilayer systems.[4]

4.2.2 Cavitated block copolymer micellar thin films

Characterization of the cavitated micellar thin films

Chapter 3 outlines our attempt to characterize the cavitated PS-b-PAA deposited micelles using AFM in order to determine the depth of the individual cavities, which may in turn determine the value of the thin films towards future applications. However, the AFM resolutions were limited by probe-sample convolution since the conventional AFM tips used in this work (diameters ~10nm or larger) were comparable in size with the dimensions of the cavities. As mentioned earlier, the use of AFM tips with smaller diameters (from commercial sources or by manual construction)[5] may be attempted to better determine the dimensions of these cavities.

There are alternative methods that may provide indirect measurements for the cavity dimensions. By constructing the cavitated micellar thin film on a conducting substrate, one may attempt to perform electrodeposition of metals through the cavitated micellar thin film template where the conducting substrate would serve as the cathode. (Ultra-high density cobalt nanowires have been fabricated within etched cylindrical pores of a block copolymer template via such direct current electroplating.)[6] Successful growth of metals from the substrate through the cavities would indicate that the depth of cavities extends through the film to the substrate, and would also represent another method for creating dense lateral metallic nanoarrays within the micellar thin film templates.

Characterization of the cavitation process

The preliminary experimental results of Chapter 3 demonstrate that pH condition (degree of ionization of the PAA carboxyl groups) and valency of the loaded metal cations (ionic crosslinking) play essential roles in the swelling of PAA cores and subsequent cavitation of the micelles. These parameters enable the creation of open vs. closed micellar nanoreactors. However, a finer control over the cavitation process - i.e., the degree of PAA core's exposure to the free surface - may be achievable. The ability to precisely manipulate the cavitation process and the resulting thin film property would render the system more versatile and attractive towards future applications. Therefore, more detailed investigation of the effects of pH and ionic crosslinking on the structural transformation of the micellar thin films is warranted. In addition, attention should be paid to determine whether or not such cavitation process is a reversible one.

Another potentially important parameter yet to be investigated is ionic strength. It is commonly known that charge shielding effects by counterions of dissolved salts strongly influence chain conformation of ionic polymers in aqueous environments.[7-9] At low ionic strength, ionized chains adopt an extended conformation due to repulsive forces among ionized groups on the chain, while at high salt concentration electrostatic screening by the salt ions leads to a denser globular chain conformation. Influences of ionic strength on the conformation of PAA chains within the deposited micelle cores may also be anticipated. Hypothetically, shrinkage of ionized PAA chains in a salty solution due to electrostatic screening among the COO^- groups may lead to shrinkage of the PAA core; thus, moderating the observed pH-induced swelling and cavitation. Future investigation is needed to evaluate the potential use of ionic strength as a variable to control the final structure of the micellar thin films.

Preliminary experiments also revealed that a 45-minute $NaOH_{aq}$ treatment time results in micelle cavities that are less pronounced than after a 24-hour treatment. Thus, length of treatment time in the base is another anticipated cavitation-controlling variable, and the kinetics of the cavitation process should also be explored. We note that in addition to the ex-situ observation in air, in-situ AFM imaging can also be performed in liquid media.[10,11] For example, liquid-cell AFM has successfully been employed to visualize the 3D topographic features of polymeric surfaces in order to study their degradation kinetics in aqueous environment (e.g., as a function of pH).[12-14] We believe that in-situ AFM imaging in aqueous solutions would also be a valuable tool for monitoring, in real time, the cavitation process of our micellar thin films, as well as the effects of aforementioned parameters on the deposited micelles' structural evolution.

Characterization of the micelles in solution

In addition to the behavior of deposited micelles, basic information regarding aggregation process and solution behavior of the micelles will be necessary in order to optimize and fully exploit the potentials of the PS-b-PAA micellar thin films. So far, only a limited number of studies exist in the literature on the PS-b-PAA micellar system. Eisenberg and co-workers have investigated reverse micelles of styrene-block-metal acrylate (i.e., neutralized version of the acrylic acid block) and their application as templates for inorganic nanocluster synthesis.[15,16] Researchers have also reported the formation of PS-b-PAA micelles in polar media, where PS is the core-forming block - i.e., not reverse micelles.[17-19] Unfortunately, these studies are not directly applicable to our current system of PS-b-PAA reverse micelles in toluene, for which solution properties should therefore be investigated.

Relevant solution properties include the critical micelle concentration (CMC), architecture of the micellar assemblies, structural transformation of the aggregates such as the cylinder-to-sphere

transformation (e.g., upon heating as outlined in section 3.3, or upon reducing polymer concentration in solution[20,21]), and stability of the micelles in solution. (We note that the PS-b-PAA spherical reverse micelles of our current investigation appear to have a limited lifetime ranging between 6-15 months.) A number of experimental techniques are available for studying micelles in solution: light scattering, small-angle X-ray and neutron scattering, size-exclusion chromatography (GPC), viscometry, etc.[22,23] For example, the transition between cylindrical and spherical micelles can be observed with a combination of static and dynamic light scattering experiments.[24] Note that in addition to using spherical micelles, the line structure of cylindrical micelles - which can be oriented upon deposition onto substrates, e.g., via capillary forces[25] - also offers the possibility of templating inorganic nanowires.

Optimization

As mentioned in Chapter 3, an improved uniformity in film thickness and areal coverage is desirable for future utilization of the micellar thin films. To address this issue, alternative film casting techniques such as dip casting[2,26] may be explored. Other relevant parameters that influence the casting process include solution concentration[21] and the speed at which the casting solution is removed from substrates. It has been shown that the velocity of substrate withdrawal from the micellar solution upon dip casting influences the lateral ordering of the deposited micelles as well as deposited film thickness.[2,26] Improving film uniformity may also require an enhanced wettability of the substrate by the micellar solution (casting solvent).[2] This could be achieved via chemical modification of the substrate surfaces. Alternatively, one may wish to explore different substrate types - e.g., of varying surface polarities - in order to optimize film uniformity, as well as to examine whether the deposition and cavitation of the micelles are substrate-dependent.

The dimensions of the micelles can be readily tailored for future applications by modifying the molecular weight of the block copolymer (relative and absolute block lengths) or by adding styrene homopolymer to enlarge the PS matrix of the micellar film.[20] Finally, one may wish to explore employing reverse micelles of other carboxyl-containing amphiphilic block copolymer to study the potential generality of the cavitation process, as well as to take advantage of potentially desirable properties inherent in different polymer species.

4.3 References

(1) Ross, C. A.; Smith, H. I.; Savas, T.; Schattenburg, M.; Farhoud, M.; Hwang, M.; Walsh, M.; Abraham, M. C.; Ram, R. J. *Journal of Vacuum Science & Technology B* **1999**, *17*, 3168-3176.

(2) Spatz, J. P.; Herzog, T.; Mossmer, S.; Ziemann, P.; Moller, M. *Advanced Materials* **1999**, *11*, 149-153.

(3) Flemming, R. G.; Murphy, C. J.; Abrams, G. A.; Goodman, S. L.; Nealey, P. F. *Biomaterials* **1999**, *20*, 573-588.

(4) Wang, T. C. Ph.D. Thesis, MIT, 2002.

(5) Commercially available probes currently offer tip diameters as small as 3nm, with relatively high aspect ratios, albeit expensive. For examples, see http://www.piezomax.com (carbon nanotube tips) and http://www.molec.com (SuperSharpSilicon® tips). Alternatively, directions for manual mounting of carbon nanotubes to conventional AFM probes are available at http://cnst.rice.edu/mount.html.

(6) Thurn-Albrecht, T.; Schotter, J.; Kastle, C. A.; Emley, N.; Shibauchi, T.; Krusin-Elbaum, L.; Guarini, K.; Black, C. T.; Tuominen, M. T.; Russell, T. P. *Science* **2000**, *290*, 2126-2129.

(7) Ahrens, H.; Forster, S.; Helm, C. A. *Physical Review Letters* **1998**, *81*, 4172-4175.

(8) Ladam, G.; Schaad, P.; Voegel, J. C.; Schaaf, P.; Decher, G.; Cuisinier, F. *Langmuir* **2000**, *16*, 1249-1255.

(9) Zhulina, E. B.; Wolterink, J. K.; Borisov, O. V. *Macromolecules* **2000**, *33*, 4945-4953.

(10) Drake, B.; Prater, C. B.; Weisenhorn, A. L.; Gould, S. A. C.; Albrecht, T. R.; Quate, C. F.; Cannell, D. S.; Hansma, H. G.; Hansma, P. K. *Science* **1989**, *243*, 1586-1589.

(11) Weisenhorn, A. L.; Macdougall, J. E.; Gould, S. A. C.; Cox, S. D.; Wise, W. S.; Massie, J.; Maivald, P.; Elings, V. B.; Stucky, G. D.; Hansma, P. K. *Science* **1990**, *247*, 1330-1333.

(12) Shakesheff, K. M.; Davies, M. C.; Domb, A.; Jackson, D. E.; Roberts, C. J.; Tendler, S. J. B.;

Williams, P. M. *Macromolecules* **1995**, *28*, 1108-1114.

(13) Davies, M. C.; Shakesheff, K. M.; Shard, A. G.; Domb, A.; Roberts, C. J.; Tendler, S. J. B.; Williams, P. M. *Macromolecules* **1996**, *29*, 2205-2212.

(14) Rossini, C. J.; Arceo, J. F.; McCarney, E. R.; Augustine, B. H. *Macromolecular Symposia* **2001**, *167*, 139-151.

(15) Moffitt, M.; McMahon, L.; Pessel, V.; Eisenberg, A. *Chemistry of Materials* **1995**, *7*, 1185.

(16) Moffitt, M.; Eisenberg, A. *Macromolecules* **1997**, *30*, 4363-4373.

(17) Zhang, L. F.; Barlow, R. J.; Eisenberg, A. *Macromolecules* **1995**, *28*, 6055-6066.

(18) Zhang, L. F.; Eisenberg, A. *Macromolecules* **1999**, *32*, 2239-2249.

(19) Groenewegen, W.; Egelhaaf, S. U.; Lapp, A.; van der Maarel, J. R. C. *Macromolecules* **2000**, *33*, 3283-3293.

(20) Meiners, J. C.; Elbs, H.; Ritzi, A.; Mlynek, J.; Krausch, G. *Journal of Applied Physics* **1996**, *80*, 2224-2227.

(21) Spatz, J. P.; Sheiko, S.; Moller, M. *Macromolecules* **1996**, *29*, 3220-3226.

(22) Price, C. Colloidal properties of block copolymers. In *Developments in Block Copolymers*; Goodman, I., Ed.; Applied Science Publishers: London, 1982; Vol. 1; pp 39-80.

(23) Tuzar, Z.; Kratochvil, P. Micelles of block and graft copolymers in solutions. In *Surface and Colloid Science*; Matijevic, E., Ed.; Plenum Press: New York, 1993; Vol. 15; pp 1-83.

(24) Mossmer, S.; Spatz, J. P.; Moller, M.; Aberle, T.; Schmidt, J.; Burchard, W. *Macromolecules* **2000**, *33*, 4791-4798, and references therein.

(25) Massey, J. A.; Winnik, M. A.; Manners, I.; Chan, V. Z. H.; Ostermann, J. M.; Enchelmaier, R.; Spatz, J. P.; Moller, M. *Journal of the American Chemical Society* **2001**, *123*, 3147-3148.

(26) Meiners, J. C.; QuintelRitzi, A.; Mlynek, J.; Elbs, H.; Krausch, G. *Macromolecules* **1997**, *30*, 4945-4951.

Appendix I

Characterization of MTD_{400}-$NORCOOH_{50}$ Statistical Copolymerization

This appendix describes our preliminary investigation of the simultaneous ROMP copolymerization of MTD and NORCOOTMS monomers. The underlying motivation for this work was to study the influence of the polymer's carboxyl (COOH) group density on the size of in-situ inorganic nanoclusters synthesized within the polymer matrices. It is commonly known that carboxyl groups of the polymer hosts associate with surfaces of inorganic nanoparticles residing in them. Such ligand interaction stabilizes the clusters against agglomeration. Previous works by the Cohen group (for example, see: Clay, R. T. Ph.D. Thesis, MIT, 1997; Kane et al. *Chemistry of Materials* **1996**, *8*, 1919) have shown that the nanoclusters synthesized within the carboxyl-containing (NORCOOH) block copolymer domains are very small - generally a few nanometers in size. As a hypothesis, such consistently small cluster size was attributed in part to the COOH capping activity.

In particular, the polymer's stabilizing capability is believed to correlate with the density of the passivating groups in the polymer matrix. Within the NORCOOH block domains, similar to a NORCOOH homopolymer, the acid group density is maximized, as the carboxyl-functionalized units are adjacent to one another in the block sequence. Thus, we anticipated that the size of the in situ nanoclusters could be enhanced by diluting the COOH group density in the polymer matrix in order to weaken the capping activity. Our initial attempt to achieve dispersion of the COOH groups in the polymer matrix was to perform copolymerization of the MTD-NORCOOTMS monomer mixture; that is, increasing spacing among the capping COOH groups in the polymer matrix by adjusting the copolymer's molecular architecture. In the absence of information on the monomers' reactivity ratios, we expected that a statistical distribution of the NORCOOTMS units within the copolymer molecules (polymerizable precursor to NORCOOH) would result from the simultaneous copolymerization of these two monomers. Our preliminary characterization of such copolymerization process is described below.

Gel Permeation Chromatography

Most of the materials (monomers and initiator) and several procedures employed for the investigation are described in Section 1.2.1. We began our investigation by polymerizing simultaneously 400 and 50 equivalent units of MTD and NORCOOTMS, respectively. This composition was chosen to enable direct comparison of the resulting copolymer with the diblock copolymer of the same monomer composition, which has been extensively used by our research group as a template for in situ nanocluster synthesis (refer to Chapter 1.) We followed the growth of the polymer chains as a function of polymerization time by performing a time-aliquot experiment and characterizing the resulting polymers with gel permeation chromatography (GPC).

Our time-aliquot experiment involved removing an aliquot from the polymerizing solution after a certain polymerization time and quenching each aliquot with a terminating agent. Specifically, we dissolved 284 mg of MTD (1.6 mmole) and 66.4 mg of NORCOOTMS (0.2 mmole) in ~7 mL of Na-dried toluene (total volume of monomer solution ~7.5 mL). The copolymerization was initiated by adding 340μL of 6.5 mg/mL solution of the Mo-based catalyst in toluene (4 μmole). Individual 0.8-mL aliquots were drawn from this polymerizing solution and quenched with degassed benzaldehyde (3 μL). Polymerization time of each aliquot is designated as the time elapsed between the addition of initiator to the monomer solution and the exposure of polymerizing aliquot to benzaldehyde (assuming instantaneous termination reaction.)

The GPC carrier solvent was THF running at a 1-mL/min flow rate (unlike the GPC experiment of Section 1.2.1 which employed toluene.) The aliquots were first dried of toluene under vacuum and redissolved in THF (at 4 mg/mL) for GPC analysis. **Figure A1 (A-D)** are examples of the GPC traces obtained from the time-aliquots. Integration of the polymer peaks yielded the polystyrene-equivalent M_n and M_w values. (GPC trace of MTD-NORCOOTMS monomer mixture displayed no signals under 31-minute elution time, indicating the absence of polymer molecules.)

The measured PS-equivalent molecular weights, shown in **Table A1**, exhibit the evident growth of the copolymer molecules over time, indicating that the polymerization proceeded successfully. The plot of **Figure A2** shows the rate of chain growth decreases drastically after ~20 minutes. A notable increase in the polydispersity index from 30 to 40 minutes is attributed to chain coupling caused by oxygen contamination. (Saunders, R. S. Ph.D. Thesis, MIT, 1992)

Transmission Electron Microscopy

Morphological investigation of the resulting copolymer was performed using transmission electron microscopy (TEM). The copolymer sample was produced by simultaneous copolymerization of 400 MTD and 50 NORCOOTMS units for 40 minutes as described above. Acidification, precipitation, and bulk film casting was performed according to procedures described in Chapter 1. Aqueous staining attempts of the resulting bulk film using $Na_2(PdCl_4)_{aq}$ resulted in no absorbed color, indicating an absence of Pd loading. Thus, staining of the COOH groups was instead achieved via gaseous $CdMe_2$. This was done by exposing microtomed sections to $CdMe_2$ vapor in a sealed chamber containing liquid $CdMe_2$ for ~3 hrs. Such staining was carried out inside a nitrogen-atmosphere drybox; it was preceded by vacuum drying to remove moisture and followed by another evacuation to remove excess $CdMe_2$.

Figure A3 shows a representative TEM image obtained from the bulk sample. $CdMe_2$ staining resulted in small (< 5nm) Cd-based nanoclusters that are distributed uniformly throughout the polymer matrix. We did not observe periodic features which are characteristic of the diblock copolymer samples of the same monomer composition that was cast in the same manner (see **Figures 1.6** and **2.1**, for example.) This observation indicates that simultaneous polymerization of the monomers does not result in a diblock copolymer. For simplicity, we will refer to this copolymer as the 'statistical' copolymer.

We also investigated thin films produced via direct casting of the statistical copolymer onto TEM grids (see Mukai, U. Sc.D. Thesis, MIT, 1994.) This was done by placing a drop of the polymer solution in THF onto a TEM grid resting on a Teflon-coated foil inside at a THF-saturated

chamber (refer to **Scheme 2.2**). For comparison, thin films of the diblock copolymer (MTD_{400}-b-$NORCOOH_{50}$) were also produced and examined along with the statistical copolymer. The $CdMe_2$-stained diblock thin films (**Figure A4**) exhibit a morphology comprising worm-like block domains, which occurred due to the fast solvent evaporation rate (see discussion of **Figure 2.13** in Section 2.5.)

The thin films of the statistical copolymer (**Figure A5**) once again exhibit primarily uniform distribution of small nanoclusters, without the worm-like domains characteristic to the diblock counterpart. However, we noticed that these samples also contain larger features of size 10-30nm that are randomly distributed throughout the matrices. It is not obvious what these larger features represent. A possibility is that they were formed via agglomeration of several small Cd-based clusters. Assuming such a scenario, one may further speculate that these larger clusters occurred as a result of the relatively low density of COOH groups present in the statistical copolymer matrix, which led to the reduced passivating strength.

However, these features could also represent Cd-stained carboxyl-rich polymer domains. In the extreme case, they could be domains of NORCOOH homopolymer molecules undergoing phase separation. In another possible scenario, these domains may represent segregated domains of NORCOOH block sequences present in the statistical copolymer chains. (A problem with this scenario is the dimensions of the copolymer molecules do not account for the relatively large size and spacing of these hypothetical domains.) The fact that such domains were not observed in the bulk-cast statistical copolymer renders such (segregated domain) interpretation unlikely.

In short, the predominantly uniform Cd-staining observed via TEM supports our hypothesis for a statistical distribution of the NORCOOH monomer units within the MTD-NORCOOH copolymer molecules. However, the larger stained features that potentially represent segregated NORCOOH domains implies that the possibility of forming block-like copolymers or homopolymers upon the simultaneous copolymerization of MTD and NORCOOTMS cannot be eliminated. TEM

visualization of the copolymer morphology using alternative staining agents/methods may be employed to verify the above observations.

Nuclear Magnetic Resonance Spectroscopy

To gain insight into the distribution of the monomers within the copolymer molecules, we also studied the conversion of each monomer as a function of polymerization time via the use of nuclear magnetic resonance spectroscopy (NMR, performed with a Bruker Avance DPX-400 spectrometer.) **Figure A6** shows the NMR spectra of the monomers in deuterated (d_8) toluene. The olefin ^1H peaks of the monomers, located between 5.9 – 6.2pmm, are mostly resolved, except for a minor MTD peak near 6.2 ppm that partially overlaps the NORCOOTMS peak. These olefin ^1H signals are employed to quantify the monomers at different polymerization times.

Time-aliquots are once again used for our NMR study of the polymerization process. However, instead of 400MTD-50NORCOOTMS composition, we polymerized 200 equivalent units of each monomer for the NMR experiment. This one-to-one starting ratio was employed in order to simplify the subsequent interpretation of the relative conversion rates of the two monomers.

The copolymerization for NMR analysis was performed in d_8-toluene rather than protonated toluene to avoid the need for subsequent solvent evaporation (prior to redissolving the aliquot content into another NMR solvent.) This was due to the fact that the MTD monomers would be removed from the aliquots upon application of vacuum during the drying step. Degassing of d_8-toluene was achieved via the 'freeze-pump-thaw' cycles. This involved freezing the solvent using liquid nitrogen; once solidified, the solvent was subjected to a vacuum treatment to remove oxygen. Following evacuation, the solvent was allowed to melt upon warming to room temperature. This cycle was repeated 3 times before the resulting deoxygenated d_8-toluene was transferred into the drybox. Then, similar to other solvents used for ROMP syntheses in this work, additional drying of the degassed d_8-toluene was done before use by storing over Na pellets, followed by filtering through 0.5-μm syringe filters.

The starting monomer mixture contained 97.4mg MTD and 182.6mg NORCOOTMS in ~8mL of d_8-toluene. Chlorobenzene (22mg, anhydrous) was also added to the starting monomer solution the as internal reference for the aliquots. The relevant chlorobenzene ^{1}H NMR signal is located at ~6.9ppm. This chlorobenzene peak was employed for normalization of the integrated monomer signals, thus enabling direct quantitative comparison of monomer conversion among the different time-aliquots. Aliquot 1 (zero-time, starting monomers mixture) was drawn from the mixture prior to addition of the initiator. Each subsequent aliquot (1 mL) was drawn at increasing times and terminated with benzaldehyde (6 μL).

Figure A7 (A-H) are the NMR spectra obtained from the 8 aliquots. With increasing polymerization time, the polymer's olefin ^{1}H signals (5.3-5.9 ppm) grow at the expense of the monomer signals. The integrated monomer peak areas (normalized against chlorobenzene internal standard) for the time-aliquots are summarized in **Table A2**. The integrated peak values of the zero-time aliquot (unreacted monomers) were normalized to 200 by factors of 64.47 and 26.49 for MTD and NORCOOTMS, respectively. These factors were then used to normalize all the other aliquots. The resulting values thus represent the equivalent amounts of unreacted monomers per an initiator molecule.

The conversion of monomers as a function of polymerization time is plotted in **Figure A8**. Similar to the trend observed via GPC, the rate of monomer conversion decreased over time, and over 97% of the monomers were consumed within 30 minutes. The key information in this plot is the fact that the conversion rates of the two monomers are comparable, evident from the sustained near-one-to-one molar ratio throughout the polymerization process.

Addition copolymerization processes are generally characterized by the monomer reactivity ratios according to the Mayo-Lewis model. (Rempp, P.; Merrill, E. W. *Polymer Synthesis*, 2 ed.; Hüthig & Wepf: New York, 1991.) A monomer reactivity ratio is defined as the ratio of the rate constants for addition of one monomer type (M) to a propagating end terminated by an M unit, to that for the addition of the other monomer type (N) to the same of active center. That is:

$$\sim\sim\sim M^* + M \xrightarrow{k_{mm}} \sim\sim\sim MM^* \quad \textit{and} \quad \sim\sim\sim M^* + N \xrightarrow{k_{mn}} \sim\sim\sim MN^*$$

Thus, the reactivity ratio for monomer M is: $r_m = (k_{mm} / k_{mn})$; similarly, $r_n = (k_{nn} / k_{nm})$. While our existing NMR data is not adequate for the calculation of the MTD-NORCOOTMS reactivity ratios, the absence of a systematic drift in the monomer feed composition from the one-to-one starting ratio indicates that the two reactivity ratio values are essentially equal. That is, $r_m \approx r_n$, where r_m and r_n represent the reactivity ratios of MTD and NORCOOTMS active centers, respectively.

Several scenarios exist regarding the distribution of monomers within the resulting copolymer molecules, depending on reactivity ratios' numerical values. For $r_m = r_n \sim 1$, both types of active centers exhibit no preference towards either monomer type, resulting in a random distribution of monomer units in the polymer chains. This scenario leads to a copolymer of the same composition as the monomer mixture, regardless of the initial feed composition. The formation of alternating copolymers of MTD and NORCOOTMS ($r_m = r_n = 0$) can be discarded as a possibility since both monomers have been shown to homopolymerize successfully. A more plausible scenario would be for $0 < r_m = r_n < 1$, which is intermediate between the alternating and the random copolymers (favoring cross-propagation). It would also imply an existence of an azeotrope at the 1:1 monomer-feed ratio.

As mentioned earlier, TEM results exhibit primarily random distribution of COOH groups in the polymer samples, supporting the case for a copolymer where the COOH groups are statistically distributed ($0 < r_m = r_n \leq 1$) within the polymer molecules. Statistical copolymers are also the most commonly observed products in copolymerization processes. Whether the MTD-NORCOOTMS copolymer system (in toluene) is ideal ($r = 1$) or azeotropic ($r < 1$) may be determined via polymerization experiments at monomer feed compositions above or below the one-to-one molar ratio (the azeotrope for the potential $r < 1$ case). In the ideal case, the starting feed ratio would be sustained, while in the azeotropic case the composition would drift further

from the azeotropic composition during polymerization, leading to compositional heterogeneity in the copolymer molecules.

Additional scenarios include the formation of block-like copolymers and homopolymers. The tendency to form long sequences (block) of the same repeat units arises when $r_m = r_n > 1$. For the extreme case of $r_m = r_n >> 1$, homopolymers are produced. Though rarely observed, our TEM observation indicates that these possibilities should also be considered. According to the Mayo-Lewis method, determination of the reactivity ratios of a monomer pair requires acquisition of the 'instantaneous' (i.e., at low conversion) polymer compositions for a series of starting monomer-feed compositions. Such quantitative measurements for the MTD-NORCOOTMS system should be possible via the NMR (e.g., ^{1}H and ^{13}C).

With the knowledge of the MTD-NORCOOTMS reactivity ratios, the distribution of the monomer units within the copolymer molecules could be controlled. Morphological observation (e.g., via TEM) would provide supporting information on the molecular architecture as the distribution of monomer units (the COOH groups) in the copolymer influences its microstructure. In addition to NMR and TEM, the copolymer molecular architecture may also be probed via other experimental approaches such as determination of the glass transition temperature. (Our attempt to determine the glass transition of using the DSC failed partly due to the high T_g's exhibited by the polymer species.)

Finally, the ability to control the distribution of the NORCOOH monomer units within the MTD-NORCOOH copolymer system would enable the investigation of the effects of COOH group density on the size of in situ nanocluster, and may also be useful towards studying other cluster synthesis parameters. For example, construction of block copolymer domains with diffuse (i.e., 'blurred up') block interfaces may be possible via the synthesis of 'tapered' MTD-NORCOOH block copolymers. Such structure would enable the inquiry into the role of domain interfaces on the nucleation and confinement of in situ nanoclusters within the segregated block domains, in comparison with the sharp interfaces of the conventional discrete block version.

Figure A1: GPC traces from copolymerization of 400 MTD & 50 NORCOOTMS monomer units

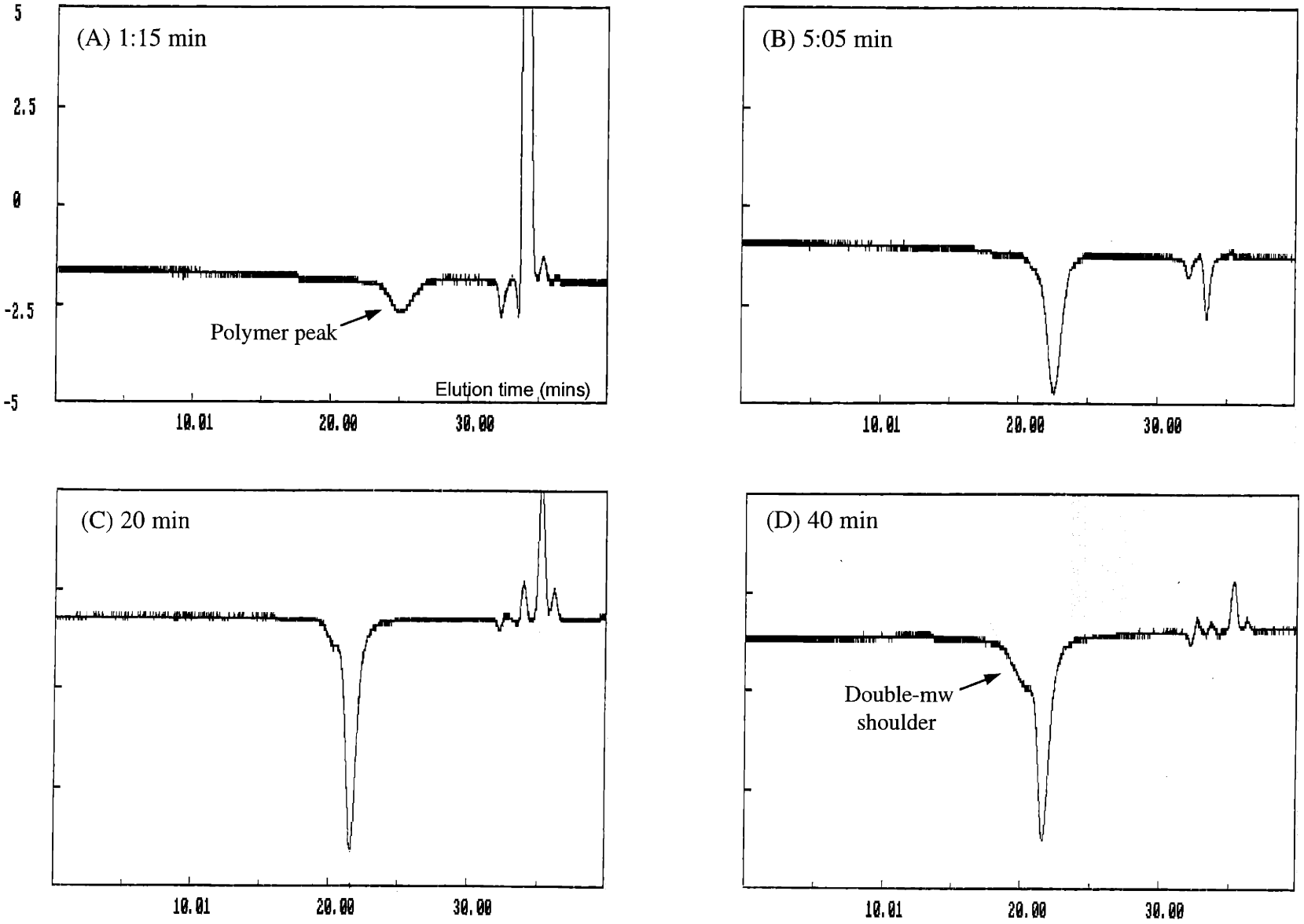

Table A1: Statistical copolymerization of 400 MTD-50 NORCOOTMS: time-aliquot molecular weights obtained via GPC

Rxn time (min:sec)	Mn (PS-equivalent)	Mw	PDI
1:15	19,188	22,006	1.153
2:45	37,769	40,336	1.068
5:05	65,069	72,112	1.108
10:10	93,153	100,247	1.076
20:00	102,399	112,963	1.103
30:00	107,127	116,271	1.085
40:00	107,573	137,791	1.281

Figure A2: Plot of the copolymer's molecular weight as a function of polymerization time (data from **Table A1**)

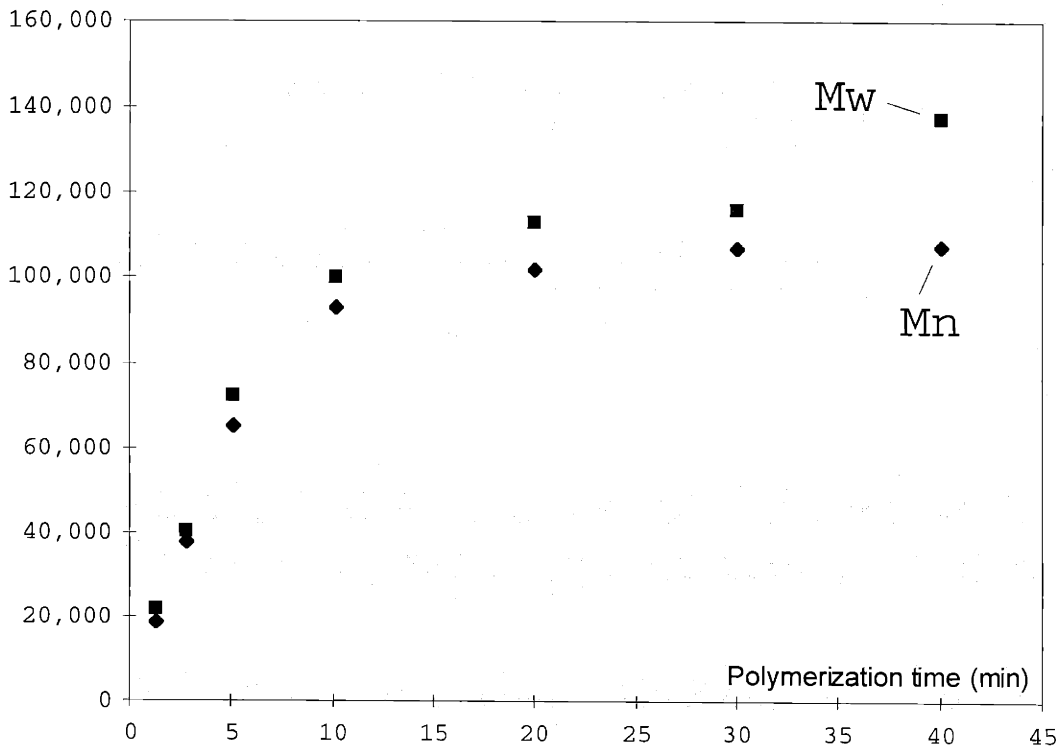

Figure A3: Bulk-cast MTD_{400}-$NORCOOH_{50}$ statistical copolymer stained with $CdMe_{2(g)}$

Figure A4: Diblock copolymer thin film cast onto TEM grid; stained with $CdMe_{2(g)}$

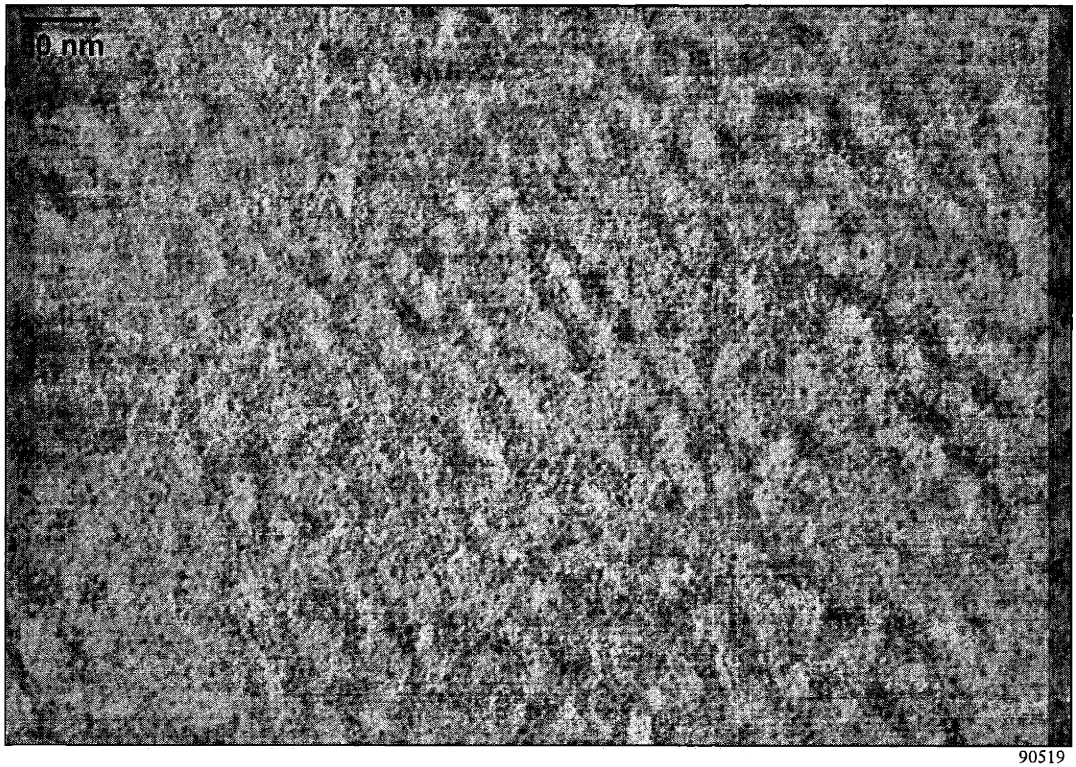

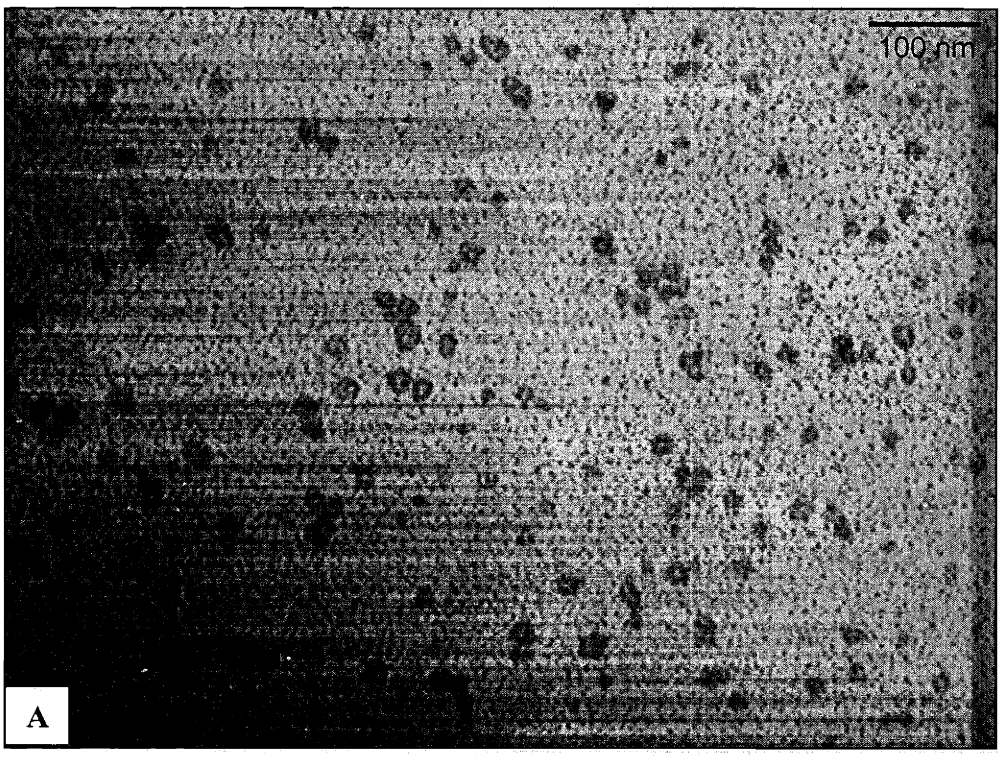

90103

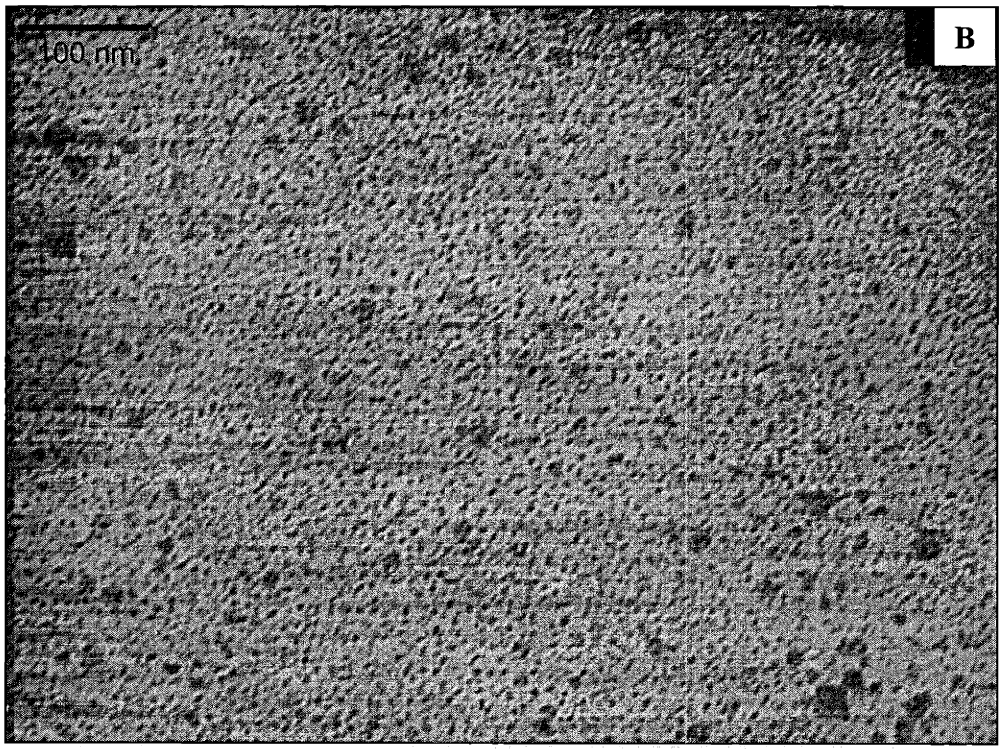

90019

Figure A5 (A,B): Statistical copolymer thin films cast onto TEM grids; stained with $CdMe_{2(g)}$

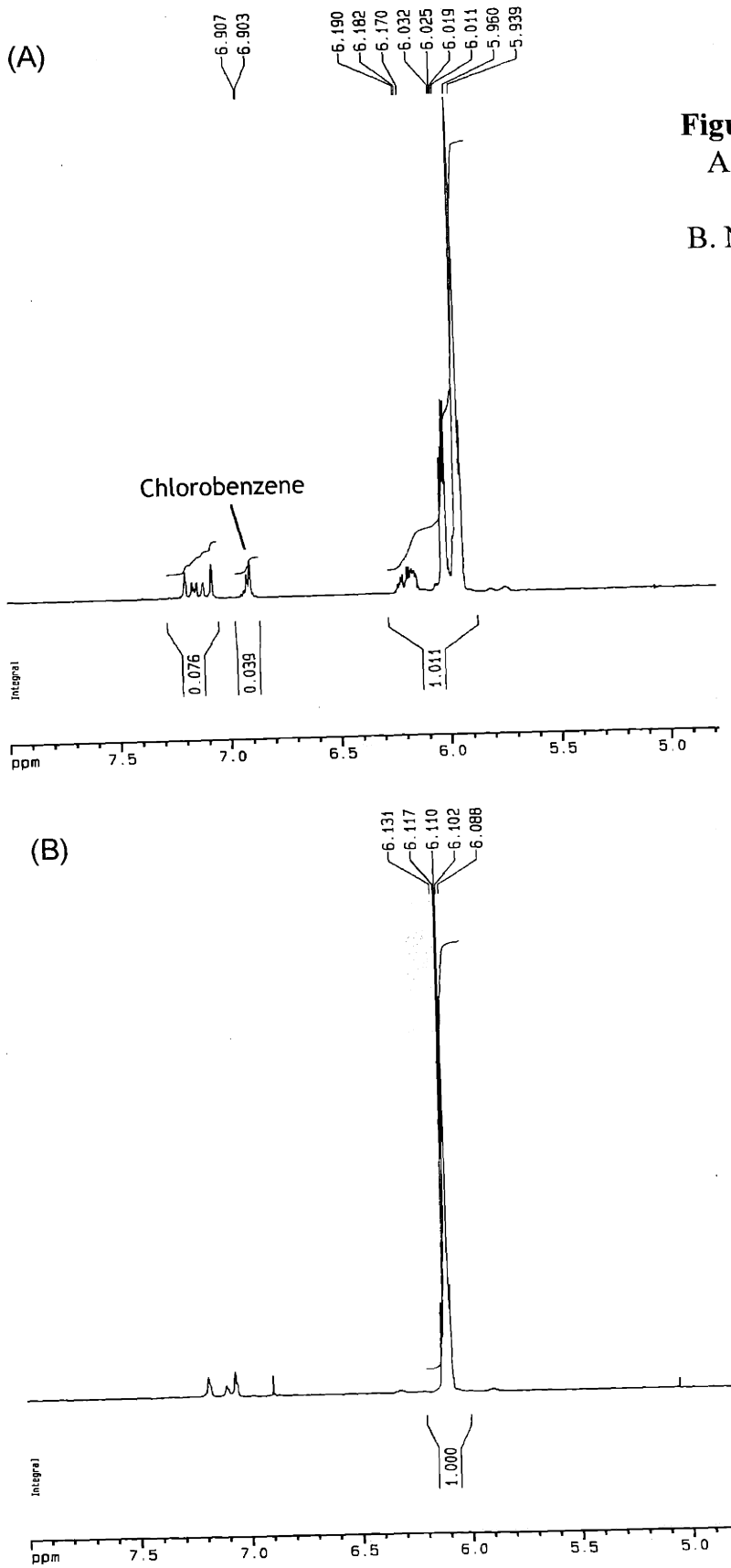

Figure A6: NMR spectra of:
A. MTD monomer (with chlorobenzene)
B. NORCOOTMS monomer

Current Data Parameters	
NAME	ROMP-kntcl
EXPNO	1
PROCNO	1
F2 - Acquisition Parameters	
Date_	990812
Time	15.45
INSTRUM	spect
PROBHD	5 mm QNP (13
PULPROG	zg
TD	32768
SOLVENT	Tol
NS	16
DS	1
SWH	4006.410 Hz
FIDRES	0.122266 Hz
AQ	4.0894966 sec
RG	64
DW	124.800 usec
DE	6.00 usec
TE	300.0 K
D1	1.00000000 sec
P1	7.20 usec
DE	6.00 usec
SFO1	400.1320007 MHz
NUC1	1H
PL1	-3.00 dB
F2 - Processing parameters	
SI	16384
SF	400.1299741 MHz
WDW	EM
SSB	0
LB	0.30 Hz
GB	0
PC	1.00
1D NMR plot parameters	
CX	20.00 cm
F1P	8.000 ppm
F1	3201.04 Hz
F2P	3.000 ppm
F2	1200.39 Hz
PPMCM	0.25000 ppm/cm
HZCM	100.03249 Hz/cm

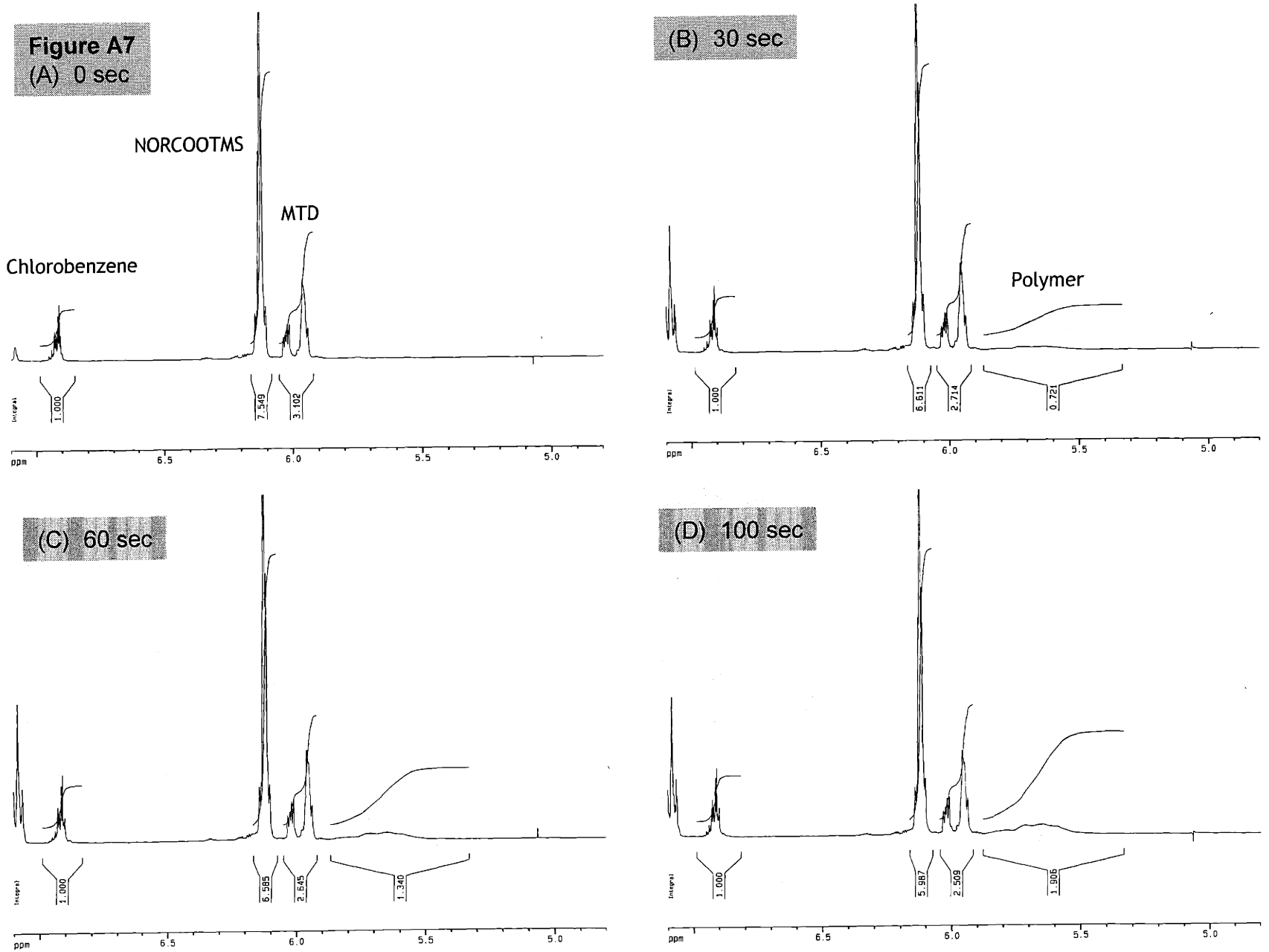
Figure A7
(A) 0 sec
NORCOOTMS
MTD
Chlorobenzene
1.000
7.549
3.102
ppm
6.5
6.0
5.5
5.0
(B) 30 sec
Polymer
1.000
6.611
2.714
0.721
(C) 60 sec
1.000
6.585
2.645
1.340
(D) 100 sec
1.000
5.987
2.509
1.906

Figure A7

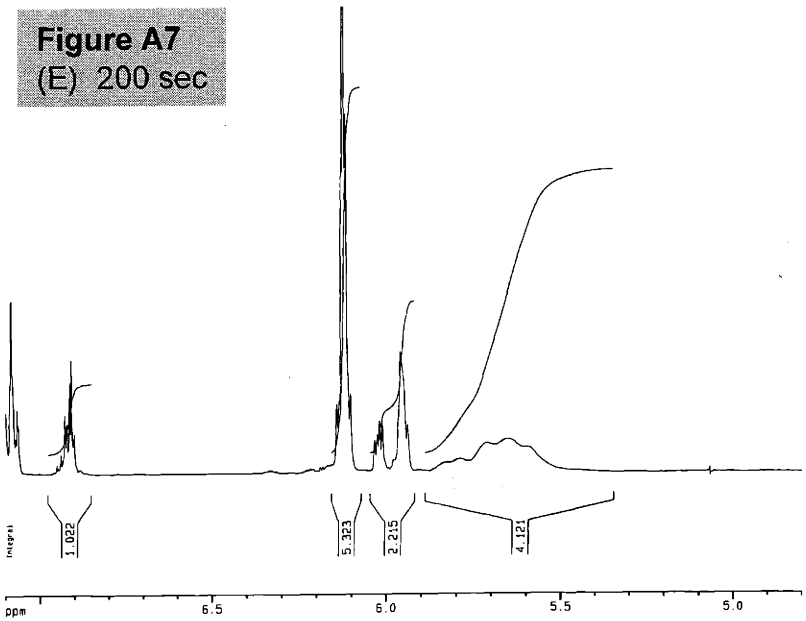
(E) 200 sec
Integral
1.022
5.323
2.215
4.121
ppm
6.5
6.0
5.5
5.0

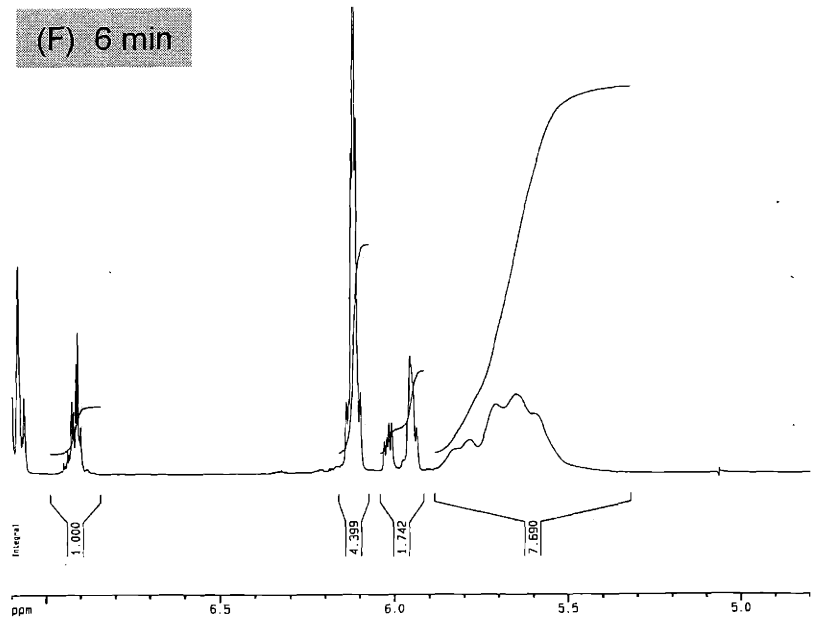
(F) 6 min
Integral
1.000
4.399
1.742
7.690
ppm
6.5
6.0
5.5
5.0

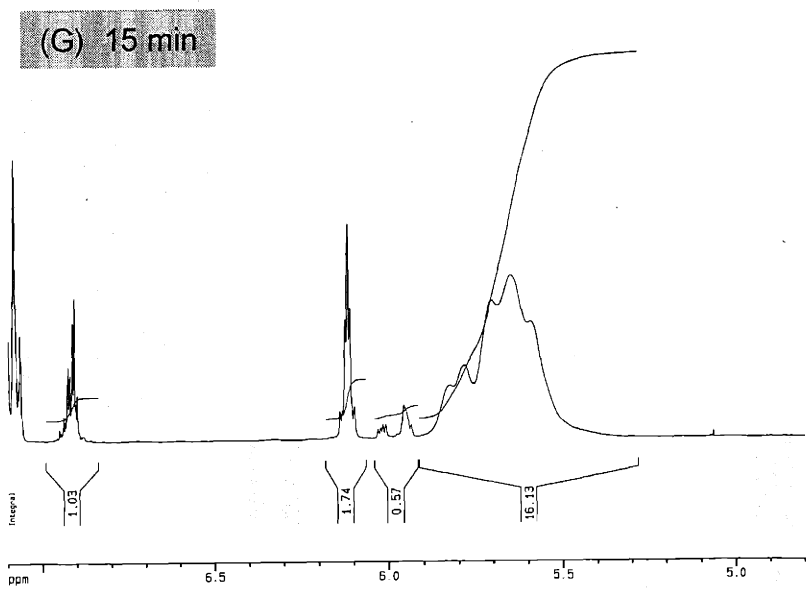
(G) 15 min
Integral
1.03
1.74
0.57
16.13
ppm
6.5
6.0
5.5
5.0

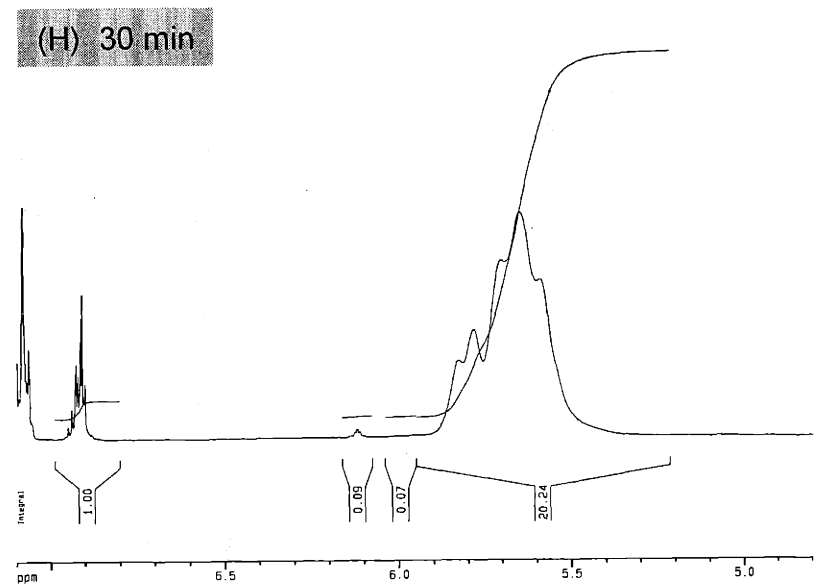
(H) 30 min
Integral
1.00
0.09
0.07
20.24
ppm
6.5
6.0
5.5
5.0

Table A2: Conversion of MTD and NORCOOTMS monomers upon copolymerzation (data obtained via NMR)

Rxn time (sec)	MTD (signals normalized against chlorobenzene internal ref.)	NORCOOTMS	MTD (normalized to 200 units at zero Rxn time)	NORCOOTMS
0	3.102	7.549	200.0	200.0
30	2.714	6.611	175.0	175.1
60	2.645	6.585	170.5	174.5
100	2.509	5.987	161.8	158.6
200	2.167	5.208	139.7	138.0
360	1.742	4.399	112.3	116.5
900	0.553	1.689	35.7	44.7
1800	0.070	0.090	4.5	2.4

Figure A8: Plot of monomer conversion as a function of polymerization time (data from **Table A2**)

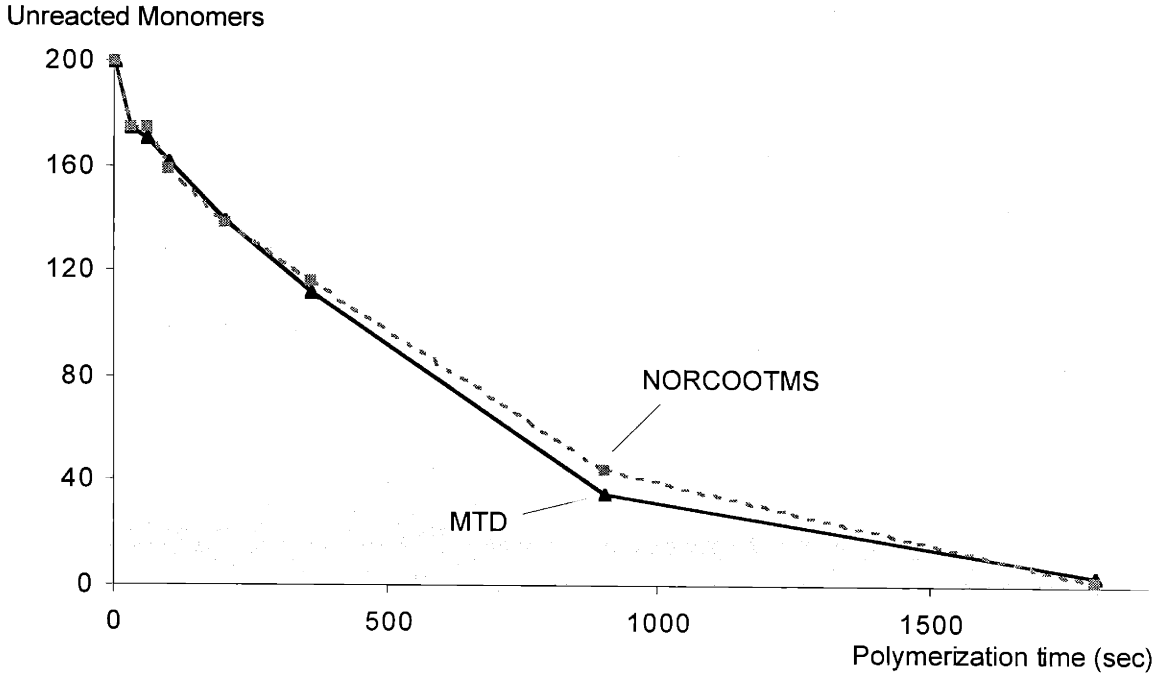

Appendix II

Balsara-Cohen Collaboration

This appendix illustrates a set of transmission electron micrographs which was acquired as a contribution to work done in collaboration with Professor Nitash Balsara, U. of California, Berkeley. The TEM observation served to verify the morphology of a partially ordered, symmetric styrene-isoprene diblock copolymer sample (molecular weight 12 kg/mole) which is the subject of the study. A manuscript of this work, titled "Analysis of Grain Structure in Partially Ordered Block Copolymers by Depolarized Light Scattering and Transmission Electron Microscopy" was submitted to *Macromolecules* in May 2001. (Authors include M.Y. Chang, W.G. Kim, B.A. Garetz, M.C. Newstein, N.P. Balsara, L. Yang, S.P. Gido, R.E. Cohen, Y. Boontongkong, and A. Bellare.)

Sample preparation for our TEM investigation included a 21-hr exposure of the bulk sample to OsO_4 vapor to crosslink the sample's outer skin in preparation for the subsequent embedding in epoxy. Following epoxy embedding, the sample was microtomed and stained to obtain TEM contrast. Sample exposure to either of two selected staining agents was done by placing microtomed sections in the saturated vapor phase of a sealed chamber containing an aqueous solution of the staining agent. Exposure to RuO_4, which selectively stains polystyrene domains, was performed for 30 minutes. Exposure to OsO_4, which selectively stains polyisoprene domains, was carried out for 6 hrs. **Figures A9 – A11** and **Figures A12 – A14** are TEM images of samples stained with Ru and Os, respectively. (TEM images were obtained using a Jeol 200CX microscope operating at 200kV.) These images illustrate that the diblock copolymer sample

comprises 2 distinct morphologies: the periodic lamellar structure observed in the Ru-stained sections, and the worm-like structure observed in Os-stained sections.

TEM investigation performed by Balsara et al. (via OsO_4 staining, shown in manuscript) produced morphologies that are consistent with ours; the difference being that both morphologies were seen as neighboring regions within the same Os-stained microtomed sections. The paper refers to regions containing the periodic striped lamellae as the ordered regions (grains), while those comprising the worm-like ('dimples') structure are referred to as disordered regions. Balsara's quantitative analysis of TEM images yielded a 13-nm value for both the period of the ordered lamellae and the length scale of the concentration fluctuations displayed by the disordered structure. The following submitted abstract summarizes the main findings outlined in the manuscript:

"The grain structure in lamellar block copolymer samples undergoing a disorder-to-order transition was studied by a combination of depolarized light scattering (DPLS) and transmission electron microscopy (TEM). The four-fold symmetry of the DPLS profiles indicated the presence of anisotropic grains. An algorithm for analyzing the TEM micrographs of samples partially filled with anisotropic, ordered grains was developed. The volume fractions of sample occupied by ordered grains determined from light scattering and electron microscopy are in reasonable agreement. Both methods indicate that, on average, the characteristic length of the grains in the direction perpendicular to the lamellar planes was a factor of two larger than that in the plane of the lamellae. However, the absolute magnitudes of grain sizes determined by light scattering are a factor of four larger than those determined by microscopy."

Figures A9 - A11: Poly(styrene-block-isoprene) sample stained with RuO_4

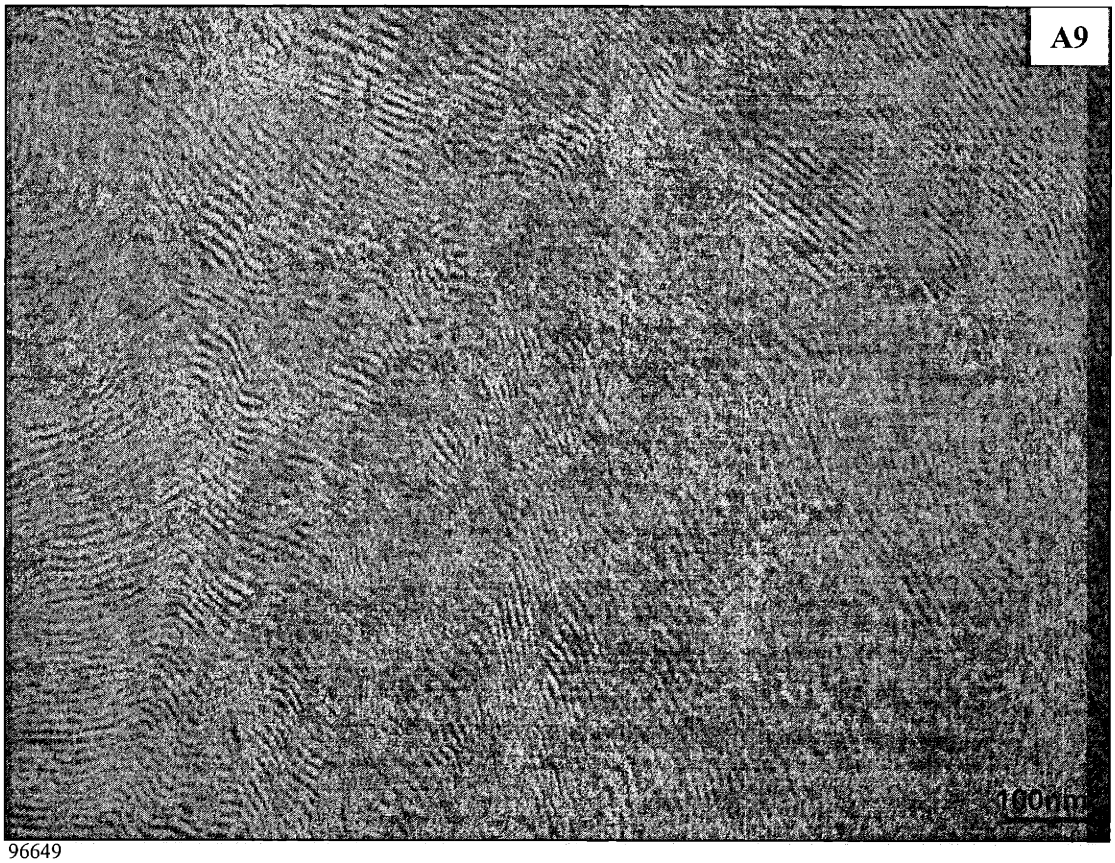

96649

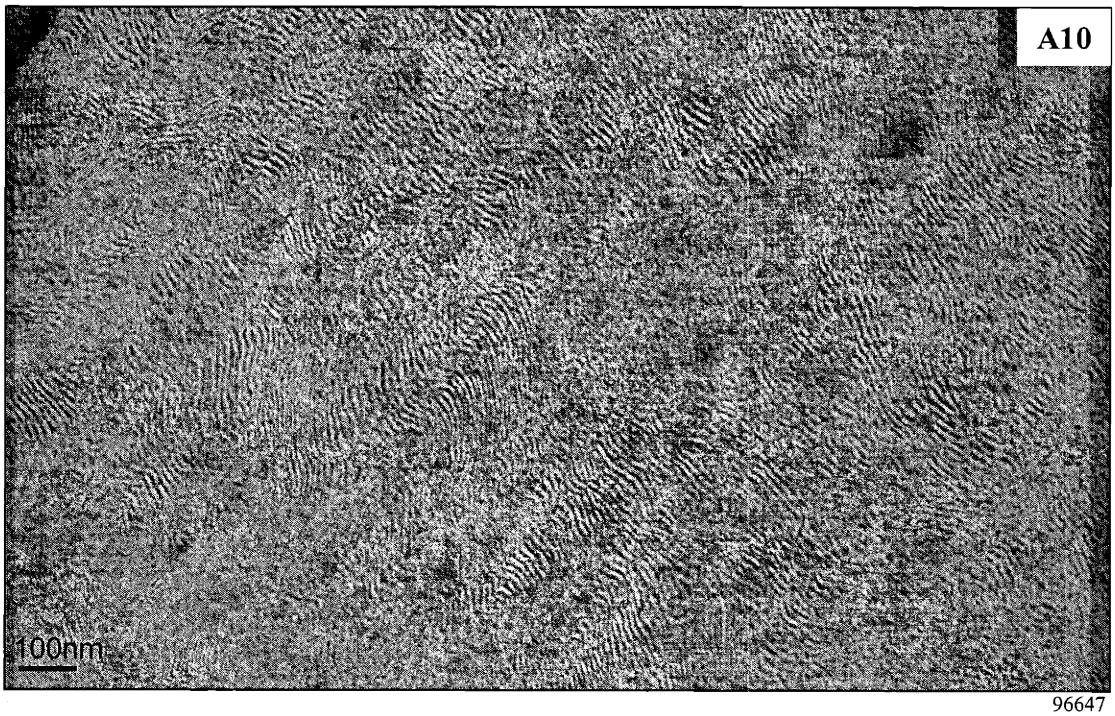

96647

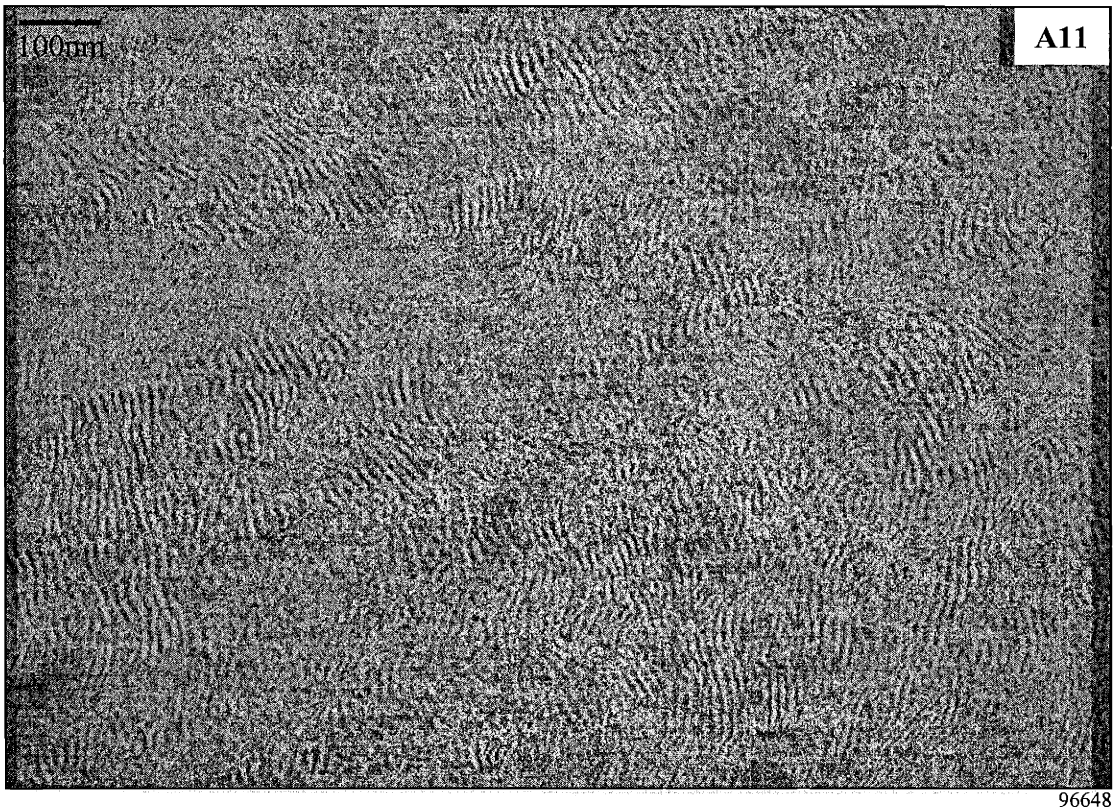

Figures A12 - A14: Poly(styrene-block-isoprene) sample stained with OsO_4

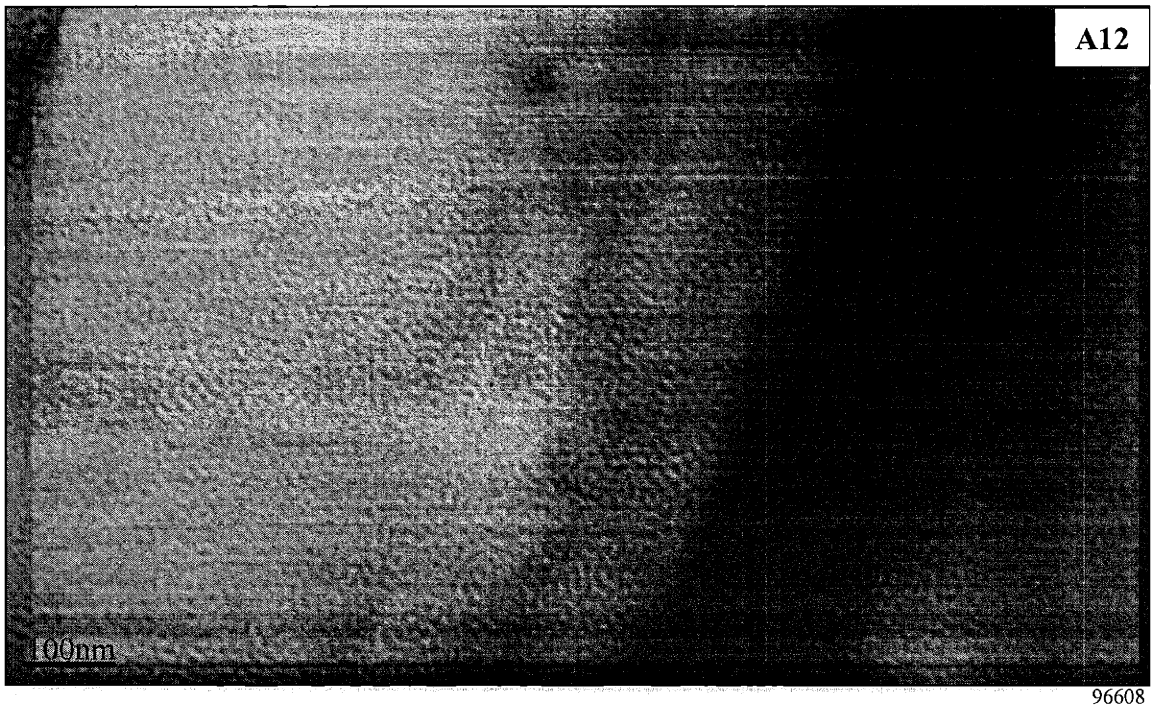

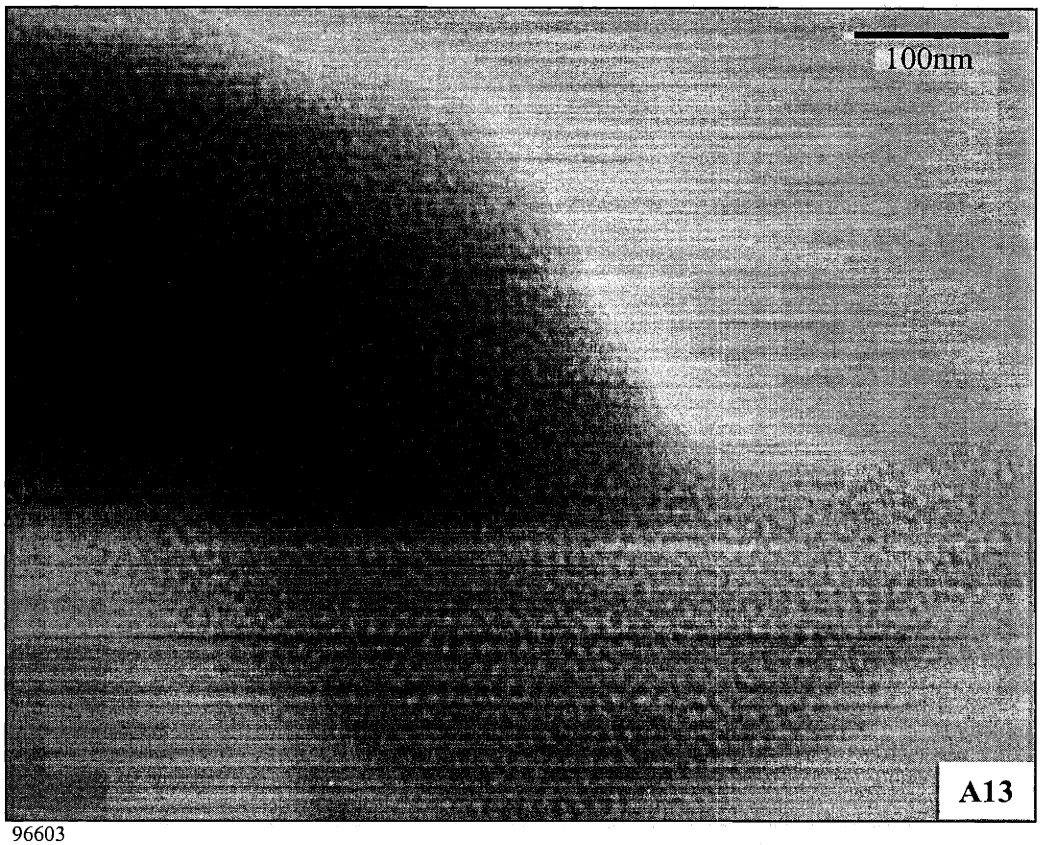

96603

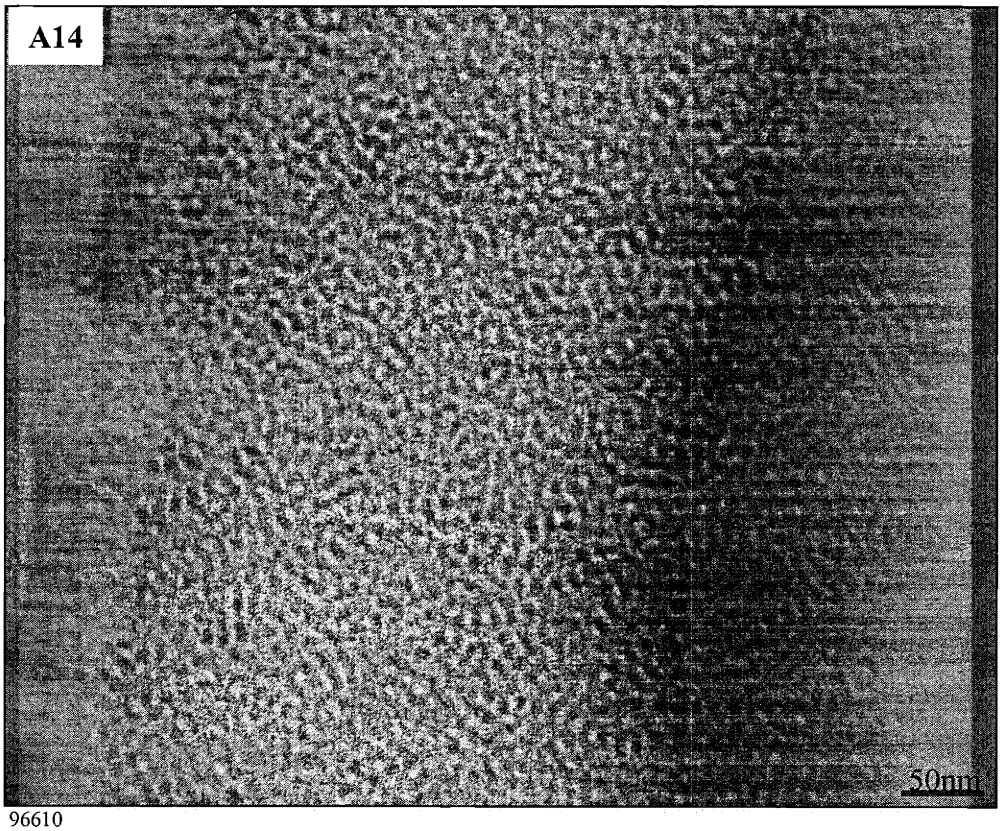

96610

Appendix III

Additional Micrographs

This Appendix illustrates microscopic images obtained during the course of this thesis project. They are presented here as supplement to the preceding chapters, or as stand-alone images for their aesthetic impression on the author (who hopes that the readers will agree!)

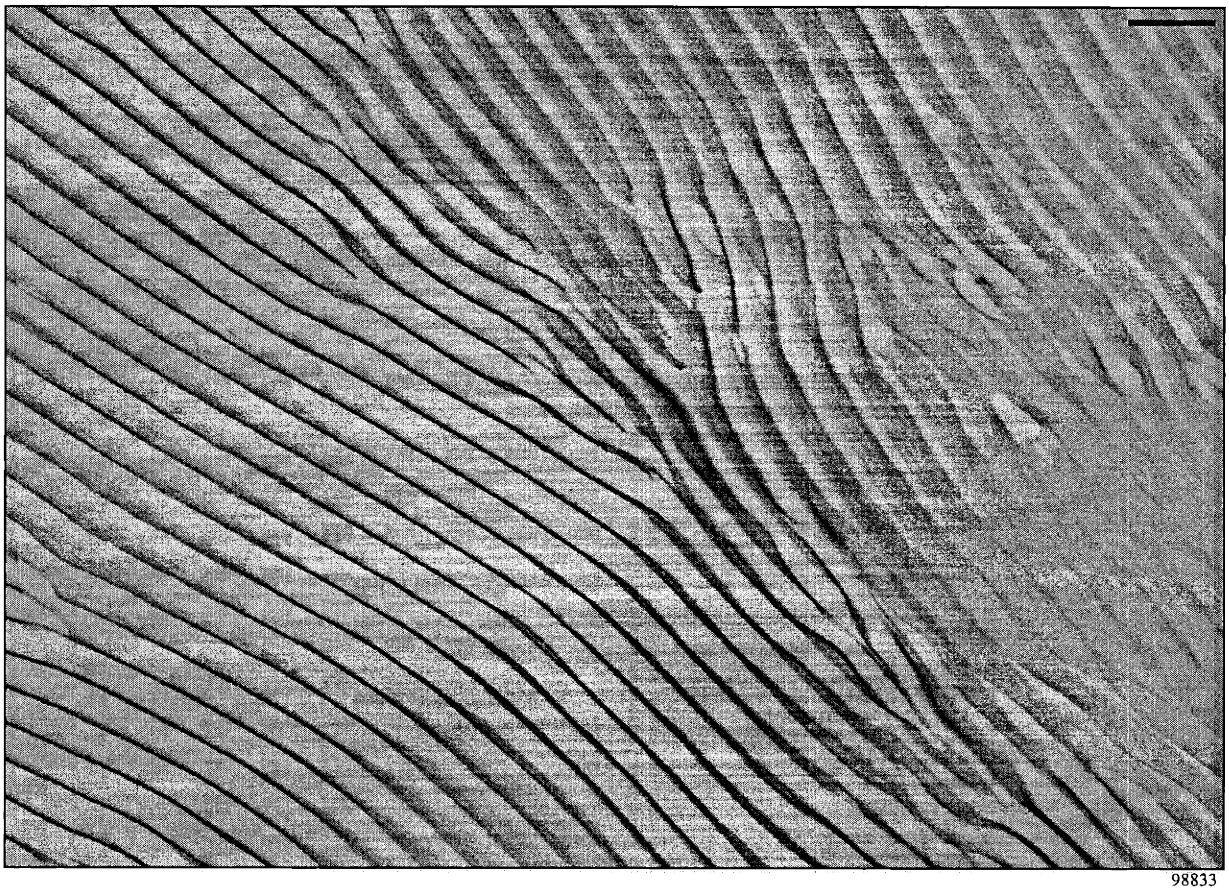

Figure A15: 'Streams'

The ordered morphology of poly(MTD_{400}-block-$NORCOOH_{50}$) bulk film (cast from THF - Chapter 1) is, to me, quite fascinating. The self-assembled structures displayed by its lamellar block domains are often rather artistic. The NORCOOH domains in this TEM image are stained with $PbAc_{2(aq)}$. My initial impression of this image was of flowing water. The smooth, liquid appearance of these lamellae seems to portray two slow-flowing streams meeting each other. (bar = 100nm)

Figure A16: 'Petals'

In this TEM image, the NORCOOH domains of an MTD_{400}-block-$NORCOOH_{50}$ bulk sample are decorated with PbS nanoclusters following loading the polymer sample with $PbAc_2$ and exposing it to H_2S (ref 29, Chapter 3). The 'swirling' domains located in the lower-right quarter of the image reminded me of flower petals. (bar = 100nm)

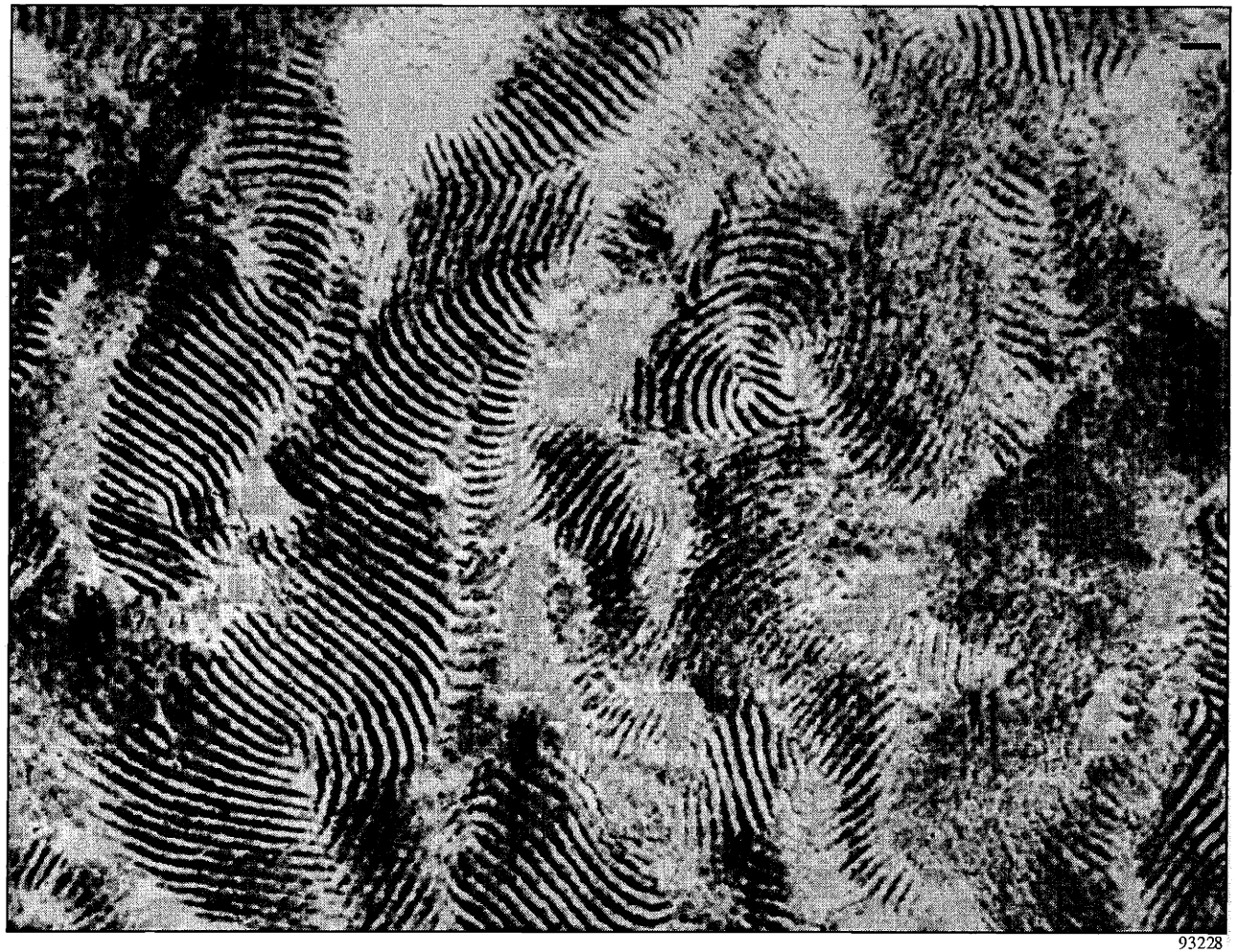

Figure A17: 'Zebra'

This TEM image shows the lamellar grains of the MTD_{400}-block-$NORCOOH_{50}$ bulk film decorated with electroless copper ('slow-plating' Formula II copper plating bath - section 2.3.2). (bar = 150nm) See a zebra? Do her stripes appear dizzying - the same optical trick that makes it hard to single out individual zebras from their herd, increasing their odds against natural predators?

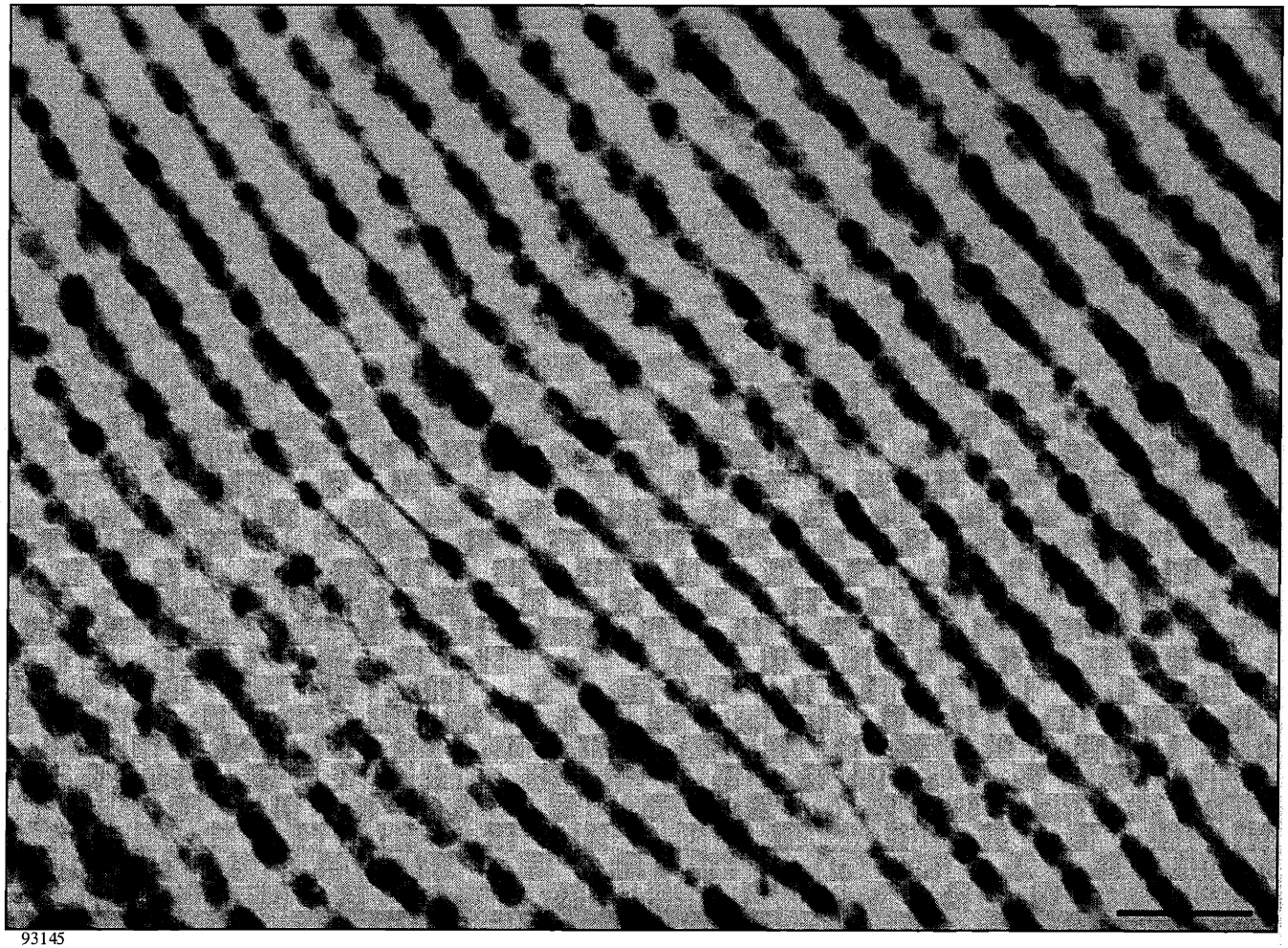

Figure A18: 'String Beans'

Bulk film poly(MTD_{400}-b-$NORCOOH_{50}$) treated in Formula II 'slow-plating' electroless copper bath for 16 hrs (same sample as **Figure 2.4** and **2.7**). This TEM image was taken at a region ~1.5 μm away from film's free surface. The lamellae's edge-on view depicts the growth of copper structures along the originally thin (~4nm) NORCOOH domains. (bar = 100nm)

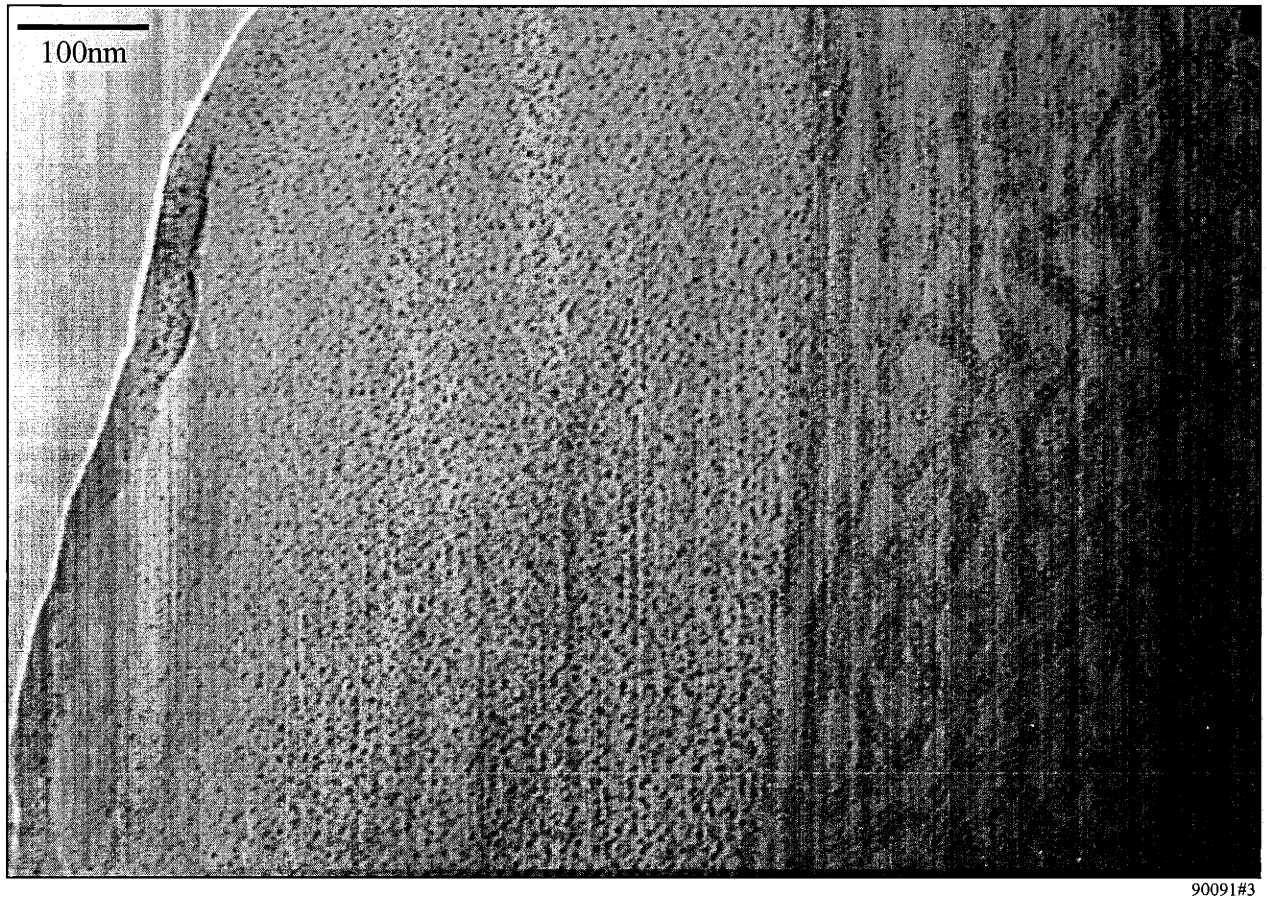

Figure A19: Undecided

TEM image of an MTD_{400}-b-$NORCOOH_{50}$ thin film sample cast directly onto a TEM grid and stained with $CdMe_{2(g)}$. Interestingly, on the left-hand side the sample displays a morphology similar to that of the statistical copolymer (see Appendix I). With increasing film thickness towards the right, the sample assumes a segregated-domain morphology typical of a block copolymer..

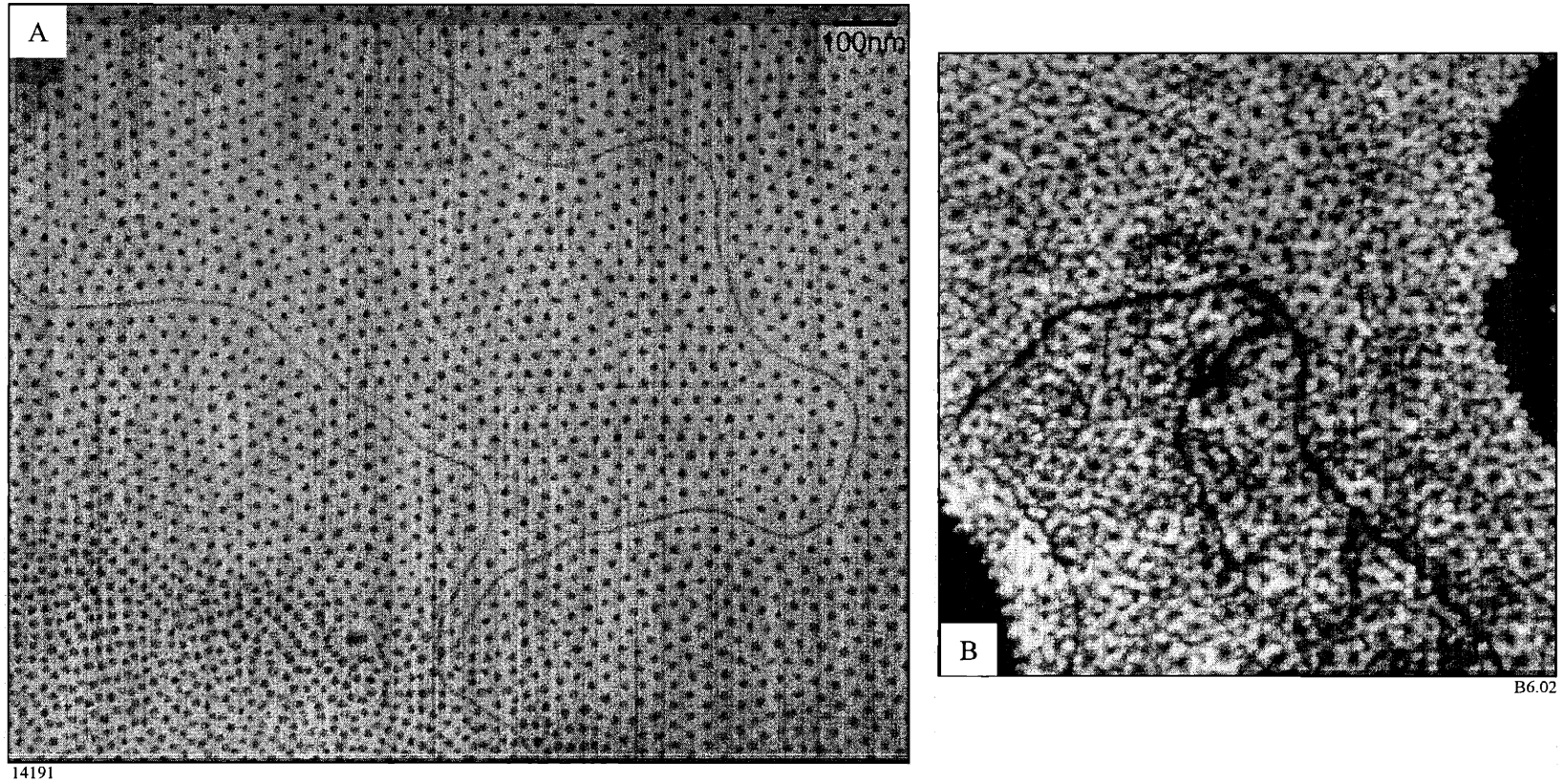

Figure A20: 'Monster'

These micrographs illustrates rare looks at cylindrical micelles in some of the PS-b-PAA micellar thin films (most of the cylindrical micelles have been transformed into spherical ones upon heating the casting solution - see Chapter 3.) TEM image (A) of an uncavitated sample ($PbAc_2$-loaded, bypassing NaOH, and exposed to H_2S) shows in-plane cylindrical micelles surrounded by spherical micelles. Notice the double-layered spherical micelles (bottom-left), and the absence of ring-like structure associated with cavitation in the TEM image. AFM height image of an NaOH-treated film (B) shows that cylindrical micelles also cavitated via alkali swelling. It gave Libby Shaw of CMSE an impression of a deep-sea creature with long tentacles: a minimonster, perhaps?!

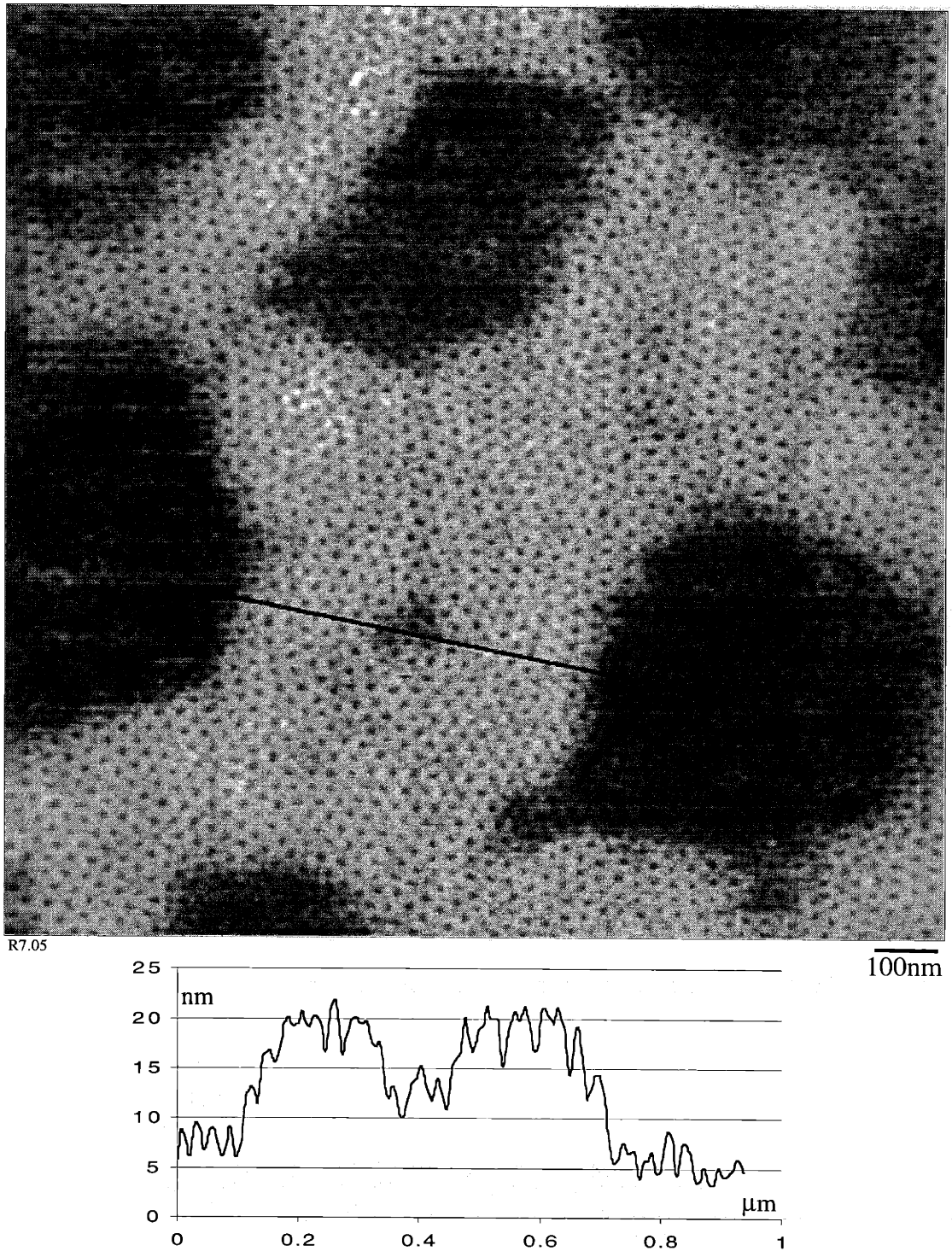

Figure A21: 'Plateaus'

AFM height image of a cavitated PS-b-PAA micellar thin film treated in $NaOH_{aq}$ and $CuAc_{2(aq)}$. The height modulation of ~14nm in the associated 2D profile indicates stacking of deposited micelle layers. The top layer of the stacked region (likely double-layered) is cavitated. The observation of **Figure 3.17** suggests that the bottom micelle layer is not open to film's surface.

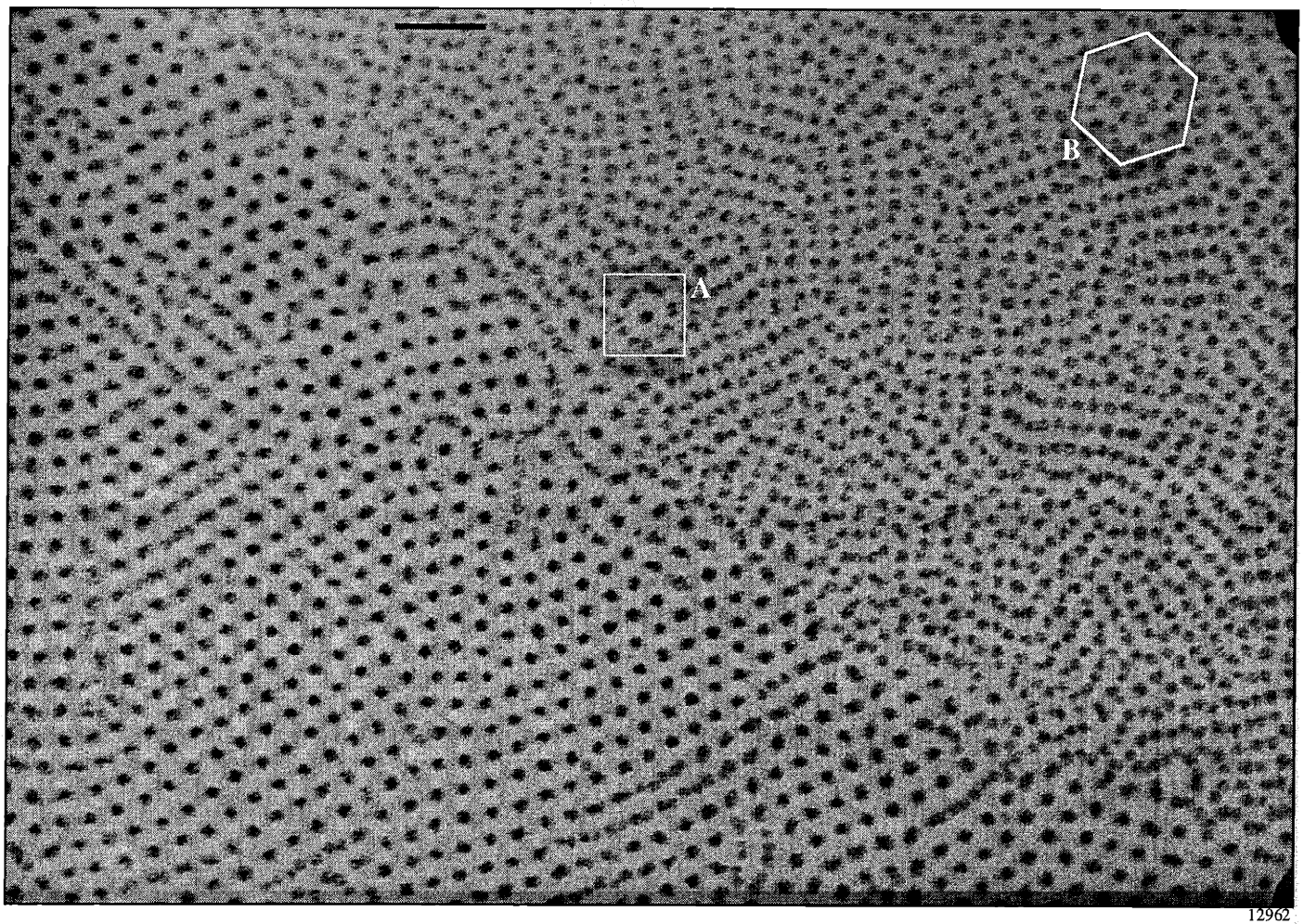

Figure A22: Stacked Hexagonal Bilayer

TEM image of a PS-b-PAA micellar thin film loaded with PbAc2(aq) (NaOH-bypassed), showing micelle bilayer. In the lower-left half, the micelles layers are stacked mostly in register (directly over each other). The out-of-register stacking in the upper-right part of reveals interesting Moiré patterns. (See Mansky et al., *J. Mater. Sci.* **1995**, 30, 1987, and ref 6 of Chapter 3.) Box A outlines a 12-membered ring (pure rotation from in-register); box B an inverse-contrast pattern (pure translation). (bar = 100nm)